

Time Correlated γ -ray Spectroscopy and High-Spin Structure of the Odd-Odd Nucleus ^{210}Fr

by

Vincent Margerin



A thesis submitted for the degree of Master of Philosophy
of the Australian National University

December, 2012



“Le savant n’étudie pas la nature parce que cela est utile ; il l’étudie parce qu’il y prend plaisir et il y prend plaisir parce qu’elle est belle. Si la nature n’était pas belle, elle ne vaudrait pas la peine d’être connue, la vie ne vaudrait pas la peine d’être vécue. Je ne parle pas ici, bien entendu, de cette beauté qui frappe les sens, de la beauté des qualités et des apparences ; non que j’en fasse fi, loin de là, mais elle n’a rien à faire avec la science ; je veux parler de cette beauté plus intime qui vient de l’ordre harmonieux des parties, et qu’une intelligence pure peut saisir.”*

- Henri Poincaré

*“The scientist does not study Nature because it is useful to do so. He studies it because he takes pleasure in it, and he takes pleasure in it because it is beautiful. If Nature were not beautiful it would not be worth knowing, and life would not be worth living. I am not speaking, of course, of the beauty which strikes the senses, of the beauty of qualities and appearances. I am far from despising this, but it has nothing to do with science. What I mean is that more intimate beauty which comes from the harmonious order of its parts, and which a pure intelligence can grasp.”

Preface

This work describes an investigation of the level structure of ^{210}Fr using time-correlated γ -ray spectroscopy. The project was suggested by Professor George Dracoulis and Dr Greg Lane. The spectroscopic measurements were made at the Heavy-Ion Accelerator Facility of the Australian National University using the 14UD Pelletron accelerator and the CAESAR array. Two one-week long experiments were performed and relied upon the help of Dr G J Lane, Professor G D Dracoulis, Mr N Palalani and Mr M L Smith. While codes written by Dr G J Lane were used for the sorting of the data and the measurement of, for instance, angular distributions, the detailed analysis and interpretation was performed by me. The coincidence data were analysed by me using the Radware software suite.

Shell model calculations were conducted by myself using existing codes developed in the department by Dr P M Davidson and Professor A P Byrne. The conclusions made for the structure of ^{210}Fr benefited from friendly discussions with Professors A E Stuchbery and A P Byrne as well as my supervisors.

Parts of the work discoursed in this thesis have been presented at the HIAS 2012 meeting, and a partial report has been published:

Levels in ^{210}Fr and the decay of a high-spin, multi-particle isomer
V. Margerin, G. J. Lane, G. D. Dracoulis, N. Palalani, M.L. Smith
EPJ Web of Conferences **35**, 06003 (2012)

I have also been involved in several projects in the γ -group including preliminary experiments for the measurement of the width of the Hoyle state in ^{12}C , a project led by Dr T Kibédi, and an experiment aimed at measuring the g-factors of states in ^{77}Se that is part of the honours project of Ms P Rajan supervised by Professor A E Stuchbery.

Except where acknowledged in the customary manner, the material presented in this thesis is, to the best of my knowledge, original and has not been submitted in whole or in part for a degree at any other university

Vincent Margerin
December, 2012

A handwritten signature in blue ink, appearing to read "Margerin".

Acknowledgements

Before starting I would like to acknowledge the Research School of Physics and Engineering at the ANU for the awarding of a scholarship that allowed me to perform this work.

I was always both excited and frightened by the idea of writing this section. Frightened because, well, I had several tens of pages to write, edit, proofread etc. But it would also mean that I had reached the end. When thinking about who has made the biggest contribution to my work, the first person I think of is my supervisor Greg. His unconditional support and friendship have provided me with an amazing studying atmosphere. I remember a 24 hour rogaine I did which describes this very well. It was in the middle of the night, in the middle of an eucalyptus forest, somewhere in Australia (which in itself is a scary thought). I was having a rest near a camp fire when I heard Greg arriving from quite far away (before I could even see him) and once again in the dark of night it was very good to have his support around some pancakes! I am also greatly indebted to him for giving me the opportunity to teach, something that I did not think I would enjoy that much. So Greg I could not thank you enough for everything I have learnt, and for all the proof-readings! I am also profoundly grateful to George. I have learnt many things from him and I am very happy that I have been always pushed to the high standards he wants, but I must say that he made me discover that coffee icecream way too late in my time in Australia! I'm also thankful to my advisors Andrew and Aidan. Andrew was the first academic I spoke to in English and I have ever since enjoyed our discussions! Also thanks Andrew for your notes on shell model calculations that were really helpful. I also want to thank Tibor, not only for the discussions around BrIcc but also for the lifts after my shifts in the cold and dark Canberra winter. A lot of people have also been very supportive in the Department of Nuclear Physics, so thanks to all of them. In particular Matt who gave me great feedback on my thesis and Maurits for his continuous support and great friendship. I also want to wish good luck to Pal, it's been great studying with you!

There are two people without whom I would have genuinely never submitted

this thesis, thanks so much Petra and Karen for all your help! And to finish the academic acknowledgments I would like to mention the University of Edinburgh which provided me time and space to finish my thesis.

I have met fantastic friends in Australia and they made my life Down Under greater than I thought it would be. So thanks to Jamie, Whitey, Sophie, Kas, Michael, Sagar, Tristan, Tintin, Jeremy (we forgive you for your “exceptional” goalkeeping skills), Sanjay and all the Burgmann crew. I would also like to thank Andreas Scheidegger for introducing me to R, a code through which I could finally “succeed” in programming!

I would also like to thank my mates from the North of France. Matt, Ju (who also helped me to get my French right on the résumé!), Alex, Anne-So, Matt, Marie, Robin thanks so much for being my friends!

Finally all of it would not have been possible without the support of my Mum and Dad, and my (little) sister. Without you this would just not exist. So thanks so much, I am very lucky to have you!

Abstract

The structure of ^{210}Fr has been studied with the $^{197}\text{Au}(^{18}\text{O}, 5\text{n})^{210}\text{Fr}$ reaction. Experiments were performed using the 14UD Pelletron accelerator at the Heavy-Ion Accelerator Facility at the ANU to provide an ^{18}O beam at an energy of 97 MeV. Several structural features have been discovered including the presence of four isomers. A high-spin isomeric state, with spin more likely being 23^+ , has been identified at ~ 4.4 MeV with a lifetime of $686(17)$ ns that decays by two γ -rays at 573.5 and 663.6 keV that are very likely to have either $M2$ or $E3$ multi-polarity. The measured strengths in the case of $E3$ assignments are approximatively 8 and 21 W.u., respectively. These would be less enhanced than is observed in the decay from the high spin isomers in ^{209}Fr and ^{211}Fr that are believed to be from a related configuration. Another isomer at ~ 1 MeV with $J^\pi = 10^-$ and lifetime of ~ 30 ns is found to decay via a hindered $E1$ transition that is j -forbidden. Possible configurations of excited states in ^{210}Fr are discussed within the semi-empirical shell model. Comparisons are made with calculations performed using the code Sesame developed at the ANU.

Résumé

Dans cette thèse, nous étudions la structure du noyau lourd ^{210}Fr grâce à la réaction de fusion $^{197}\text{Au}(^{18}\text{O}, 5\text{n})^{210}\text{Fr}$. Pour ce faire, deux expériences utilisant un faisceau d'oxygène à une énergie de 97 MeV et une cible d'or furent réalisées sur l'accélérateur de particules 14UD Pelletron localisé à l'Heavy-Ion Accelerator Facility de l'Australian National University. Nos investigations révèlent de nombreuses caractéristiques de la structure de ce noyau dont la présence d'un isomère à une énergie d'excitation de 4,4 MeV avec une durée de vie moyenne de ~ 700 ns et un spin de 22 ou 23^+ . L'indécision sur la quantité de spin provient de la nature des rayons gammes désexcitant cet isomère qui peuvent être de multipolarité $M2$ ou $E3$. Dans le cas où ces transitions sont de multipolarité $E3$ alors leur probabilité de transition serait de 8 et 21 W.u., en dessous de ce qui est généralement observé pour les décroissances de niveaux à haut spins dans les noyaux voisins comme les isotopes ^{209}Fr et ^{211}Fr qui ont pourtant été attribués à des configurations coïncidentes avec celles faites ici pour ^{210}Fr . Un autre isomère à 1 MeV et $J^\pi = 10^-$ a une durée de vie moyenne d'environ 30 ns et décroît via une transition $E1$ qui est j -interdite et donc de plus faible probabilité. Les possibles configurations pour les niveaux d'énergie observés dans le noyau ^{210}Fr sont envisagées dans cette thèse en invoquant les problématiques liées au modèle semi-empirique des couches nucléaires. Ces observations sont comparées avec les prédictions du code Sesame développé à l'ANU.

Contents

Preface	v
Acknowledgements	vii
Abstract	ix
Résumé	xi
1 Introduction	1
1.1 The shell model applied near ^{208}Pb and to the nucleus ^{210}Fr	3
1.1.1 Single particle structure	3
1.1.2 Octupole vibration	3
1.1.3 Coupling of single particle excitation and octupole vibration	3
1.1.4 Francium nuclei and rationales for the study of ^{210}Fr	4
1.2 Production of francium isotopes	4
1.3 Why time correlated γ -ray spectroscopy?	6
1.4 Other studies of ^{210}Fr	6
2 Experimental methods	9
2.1 Heavy ion fusion-evaporation reactions	9
2.1.1 Complete fusion (compound nucleus formation)	10
2.1.2 Production of ^{210}Fr	11
2.2 The CAESAR Array	11
2.2.1 Compton Suppression	13
2.2.2 Electronics	13
2.3 Off-line Analysis	17
2.3.1 Calibrations	17
2.3.2 Building matrices and gating	18
2.3.3 Deconvoluting unresolved lines	24
2.4 Measuring internal conversion coefficients	25
2.5 Angular anisotropies for determining multi-polarities	26

2.5.1	The transition $I_i \rightarrow I_f$	26
2.5.2	Angular distribution for an aligned ensemble of nuclei	27
2.5.3	Correlations in gated angular distributions	30
2.6	Techniques for lifetime measurements	30
3	Experimental results	37
3.1	Decay of the high-spin, long-lived isomer	38
3.1.1	States and transitions below the isomer at 2206 keV	41
3.1.2	States and transitions above the isomer at 2206 keV	44
3.2	The level scheme for ^{210}Fr	46
3.2.1	States and transitions below the state at 2206 keV	46
3.2.2	States and transitions above the state at 2206 keV	50
3.2.3	States and transitions on the right hand side of the level scheme	54
3.3	Lifetimes	55
3.3.1	The isomer at 1113 keV	55
3.3.2	The isomer at 2018 keV	57
3.3.3	The isomer at 2206 keV	57
3.3.4	The isomer at 4417 keV	58
3.4	Spin and parity assignments	60
3.4.1	States below the isomer at 2206 keV	61
3.4.2	States below the isomer at 4417 keV	68
3.4.3	States on the right hand side of the level scheme	69
4	The structure of ^{210}Fr	71
4.1	The nuclear shell model	71
4.1.1	Single particle potential and semi-empirical energies	72
4.1.2	Two-body interactions	72
4.1.3	n -nucleon wave function and angular momentum recoupling	75
4.1.4	Calculation of states I - Empirical shell model calculation	76
4.1.5	Calculation of states II - Partial decomposition	77
4.2	Preliminary considerations for configuration assignments in ^{210}Fr	77
4.2.1	Neutron configurations - ^{205}Pb	78
4.2.2	Proton configurations - ^{213}Fr and ^{211}Fr	78
4.2.3	The case of ^{212}Fr	84
4.3	Configuration assignments in ^{210}Fr	86
5	Concluding comments	101
5.1	Experimental measurements and main structural assignments	101

5.2	Shell model calculation	102
5.3	Future work	103
A	Deconvoluting unresolved transitions - an example	105
B	Detailed γ-γ coincidence arguments	109
C	Measurement of total conversion coefficients	113
D	Calculation of the 19^- state energy in ^{210}Fr using partial decomposition	123
E	List of two-body residual interactions used in this work	127
F	Calculation of energy matrix elements using the shell model	133
F.1	The $29/2^+$ state in ^{213}Fr	134
F.2	The W-coefficients	135
	Bibliography	139

Chapter 1

Introduction

“Commençons tranquillement voulez-vous, avant de corser les choses.”

– **Jean Dujardin (as OSS117), in OSS117, Le Caire Nid d’Espions**

The atomic nucleus is a unique system to study. It is a quantum object made of a number of fermions, too few for it to be treated in the limit as if it were an infinite size object, and too many for all of its properties to be calculated from first principles using the individual nucleon-nucleon interaction. The nucleus, however, can exhibit different limiting behaviours that can, fortunately, be explained with more accessible pictures. The experimental investigation of the energy level properties is consequently important for testing these simplified theories. In one such theory, the angular momentum is only carried by a few particles outside a stable core, whereas in another the bulk of the constituents behave collectively. Although these behaviours are distinct, it is possible for both single particle excitation and collective motion to compete in one nucleus, at similar energies. In fact, on a detailed fundamental level the collective behaviours are a sum over the motion of many individual nucleons.

This thesis is mainly focussed on a multi-particle description of the nucleus. The important feature that simplifies the description is the so-called shell structure; the motion of nucleons in the nucleus can be understood in an analogous way to that of the electronic cloud of an atom, where the electrons fill orbitals having particular energy and angular momentum, resulting in a shell structure. The governing interaction in the nucleus is, however, different from that of the atom. In the latter it is the electromagnetic interaction that dictates the shell gaps found at electron number 2, 10, 18, 36 etc. corresponding to the noble gases that are especially stable since their electron shells are full.

The behaviour of the Z protons and N neutrons of the nucleus is, however, mainly governed by the strong nuclear force and, in particular, a large spin orbit coupling, although the Coulomb interaction still plays an active role. The different interaction leads to a change in the favoured numbers compared to the atoms, and the nuclear shell gaps, also called *magic numbers*, are found at Z (or N)=2, 8, 20, 28, 50, 82 and 126¹.

Experimentally, this is confirmed by the observation of an increased binding energy (stability) for nuclei containing a magic number of protons or neutrons (see Figure 1.1) analogous to noble gases in atomic physics.

In this description, nuclei close to the magic numbers can be explained in terms of the few valence nucleons or holes occupying levels near the shell closures.

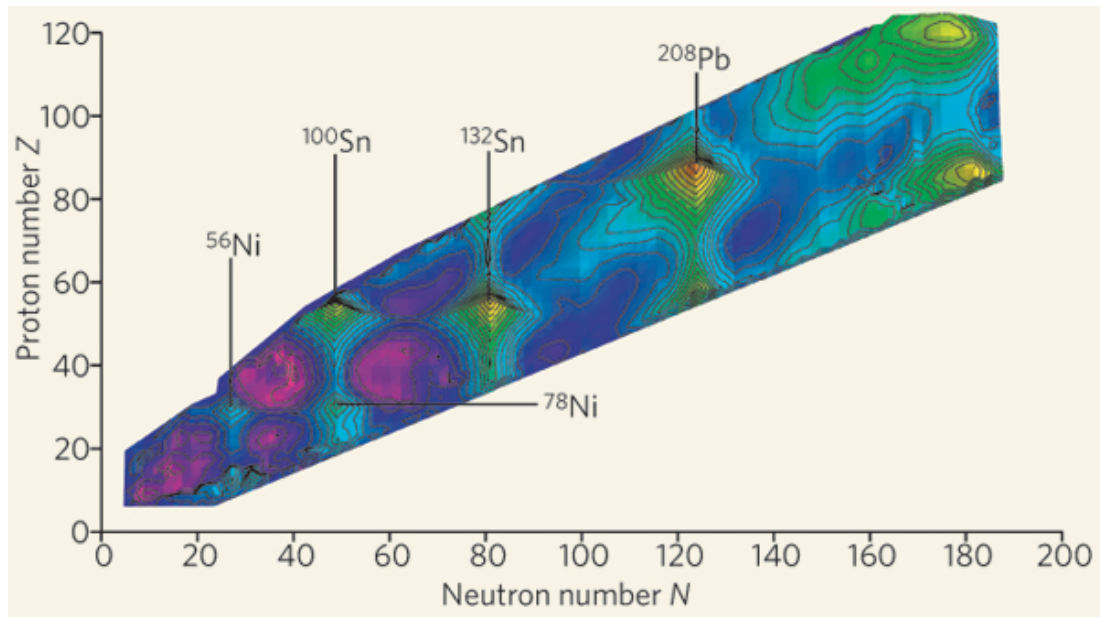


Figure 1.1: Binding energy for known nuclei. The colour spectrum, from violet to red, indicates the excess/depletion in binding energy, from less to more bound. This picture is taken from Ref. [Beng 07].

¹The shell closure at 126 is only known for neutrons and the occurrence of such a gap for protons has not yet been experimentally confirmed as an element with such a proton number has not yet been produced. The next proton shell gap is likely to be different to 126 as in such heavy nuclei the Coulomb force is starting to become more and more significant.

1.1 The shell model applied near ^{208}Pb and to the nucleus ^{210}Fr

1.1.1 Single particle structure

The heaviest doubly-magic nucleus known is ^{208}Pb ($Z=82$, $N=126$). As a first approximation, this nucleus can be seen as inert so that the energy levels in nearby nuclei are due to excitation of the valence nucleons within the orbital space available. For instance the ground state of ^{209}Pb and the first two excited states at 779 and 1421 keV have spin and parity $9/2^+$, $11/2^+$ and $15/2^-$ [DoE 12], respectively, corresponding to a neutron in the $g_{9/2}$ ($\ell = 4$) orbital (in the ground state) being excited first to $i_{11/2}$ ($\ell = 6$) and then to $j_{15/2}$ ($\ell = 7$).

1.1.2 Octupole vibration

Around the lead core, proton and neutron orbitals have high angular momentum (see Figure 1.2). This creates a lot of possibilities for (allowed) $\Delta j = \Delta\ell = 3$ excitations between single particle orbitals, resulting in a low-lying 3^- vibrational state in ^{208}Pb at 2615 keV. The octupole phonon is a superposition of particle/hole excitations resulting in an oscillating shape that is, on average, spherical. The nucleus decays to the ground state via an $E3$ transition, that is a γ -ray that carries three quanta of angular momentum ($j = 3\hbar$) and changes the parity. Due to the coherent nature of the motion, this $E3$ transition is enhanced over single-particle values. This 3^- excitation often plays an important role.

1.1.3 Coupling of single particle excitation and octupole vibration

In nuclei with up to several valence particles/holes outside a ^{208}Pb core, it is possible for transitions to proceed through single-particle de-excitations that are coupled to the 3^- phonon, if the correct orbitals are part of the parent and daughter state configurations. This can generate enhanced $E3$ transitions. Since $E3$ transitions are inherently slow, the parent states often exhibit a lifetime, and the observed lifetimes for $E3$ -decaying states in the region of ^{208}Pb often imply enhanced $E3$ transition strengths that can in turn indicate that the states involved in the transition are coupled to the octupole vibration. In the region of the chart of the nuclide going from Tl ($Z=81$) to Th ($Z=90$), the coupling of single particle excitation and the 3^- phonon is well known for both the proton $\tilde{i}_{13/2} \rightarrow \tilde{f}_{7/2}$ and the neutron $\tilde{j}_{15/2} \rightarrow \tilde{g}_{9/2}$ transitions (see for example [Bohr 69]). (The tilde

signifies that the states are actually superpositions of the single particle excitation with a coupling of the 3^- phonon, for example $|\tilde{i}_{13/2}\rangle = |i_{13/2}\rangle + |f_{7/2} \otimes 3^-\rangle$, for which the strength has been measured at $\sim 32(2)$ W.u. [Haus 72].)

1.1.4 Francium nuclei and rationales for the study of ^{210}Fr

Francium isotopes ($Z=87$) have been extensively studied prior to this work, with all isotopes from $A=208$ to $A=215$ (see Refs. [Drac 09b, Drac 09a, Byrn 86b, Byrn 94, Drig 85]) having high-spin level schemes known, except ^{210}Fr . The nuclei in this range are all spherical; lower mass isotopes have been not, or only partially, investigated but they are more likely to be past the transition to deformed nuclei, while heavier francium nuclei have clear rotational band structures corresponding to a pear shaped (octupole) deformation [Debr 90]. Therefore ^{210}Fr is the last francium nucleus that is expected to be spherical but is not known at high-spins. The available orbitals for ^{210}Fr , in the framework of the shell model, are shown in Figure 1.2.

Together with the structural expectations discussed below, this fact motivated the present work for several reasons. Both types of coupling generating enhanced $E3$ γ -rays have been observed in nearby francium nuclei and might occur in ^{210}Fr . The proton $\tilde{i}_{13/2} \rightarrow \tilde{f}_{7/2}$ transition is expected to arise below 5 MeV, as measured in ^{209}Fr [Drac 09a] and ^{211}Fr [Byrn 86b], the direct neighbours of ^{210}Fr . The neutron hole $\tilde{j}_{15/2} \rightarrow \tilde{g}_{9/2}$ transition, however, has been measured higher in energy, at around 6 MeV in ^{212}Fr [Byrn 86b].

Another motivation for the investigation of ^{210}Fr is the systematic observation, in odd-odd neutron deficient nuclei near ^{208}Pb , of isomeric 10^- states that decay by j -forbidden transition(s) (principally $E1$, $M2$ or $E3$). This decay is due to the $\nu i_{13/2}^{-1} \rightarrow f_{5/2}^{-1}$ transition (the proton component does not change) and hence the γ -rays observed are all j -forbidden. The observation of a 10^- isomer in ^{208}Fr , together with a new measurement for the lifetime of a 10^- isomer in ^{206}At , was the subject of a recent letter by Dracoulis *et al.* [Drac 09b]. Details of the 10^- isomer in a range of odd-odd neutron deficient nuclei in the lead region are listed in Chapter 4. A related $13/2^+$ isomer is systematically observed in even Z , odd N nuclei.

1.2 Production of francium isotopes

Francium isotopes (87 protons) can be created through the fusion of several beam/target combinations including gold with oxygen, thallium with carbon and

1.2. PRODUCTION OF FRANCIUM ISOTOPES

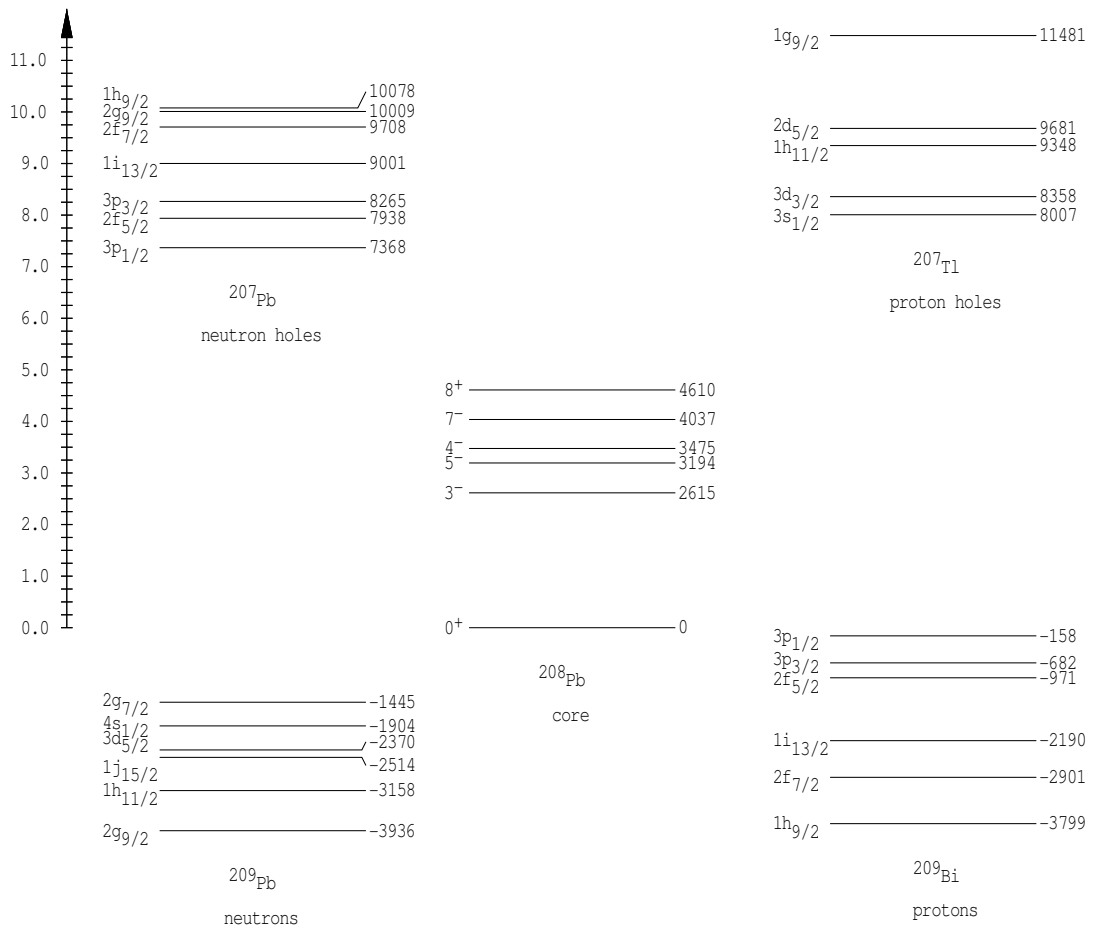


Figure 1.2: The main orbitals, and associated excitation energies, involved in the formation of excited states in ^{210}Fr .

lead with boron. The choice of the reaction will be discussed in Chapter 2 together with other experimental methods required for time-correlated γ -spectroscopy.

1.3 Why time correlated γ -ray spectroscopy?

Time correlated γ -ray spectroscopy is a powerful tool to gain insight into the structure of a nucleus. It allows derivation of the nuclear level scheme that shows measured states, with their associated spins, parities and lifetimes, and the transitions between them. Photons are emitted by unstable nuclei as they de-excite. The measurement of their characteristic properties such as the energy and multi-polarity, gives information about the parent and daughter states in the transition. Time correlated γ -ray spectroscopy provides a means to achieve direct and/or indirect measurement of such properties.

The electromagnetic nature of radiation (electric or magnetic, dipole, quadrupole or higher multi-polarity) can, for example, be inferred from the angular distribution of emission of γ -ray. The change in spin and parity between parent and daughter states also has an impact on the probability whether the transition will undergo internal conversion, a process where the energy of the transition is transferred to an atomic electron. The probability for internal conversion can be directly deduced from conversion electron measurements or inferred from intensity balances. Because of the shell structure of the atom discussed above, internal conversion is either derived for the total number of electron shells (K, L, M, ...) in which case the coefficient is called α_T , or for individual electron shells, α_K , α_L ... The use of these methods to determine multi-polarities will be discussed in Chapter 2.

Further insight into the nuclear structure can be gained through lifetime measurements. Lifetimes are, here, either measured directly, i.e. relative to the beam pulsing, or alternatively by looking at the intermediate time between γ -rays populating and depopulating states. These techniques will be detailed in Chapter 2.

1.4 Other studies of ^{210}Fr

While no high-spin structure investigation had been reported for ^{210}Fr prior to this work, the α -decay of ^{214}Ac into ^{210}Fr has been studied by Kuusiniemi *et al.* [Kuus 04] and numerous low-spin states were reported. An investigation of excited states in ^{210}Fr from a study primarily focussed on ^{209}Fr was published [Meye 06] some years before this study, but the results were proven to be erro-

1.4. OTHER STUDIES OF ^{210}Fr

neous in Ref. [Drac 09b] (see also Chapter 2). Towards the end of the present investigation, a report on high-spin states and transitions in ^{210}Fr by Kanjilal *et al.* [Kanj 11] appeared in the literature, although the results from the present work show significant disagreement.

CHAPTER 1. INTRODUCTION

Chapter 2

Experimental methods

“Comment voulez vous gouverner un pays avec plus de trois cents sortes de fromage!”
– **Charles de Gaulle**

This chapter presents experimental techniques, focussing on those used in this thesis. The first sections describe the rationales for the use of heavy-ion fusion reactions and the experimental set up used to realise those reactions. The later sections will focus on analytical methods, including the extraction of information for the building of the level scheme from γ - γ -time coincidences and the determination of multi-polarities and lifetimes.

2.1 Heavy ion fusion-evaporation reactions

Excited energy levels in nuclei can be populated through several methods including heavy ion fusion, neutron capture, γ - or particle-induced excitation. Nevertheless for the population of high spin states in nuclei, heavy ion reactions are the standard method, especially for the case of neutron-deficient nuclei. Introductory [Newt 74] and more complete reviews (see, for example, Refs. [Bass 80, Thom 68, Boda 62, Pelt 82]) are available on this subject, while study of the reaction process itself is an active field of research. In this section the formation of the compound nucleus and its decay leading to the production of nuclei at high-spin are discussed; other aspects are outside the scope of this work.

2.1.1 Complete fusion (compound nucleus formation)

An ion with kinetic energy above the Coulomb barrier, E_{CB} , can fuse with an atomic nucleus of the target resulting in the formation of a compound nucleus. This process can be explained via classical considerations.

In the incoming channel of a heavy ion reaction, the projectile, with charge Z_1e , and the target, with charge Z_2e , experience the Coulomb potential and the centrifugal potential:

$$V(r) = V_{EM}(r) + V_{cen}(r), \quad (2.1)$$

where

$$V_{EM}(r) = \frac{1}{4\pi\varepsilon_0} \frac{Z_1 Z_2 e^2}{r}, \quad (2.2)$$

$$V_{cen}(r) = \frac{\ell(\ell+1)\hbar^2}{2\mu r^2}, \quad (2.3)$$

and μ is the reduced mass of the two-body system. At the nuclear interaction radius ($r_{int} = R_1 + R_2$) the electromagnetic potential is the Coulomb barrier $V_{EM}(r_{int}) = V_{CB}$. The angular momentum $\ell\hbar$ brought into the system by the fusion reaction can be estimated at the point of interaction by:

$$\ell(\ell+1) = \frac{2\mu(r_{int})^2}{\hbar^2} (V_{CB} - E_{cm}), \quad (2.4)$$

where E_{cm} is the energy of the projectile in the centre of mass frame. The ground state spin of the fusing nuclei, ℓ_1 and ℓ_2 , must also be considered in Eq. 2.4, this is defined by $\ell_{(12)} \in [-(\ell_1+\ell_2), (\ell_1+\ell_2)]$. Taking the nuclear radii as $R = R_0 A^{1/3}$ and using the approximation $\ell(\ell+1) \approx \ell^2$ gives:

$$\begin{aligned} \ell &= \frac{R_0(A_1^{1/3} + A_2^{1/3})}{\hbar} \sqrt{2\mu(V_{CB} - E_{cm})} + \ell_{(12)} \\ &\approx 0.226 \times (A_1^{1/3} + A_2^{1/3}) \sqrt{2\mu(V_{CB} - E_{cm})} + \ell_{(12)}, \end{aligned} \quad (2.5)$$

where V_{CB} and E_{cm} are in MeV. As a result the second line of Eq. 2.5 is in units of \hbar . The Fermi radius R_0 has been taken as 1.5 fm [Kran 88]¹. The cross section can also be obtained:

$$\sigma_r = \pi r_{int}^2 \left(1 - \frac{V_{CB}}{E_{cm}}\right), \quad (2.6)$$

valid for $E_{cm} > V_{CB}$.

¹In the relationship $R = R_0 A^{1/3}$, R_0 is typically taken to lie between 1.2 and 1.5 fm [Kran 88].

2.2. THE CAESAR ARRAY

2.1.2 Production of ^{210}Fr

Depending on the excitation energy of the compound system, several evaporation channels compete (xn , yp , $z\alpha \dots$), where n , p and α are emitted neutrons, protons and alpha particles respectively, and x , y and z are the number of particles emitted. Following the formation of the compound nucleus, neutron evaporation is, in the region of interest for this work, roughly a factor of ten more probable than other types of evaporation [Newt 74]. As a result, it is preferable to choose the beam and the target so that the compound nucleus already has the desired number of protons. Some of the possible combinations of beam and target for the production of ^{210}Fr are presented in Table 2.1. An excitation function based on statistical model calculations performed with the program PPACE is presented in Figure 2.1 and shows that the $^{197}\text{Au}(^{18}\text{O}, 5n)^{210}\text{Fr}$ reaction is favourable. Gold is, furthermore, experimentally very convenient to use. It is easy to prepare, mono-isotopic and appears to be a good “hyperfine” host² for the recoil nuclei if they are stopped in the target. The maximum cross section for production of ^{210}Fr is predicted at roughly 94 MeV. A choice of 97 MeV for the beam energy means that, for a 5 mg/cm² target (thick enough to stop the recoiling fusion products), the energy loss will be around 10 MeV, integrating across the peak of the cross section. Other (known) nuclei, such as ^{211}Fr , are produced in reasonable quantities and can be used for calibration in some cases.

2.2 The CAESAR Array

Time-correlated γ -ray spectroscopy was performed using the CAESAR³ array at the Heavy-Ion Accelerator Facility at the Australian National University. The array consists of two types of detectors: **H**igh **P**urity **G**ermanium (HPGe) detectors and **L**ow **E**nergy **P**hoton-**S**pectrometers (LEPS). Six of the HPGe are placed in the vertical plane and form a set of three, well-defined, angles ($\pm 48^\circ$, $\pm 97^\circ$ and $\pm 145^\circ$) with respect to the beam direction. The three other HPGe detectors are

²Hyperfine interactions attenuate the alignment of the angular momentum that gives rise to an angular dependence of the γ -ray emission intensity (see Section 2.5). In the present work, the angular intensity distribution for the 728.4 keV $E3$ transition in ^{211}Fr , decaying from a 178 ns isomer at 4657 keV, is measured to be $A_2/A_0 = +0.27(4)$ similar to the value measured by Byrne *et al.* [Byrn 86b] ($A_2 = +0.29(2)$, $A_4 = +0.01(3)$), who used liquid mercury to perform angular distribution measurements. Liquid Hg has very well defined molecular structure and the hyperfine interaction is virtually zero. However for the study of ^{210}Fr , the use of a liquid Hg target was not appropriate.

³CAESAR comes from an acronym for Compton Suppressed Array, CSA pronounced “Cee-Z-a” by the Australians.

CHAPTER 2. EXPERIMENTAL METHODS

Table 2.1: Beam and target combinations for the production of ^{210}Fr and their previous use for the production of related nuclei.

Beam	Target	Energy range (MeV)	Evaporated neutrons to produce ^{210}Fr	Comments
$^{12,13}\text{C}$	^{203}Tl	77–96	5 or 6	Used for $^{211,212,213}\text{Fr}$ (^{205}Tl target also used) by Byrne <i>et al.</i> [Byrn 86b].
$^{16,17,18}\text{O}$	^{197}Au	82–99	3, 4 or 5	^{16}O used by Dracoulis <i>et al.</i> for ^{209}Fr [Drac 09a]. Relatively high cross section for ^{208}Fr [Drac 09b].
^{37}Cl	^{176}Yb	173–185	3	Used by Meyer <i>et al.</i> [Meye 06] for $^{209,210}\text{Fr}$, although assignments were erroneous (see Ref. [Drac 09a]).
^{17}O	^{197}Au	88–102	5	Used in this work.

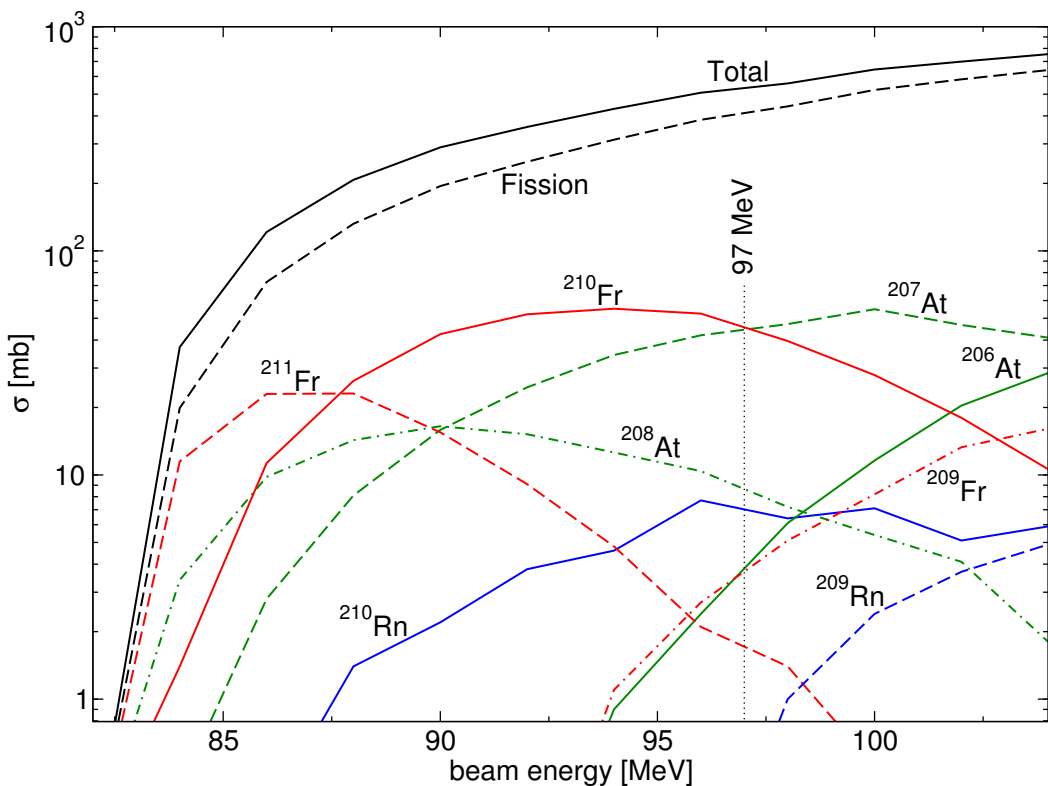


Figure 2.1: Calculated cross sections for the reaction of $^{197}\text{Au}+^{18}\text{O}$ as a function of the laboratory beam energy.

2.2. THE CAESAR ARRAY

out of the vertical plane, at approximatively 49° , 53° and 132° with respect to the beam axis. These nine detectors are surrounded by Bismuth Germanate shields (BGO) for Compton suppression (see below). The two LEPS detectors are also out of the vertical plane, at angles of $\sim 70^\circ$ and $\sim 135^\circ$ with respect to the beam axis, and are *not* Compton suppressed.

2.2.1 Compton Suppression

One of the obstacles in γ -ray spectroscopy is the presence of background that may obscure a peak relevant to the nucleus under study. Compton events where a γ -ray scatters out of the detector, give rise to partial energy deposition and a continuous background in the energy spectra. Methods have been developed to suppress as many of the Compton scattered events as possible. Compton suppression in the CAESAR array is performed by surrounding the HPGe detector with a Bismuth Germanate (BGO) suppressor. Because of the high Z of the BGO, γ -rays Compton scattering out of the germanium crystal have a high probability to be detected by the suppressor and coincidence logic can be used to suppress the associated HPGe signal.

More recent detector systems can track the path of the γ -rays as they scatter/absorb within the array and reconstruct the full energy signal from the original γ -ray (for example AGATA [Nybe 12] and GRETINA).

2.2.2 Electronics

The electronics set up for the coincidence logic for the CAESAR array dates back to many years ago and has been continuously developed since then.

The electronics for CAESAR and a schematic picture of how the signals propagate through the electronics are presented in Figure 2.3. When the low-energy beam chopping is used (such as for the experiments run as part of this work), the accelerator provides beam pulses that are multiples of 107 ns apart. Signals derived from the chopper are a natural reference to use so as to measure γ -ray arrival times with respect to the beam bursts. The various timing signals, consequently, are in general some multiple of the beam pulse width. For example, in the first experiment the beam was 1:15 pulsed (beam bursts 1712 ns apart) so that the signals used to define coincidences (out of the fast. Discr. LRS821 after “A1” and “A2” in Figure 2.3) are $\Delta T = 856$ ns. This results in a maximum time difference between two coincident γ -rays (± 856 ns) that cannot exceed the separation between beam pulses (1712 ns).

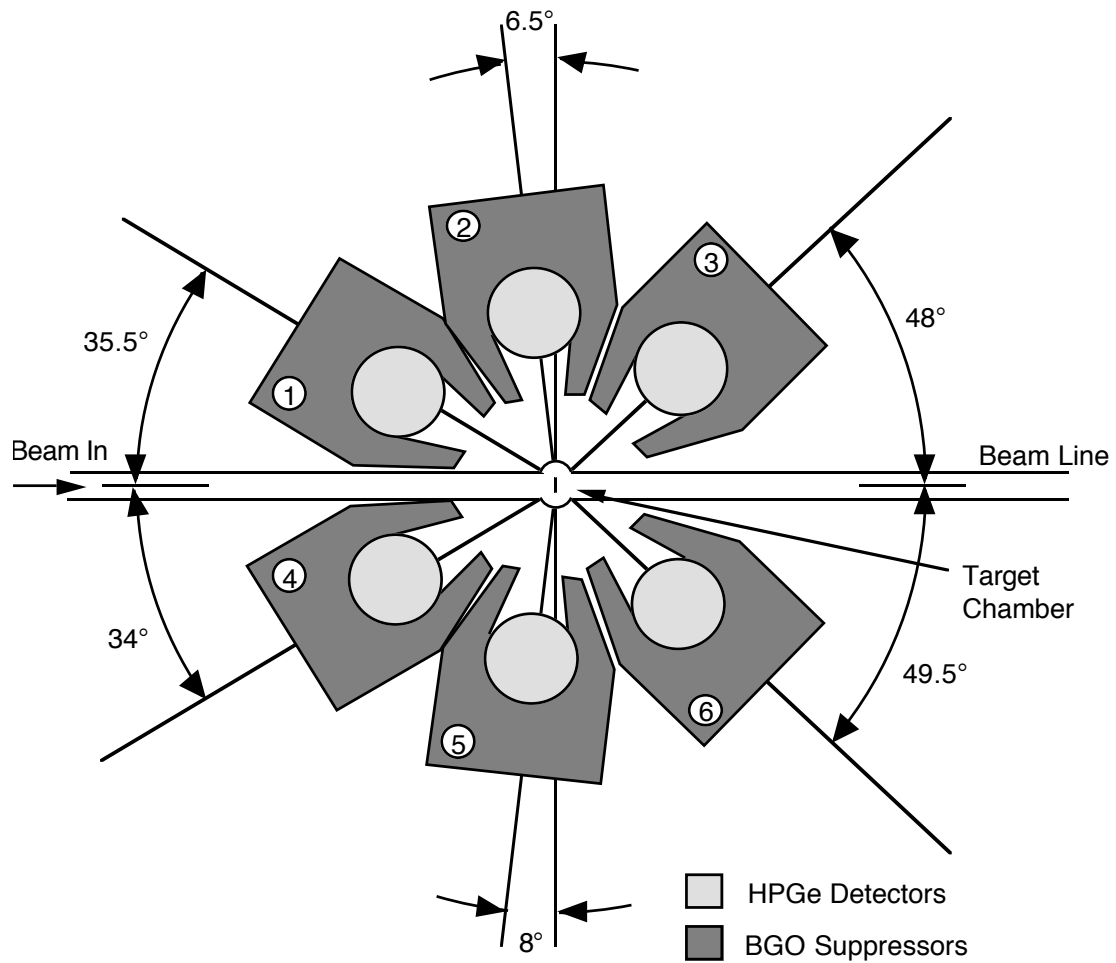


Figure 2.2: Schematic diagram of the CAESAR array for the six detectors in the vertical plane. The target denoted by the bar in the middle of the target chamber is oriented at a $\sim 70^\circ$ angle with respect to the beam to minimise self absorption of γ -rays in the target (i.e. all detectors are evenly exposed to the target). The HPGe detectors enter the BGO suppressors from the side (asymmetric type).

2.2. THE CAESAR ARRAY

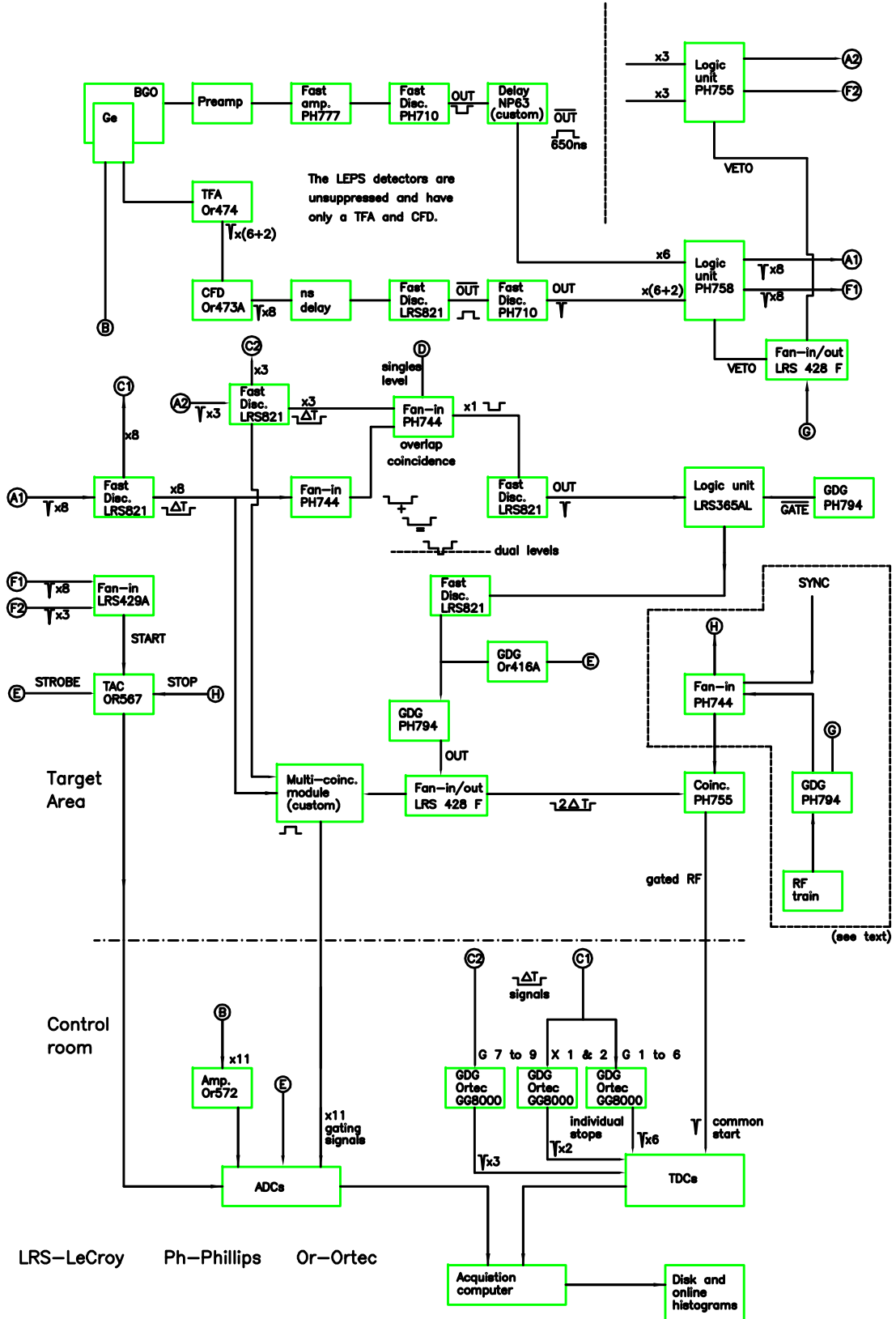


Figure 2.3: Circuit diagram for the electronics of the CAESAR array. Adapted from Ref. [Lane 95]

Compton Suppression (CS)

When one of the germanium detectors fires, one of the output signals is sent through a Timing Filter Amplifier (TFA) and a Constant Fraction Discriminator (CFD). This fast signal is delayed and checked against the arrival of a signal from the associated suppressor in the PH758 Logic Unit. The suppressor signal is made 650 ns wide allowing for the coincident signal from the HPGe to be tagged as a Compton event. Only valid (unsuppressed) signals are allowed onward into the logic circuit. LEPS signals pass through without suppression.

Timing signals and coincidence logic

The valid signals are sent to a Fast Discriminator (Fast. Disc. LRS821) which creates negative pulses for each of the eleven detectors (see symbol x11 in Figure 2.3) of ΔT width. These are then fanned out. One set of outputs is sent to two fan-in/out in series, PH744 and LRS428F, respectively, in order to sum these signals. The LRS821, after the two fan-in modules, discriminates below (a Fast. Disc. triggers on a negative signal) a level chosen to select out coincidence events and produces a fast-timing negative output, which is stretched into two Gate and Delay Generators (GDG). (In order to measure single γ -ray events a fake constant level can be provided at the fan-in.) Note that the signal is now $2\Delta T$ in width. One of the GDGs (OR416A) produces a positive signal (“E”) that indicates that a valid coincidence has been detected and this is used as a master gate for various purposes, for example, triggering the data acquisition.

The output from the other GDG (PH794) is used to generate the gated RF by overlapping a $2\Delta T$ wide signal with the signal train from the pulsing in the PH755 module. This gives a time relative to the beam pulsing that is used as the common start of the TDC. Thus the individual time of detections for γ -rays are measured relative to the beam pulsing. The times of γ -rays relative to each other can then be derived from differences between those times.

Time to Amplitude Converter (TAC)

A Time to Amplitude Converter (TAC) is also used to measure the time of γ -rays with respect to the beam pulses. In order not to have the TAC continuously triggering, it is started when there is a valid event and stopped with a signal in phase with the beam bursts. The suppressed signals from all the detectors are combined into a common start signal and the stop is triggered on the beam “synch” signal (which drives the chopper). The TAC is also strobed, meaning that the output is provided only upon receipt of an external trigger, in this case

2.3. OFF-LINE ANALYSIS

the master gate signal (the output of the GDG OR416A).

Prompt Veto

In a long chopping experiment, where only out-of-beam γ -rays are to be collected, the signals due to prompt in-beam γ -rays can be suppressed by adjusting the delay (GDG PH794) on a signal derived from the beam pulsing to generate a veto signal to suppress the signals at points “A1” and “A2” in the electronics circuit (see Figure 2.3).

Data acquisition

The Amplitude to Digital Converters (ADC) are triggered by the output of a multi-coincidence module so that only valid coincident events are converted. The ADCs record the (slow) energy signals that come from the HPGe detectors via the OR572 amplifiers.

The signals recorded in the ADCs and TDCs (γ -ray energy and times) are written to disk. The timing and coincidence logic set up by the electronics provides flexibility on the types of time correlated analysis that can be performed off-line.

2.3 Off-line Analysis

2.3.1 Calibrations

Gain-matching and aligning ADC and TDC spectra

The gains on the amplifiers and ADCs are set up such that all of the nine HPGe detectors produce roughly 0.5 keV/channel raw signals (0.2 keV/channel for the LEPS) and such that the zero offset is small. Fine matching of the detectors is done off-line to enable their addition and create summed spectra. Similar procedures are required for time spectra. Typical ADC and TDC spectra are shown in Figures 2.4 and 2.5. Energy spectra were matched initially using radioactive sources and then using internal peaks. In this work, strong lines from ^{211}Fr were used to obtain gain matching. The use of ^{211}Fr has the advantage of performing gain-matching under the actual experimental conditions in which the data for ^{210}Fr were collected. Each saved set of data (a “runfile”) was gain matched separately and then summed together. A similar process can be applied to the TDC spectra with the noticeable difference that all TDC spectra have the same time dispersion. The prompt time peak, however, does not have a defined position

and therefore an arbitrary value (e.g. the actual position for detector 1) can be chosen and all TDCs aligned to it (ten offsets must be derived). TDC differences between each detector give the time difference between two γ -rays. The fifty five ($[11 \times 10]/2$) TDC time-difference spectra were aligned by optimising, through a χ^2 -minimisation method, the offsets between the t_0 ($\Delta T=0$) and the arbitrary reference value.

Efficiency calibration and/or efficiency matching

Unlike energy gain matching, efficiency calibration could not be done through the use of known nuclei produced in the reaction because the relative intensities are not known to sufficient accuracy. Efficiency calibration functions (see Figure 2.6) were therefore determined from relative intensity ratios using ^{152}Eu and ^{133}Ba sources. The long-lived activity of the reaction products can also be used to check the efficiency calibration. While activity is produced continuously during the experiment, γ -ray spectra are recorded just after the beam is (finally) turned off at the end of the experiment with the coincidence trigger set on singles to specifically measure activity. Long lived nuclei emit γ -rays isotropically at this stage. As a result, the intensity of γ -rays from activity should be the same in all detectors. This can also be checked in the run files since EC-capture and/or α -decay product can be prominent and provide peaks to challenge the calibration. (For example the 395.5, 477.0 and 700.6 keV γ -rays from ^{206}Po are only coming from decay of the reaction products.) Angular distribution values for transitions in ^{211}Fr [Byrn 86b] were also reproduced as a check of the efficiency calibration (see Section 2.5).

2.3.2 Building matrices and gating

The most convenient way to analyse the recorded coincidence data is to sort it into matrices. A matrix records the number of coincidences observed between a pair of detectors, as a function of the channel numbers (subsequently calibrated). These matrices can be of different types. A HPGe vs. HPGe matrix represents $\gamma\text{-}\gamma$ coincidences between some combination of pairs of the nine HPGe detectors. To measure the intensity of a γ -ray as a function of the angle of emission, the procedure is to arrange particular detectors at one angle on one axis against all of the rest on the other. A $\gamma\text{-}X$ matrix contains the information for the coincidences between the HPGe detectors and the LEPS detectors.

There are limitations on the fold (number of coincident γ -rays) achievable

2.3. OFF-LINE ANALYSIS

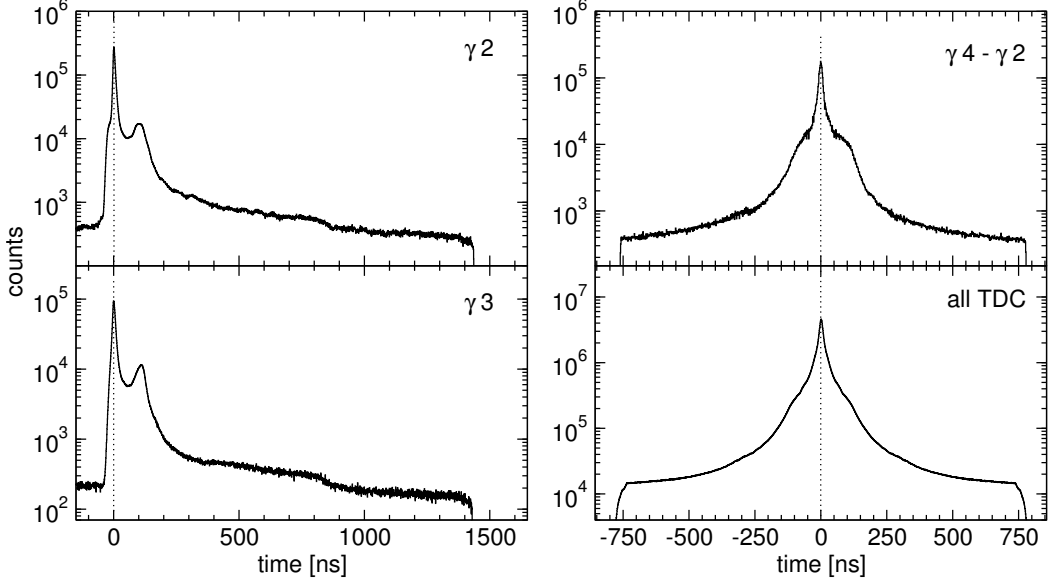


Figure 2.4: Selected spectra showing the absolute γ -ray times and the time difference between detector pairs (“all TDC” is a sum that includes all HPGE and LEPS detector pairs).

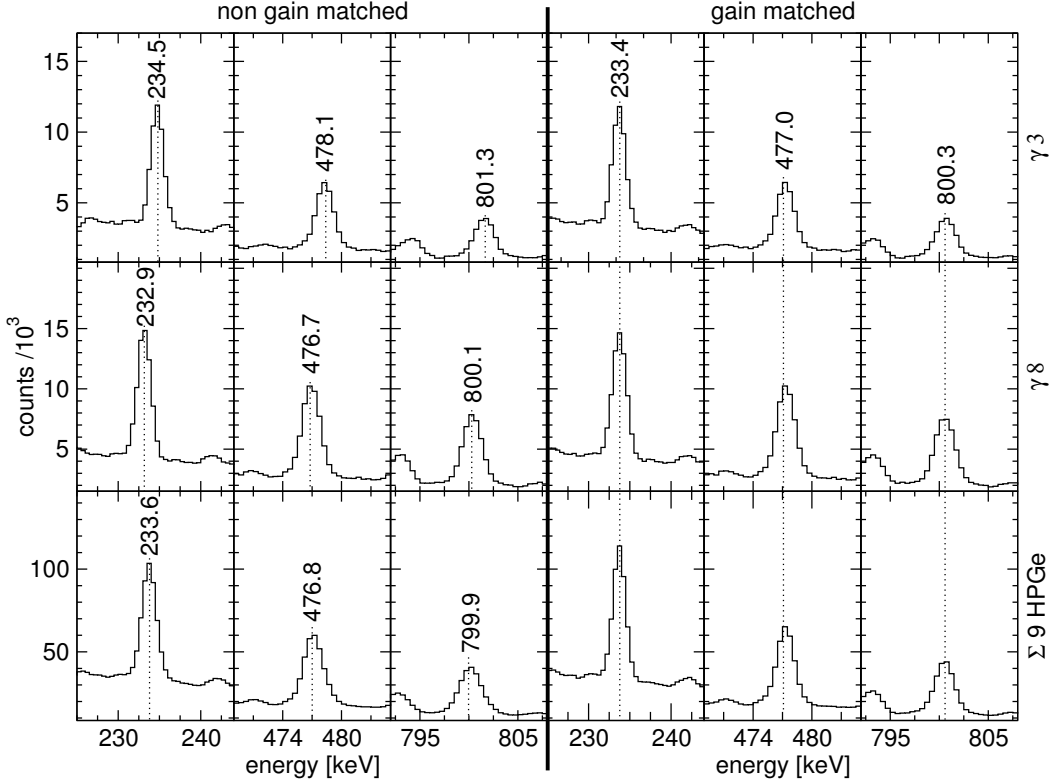


Figure 2.5: Energy spectra before (left) and after (right) gain matching, assuming a 0.5 keV/channel energy calibration (with zero offset), and showing the need for gain matching after calibration. The peaks shown correspond to transitions in ^{211}Fr (nominal known energies of 233.4 and 800.3 keV) and ^{206}Po (477.0 keV), energy labels refer to the fitted centroid of the peaks. Results are shown for two individual HPGe detectors (γ_3 and γ_8) as well as for the sum of all nine HPGe detectors.

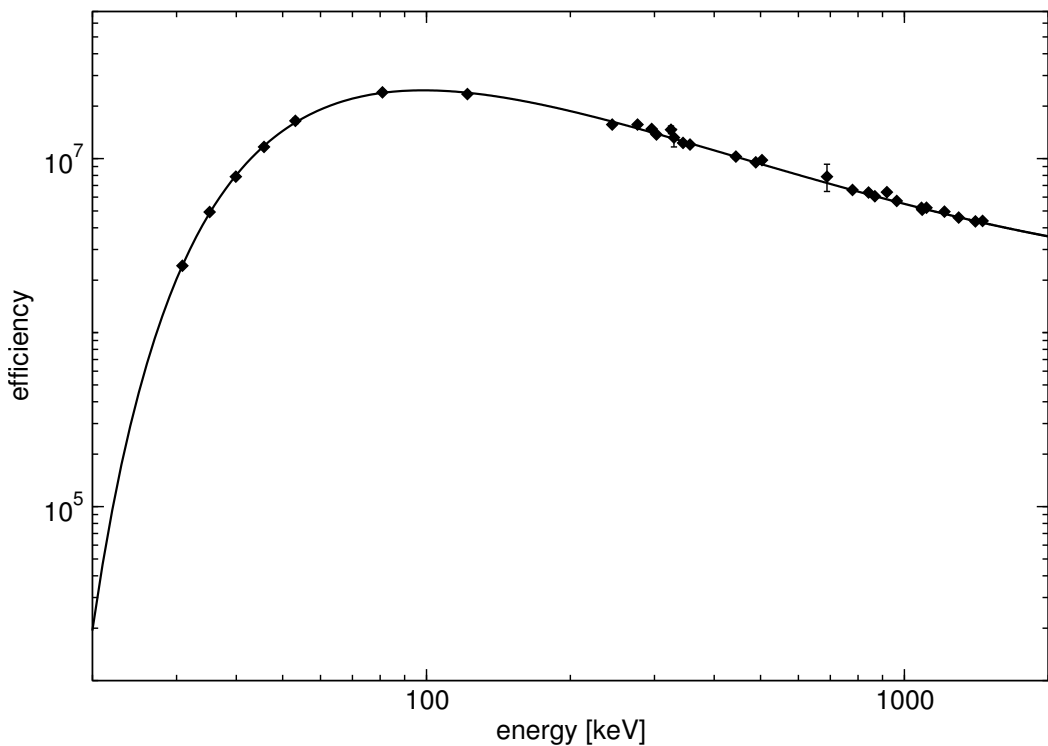


Figure 2.6: Combined efficiencies of the nine HPGe detectors obtained by comparing observed intensities in ^{152}Eu and ^{133}Ba to their known values (Ref. [LNHB 12]). The fit is based around a sum of log-log polynomials (see Ref. [Radf 95] for details).

2.3. OFF-LINE ANALYSIS

with the CAESAR array. The summed efficiency of all detectors is of the order of 1% (effectively close to the solid angle covered by the detectors). The CAESAR array is optimal for 2-fold events and only a small proportion of 3-fold events are recorded.

Time cuts and gates in the multi-dimensional coincidence space

A two-fold event can be represented in a three dimensional space that spans the two γ -ray energies and the time difference between them (see Figure 2.7). (There are also an additional pair of dimensions which are the absolute times of detection for each γ -ray.) Matrices can be produced by reducing the dimension of this space to both specific times with respect to the beam and a specific coincidence overlap times. For example, one can specify an absolute time window within which the event must have happened and project the corresponding $\gamma\gamma$ coincidence matrix (with appropriate cuts on the time difference) in order to look at, for example, events that were recorded in-beam. Similarly, time spectra can be obtained by reducing the two energy axes to the energies of a specific pair of γ -rays and projecting the time difference between the pair. A range of time cuts used in this work are shown in Figure 2.8 and summarised in Table 2.2. Figure 2.7 shows how to gate on absolute times and time differences, gating on the energy is similar.

Table 2.2: Time conditions that were applied for the main set of matrices used in the present work.

matrix name	Absolute time		Time diff. ΔT (ns)
	T_{γ_1} (ns)	T_{γ_2} (ns)	
prompt narrow	$-25 \rightarrow +30$	$-25 \rightarrow +30$	$-30 \rightarrow +30$
prompt wide (p. w.)	$-25 \rightarrow +150$	$-25 \rightarrow +150$	$-150 \rightarrow +150$
narrow	$-25 \rightarrow +1415$	$-25 \rightarrow +1415$	$-30 \rightarrow +30$
wide	$-25 \rightarrow +1415$	$-25 \rightarrow +1415$	$-150 \rightarrow +150$
out-of-beam short	$+30 \rightarrow +150$	$+30 \rightarrow +150$	$-150 \rightarrow +150$
out-of-beam long (o. b. l.)	$+150 \rightarrow +1415$	$+150 \rightarrow +1415$	$-150 \rightarrow +150$
early-delayed short	$-25 \rightarrow +1415$	$-25 \rightarrow +1415$	$+30 \rightarrow +150$
early-delayed long	$-25 \rightarrow +1415$	$-25 \rightarrow +1415$	$+150 \rightarrow +856$
p. w. - o. b. l.	$-25 \rightarrow +150$	$+150 \rightarrow +1006^1$	$-856 \rightarrow +856$

¹ The maximum time difference between two γ -rays is $\Delta T = 856$ ns. Therefore the absolute maximum time for this cut is $150 + 856 = 1006$ ns.

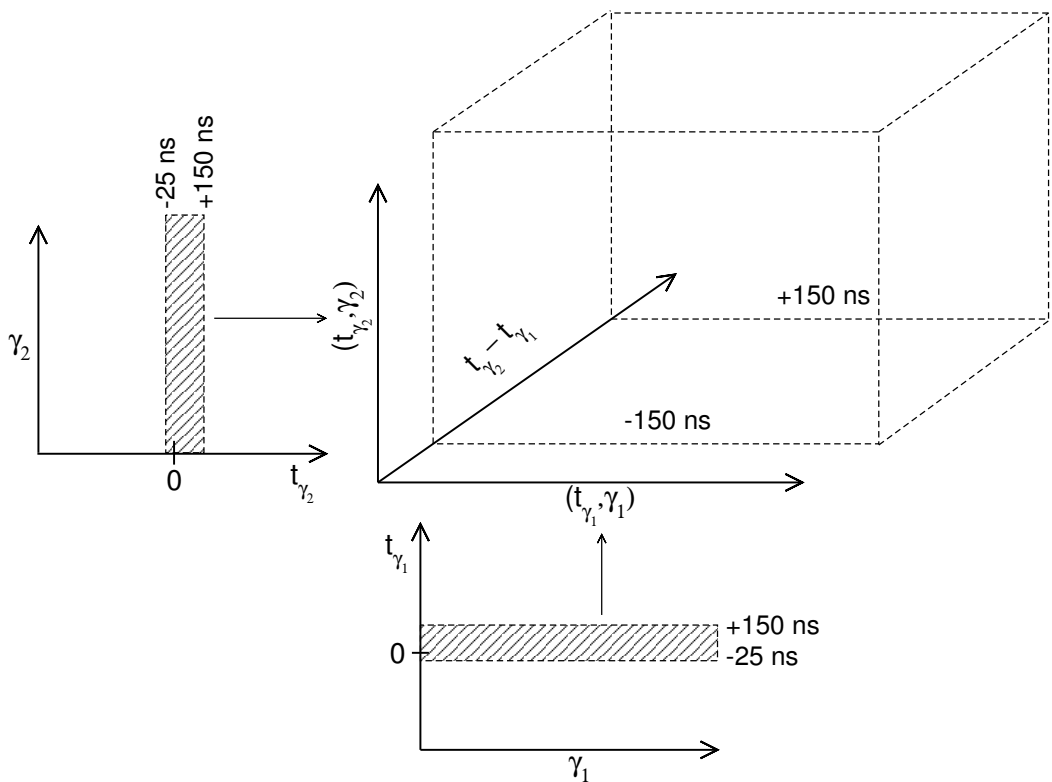


Figure 2.7: $\gamma\text{-}\gamma$ -time difference dimensional space with cuts for the construction of a $\gamma\text{-}\gamma$ prompt wide matrix. The hashed boxes and the arrows represent the prompt time slicing and projection onto the x - and y -axes of the cube. The unfilled dashed cube represents the location in the $\gamma\text{-}\gamma$ -time difference space of the prompt wide $\gamma\text{-}\gamma$ coincidences. The projection of the dashed cube on the xy plane creates the $\gamma\text{-}\gamma$ prompt wide matrix. Note that the picture is only indicative and that the vertex shown for the three dimensional $\gamma\text{-}\gamma$ -time difference space is not $(0, 0, 0)$.

2.3. OFF-LINE ANALYSIS

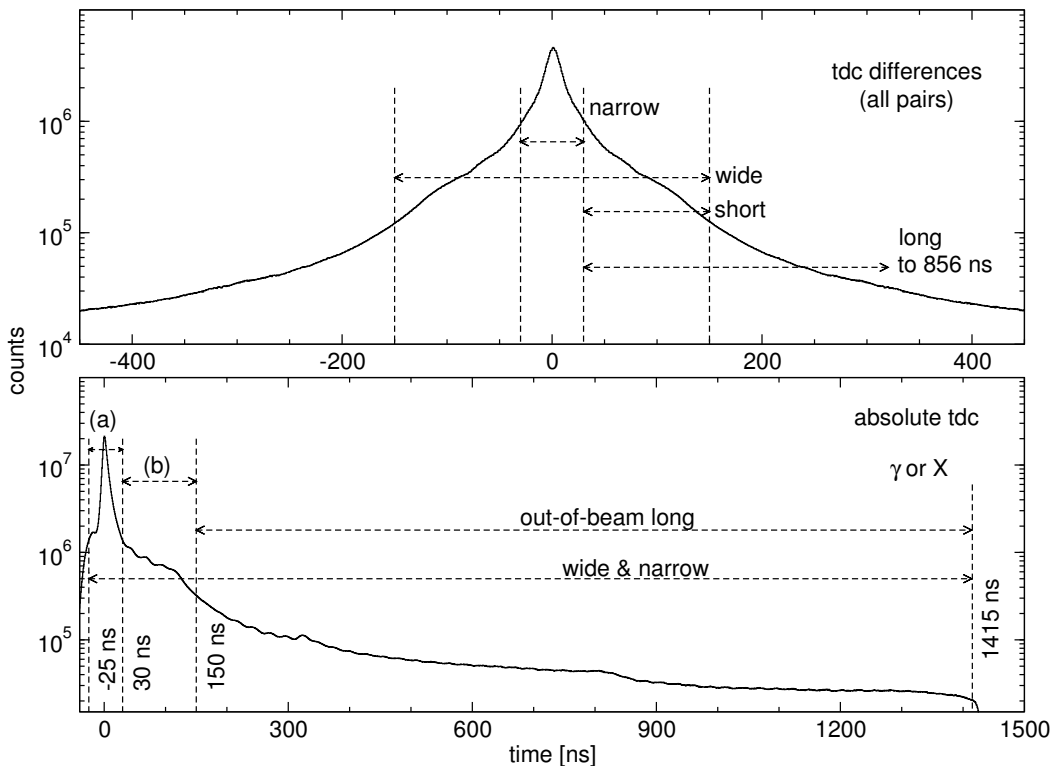


Figure 2.8: Examples of time cuts used for the sorting of $\gamma\gamma$ matrices. In the lower panel, (a) refers to the prompt narrow time cut, while (b) refers to the out-of-beam short time cuts used on the absolute time spectrum, whereas the region (a)+(b) would be the prompt wide cut (see Table 2.2).

Gating

Once the matrices have been generated, coincidence analysis is generally done in the two-dimensional space where one would usually gate on a γ -ray peak, and project the associated coincident information, usually another γ -ray energy or a γ -ray time.

2.3.3 Deconvoluting unresolved lines

Ideally a γ -ray peak in a spectrum would have a well-defined Gaussian shape. The reason why a peak might not be Gaussian is often a consequence of the detection equipment (neutron damage in the crystal of one or several detectors, for example). Furthermore, for convenience one would prefer the peaks to be well separated in order to obtain clean gates that do not contain transitions coming from another γ -ray. Unfortunately, and as will be shown in the next section (see also Appendix A), several γ -rays in ^{210}Fr overlap with transitions belonging to other nuclei.

Resolving this issue is not so straightforward as it requires already being sure that there is at least one transition that is in *unique* coincidence with each overlapping γ -ray. Consider an area where two γ -rays, ω_1 and ω_2 , are not fully resolved and cut the region into two gates \mathcal{G}_1 and \mathcal{G}_2 . The total intensity for a γ -ray, denoted γ_1 , that should be *uniquely* in coincidence with ω_1 is set to 1. Because of the overlapping γ -rays, this intensity is fractionated between the gates \mathcal{G}_1 and \mathcal{G}_2 , with the intensity fractions being α_{11} and α_{21} , respectively. Similar assumptions can be made for a γ -ray, γ_2 , that is *uniquely* in coincidence with ω_2 . This can be synthesised in the following matrix form:

$$\begin{pmatrix} \mathcal{G}_1 \\ \mathcal{G}_2 \end{pmatrix} = \begin{pmatrix} \alpha_{11} & \alpha_{12} \\ \alpha_{21} & \alpha_{22} \end{pmatrix} \cdot \begin{pmatrix} \omega_1 \\ \omega_2 \end{pmatrix}, \quad (2.7)$$

with:

$$\sum_i \alpha_{ij} = 1, \quad (2.8)$$

for each j . As a result we get:

$$\begin{pmatrix} \omega_1 \\ \omega_2 \end{pmatrix} = \begin{pmatrix} \alpha_{11} & \alpha_{12} \\ \alpha_{21} & \alpha_{22} \end{pmatrix}^{-1} \cdot \begin{pmatrix} \mathcal{G}_1 \\ \mathcal{G}_2 \end{pmatrix}, \quad (2.9)$$

which defines a way to manipulate and add the raw gates so as to recover clean coincidence gates for ω_1 and ω_2 .

2.4 Measuring internal conversion coefficients

Internal conversion is an electromagnetic phenomenon in which the energy of a transition is given to an electron (see for example Ref. [Paul 75]). As described in the introduction, measurement of α_T enables deduction of transition multipolarities. No direct conversion electron measurements were made in this work, but total conversion coefficients were deduced using intensity balances. The measurement of intensity balances is made easier when a long-lived isomer⁴ is present, although it is possible to measure total conversion coefficients in the prompt data as long as one gates on a transition above the studied γ -rays.

The absence of side-feeding following the decay of an isomer means that the intensity feeding a state is equal to the depopulating intensity. The total intensity for a transition is the sum of the γ -ray emission intensity and that for internal conversion. Because only I_γ is measured, the total conversion coefficient α_T can be measured through:

$$\sum_i I_{\gamma,i} \times (1 + \alpha_{T,i}) = \sum_j I_{\gamma,j} \times (1 + \alpha_{T,j}), \quad (2.10)$$

where i denotes the γ -rays feeding a state, and j those de-exciting it. Total conversion coefficient measurements from this work for transitions in the decay of the 178 ns isomer at 4657 keV in ^{211}Fr are presented in Table 2.3. The values agree with the result of direct measurements [Byrn 86b].

Table 2.3: Total conversion coefficients α_T for transitions in ^{211}Fr .

E_γ (keV)	$\sigma\lambda$	α_T theory ^(a)	α_T direct measurement ^(b)	α_T present work
112.9	$E2$	5.322	5.8(10)	5.9(6)
173.7	$M1$	2.984	2.9(3)	3.18(19)
233.4	$E2$	0.3228	0.27(6)	0.38(6)

^(a) Values from Ref. [Kibe 08].

^(b) Values from Ref. [Byrn 86b].

⁴An isomer is an excited state in a nucleus that has a relatively long lifetime.

2.5 Angular anisotropies for determining multi-polarities

Another method for the determination of transition multi-polarities is to measure the angular distribution of the γ -ray intensities.

2.5.1 The transition $I_i \rightarrow I_f$

Gamma-rays are not emitted isotropically from a particular excited state. Instead the probability of emission depends on the angle θ between the angular momentum \mathbf{J} and the direction of the emitted radiation. The density matrix element for a transition, $I_i \rightarrow I_f$, is written [Stef 75]:

$$\begin{aligned} \left\langle \tau \left| \rho_{q_f}^{\lambda_f}(I_f, \mathbf{p}) \right| \tau' \right\rangle &= \frac{d\Omega}{8\pi\lambda_\gamma} \sum_{\lambda_i \lambda_q q L L'} (-1)^{\lambda_i - q_i} (2\lambda + 1)^{1/2} \left(\frac{2I_i + 1}{2I_f + 1} \right)^{1/2} \\ &\quad \times \begin{pmatrix} \lambda_f & \lambda & \lambda_i \\ q_f & q & -q_i \end{pmatrix} \rho_{q_i}^{\lambda_i}(I_i) D_{q\mu}^{(\lambda)*}(\mathbf{e}_z \rightarrow \mathbf{k}) [\gamma(EL) + \tau\gamma(ML)] \\ &\quad \times [\gamma^*(EL) + \tau\gamma^*(ML)] \frac{\begin{pmatrix} L & L' & \lambda \\ \tau & -\tau' & \mu \end{pmatrix}}{\begin{pmatrix} L & L' & \lambda \\ 1 & -1 & 0 \end{pmatrix}} F_\lambda^{\lambda_f \lambda_i}(LL' I_f I_i), \end{aligned} \quad (2.11)$$

where:

- $d\Omega$ is the solid angle into which the γ -ray is *emitted*,
- the λ 's are the statistical tensor rank (see also equation just below),
- D -matrices are needed to transform angular momentum states (such as I_i and I_f) under a rotation of the quantisation axes. They allow for the expression of the density matrix element in the direction of propagation of the wave at which the radiation intensity is measured to determine the angular distribution. The original D -matrices can be changed so as to be in the direction of propagation of the wave by expanding with respect to a new angular momentum basis, i.e. the q 's (expression of the m quantum

2.5. ANGULAR ANISOTROPIES FOR DETERMINING MULTI-POLARITIES

number in the new space); this allows for the change in space:

$$D_{m_1 \bar{m}_1}^{(j_1)}(\alpha \beta \kappa) D_{m_2 \bar{m}_2}^{(j_2)}(\alpha \beta \kappa) = \sum_q (2q+1) \begin{pmatrix} j_1 & j_2 & \lambda \\ m_1 & m_2 & q \end{pmatrix} \begin{pmatrix} j_1 & j_2 & \lambda \\ \bar{m}_1 & \bar{m}_2 & \bar{q} \end{pmatrix} \times D_{q\bar{q}}^{(\lambda)*}(\alpha \beta \kappa), \quad (2.12)$$

- the $\begin{pmatrix} 1 & 2 & 3 \\ 4 & 5 & 6 \end{pmatrix}$ coefficients are the Wigner-6j function. These are tabulated in Ref. [Appe 68],
- E and M (respectively electric and magnetic) denotes the type of the electromagnetic radiation,
- L is the maximum angular momentum carried away by the photon,
- $\gamma(\pi L) = \gamma(\pi L, I_i \rightarrow I_f)$ is the amplitude of the radiation (probability),
- τ is the helicity of the γ -ray photon,
- the F_k 's are coefficients that are tabulated in Ref. [Mate 74].

From Eq. 2.11 the angular distribution as a function of the direction of propagation \mathbf{k} is obtained by:

$$W(\mathbf{k}) = \sum_{\tau\tau'\lambda_f q_f} \left\langle \tau \left| \rho_{q_f}^{\lambda_f}(I_f, \mathbf{p}) \right| \tau' \right\rangle \times (2I_f + 1)^{1/2} \quad (2.13)$$

2.5.2 Angular distribution for an aligned ensemble of nuclei

In a heavy-ion reaction the angular momenta of an ensemble of nuclei produced in the reaction are aligned in a plane perpendicular to the beam (z) axis. This reduces the complexity of Eq. 2.11, mainly through simplification of the D -matrices into spherical harmonics which then give rise to Legendre polynomials. The equation for the angular distribution of γ -rays emitted from an oriented source is therefore:

$$W(\theta) = \sum_{\lambda} A_{\lambda} P_{\lambda}(\cos \theta). \quad (2.14)$$

CHAPTER 2. EXPERIMENTAL METHODS

The P_k are the Legendre polynomials and it is usual to normalise the distribution so that $A_0 = 1$. The coefficients A_k are defined by [Stef 75]:

$$A_\lambda = \alpha_\lambda \frac{1}{1 + \delta_{12}^2} [B_\lambda(J_i)F_\lambda(L_1 L_1 J_f J_i) + 2\delta_{12}(\gamma_{12})B_\lambda(J_i)F_\lambda(L_1 L_2 J_f J_i) + \delta_{12}^2(\gamma_{12})B_\lambda(J_i)F_\lambda(L_2 L_2 J_f J_i)], \quad (2.15)$$

where α_λ is the attenuation coefficient, the coefficient B_λ is the radiation orientation coefficient defined in Ref. [Stef 75], and finally δ_{12} is the mixing ratio:

$$\delta_{12} = \frac{\gamma_1}{\gamma_2}, \quad (2.16)$$

where γ_i is understood as the amplitude of the γ -ray with a particular multipolarity $X\lambda$.

The CAESAR array contains six detectors in the vertical plane defining a set of three angles with regard to the beam axis and therefore allows for the measurement of A_2 . The coefficients F_k in Eq. 2.15 are the same as those in Eq. 2.11. The coefficients B_k contain the remaining information of the statistical tensor, and depend on the experimental likelihood to measure a particular m -substate (J_z) around 0, i.e. perpendicular to the beam axis (see Figure 2.10). This is usually called the degree of alignment and can be characterised by the spread (σ) in the m -substate distribution as σ/J (“sigma over J”).

The A_2 coefficient for stretched transitions can be obtained by computing Eq. 2.14. Results are given in Table 2.4.

For $\sigma/J = 0.3$, the value A_2 as a function of the mixing ratio ($\delta = \gamma(E2)/\gamma(M1)$) is shown in Figure 2.9 for mixed quadrupole/dipole transitions with $J = 13$ and $J = 20$.⁵ It can be seen that a stretched $M1$ ($\gamma(E2) = 0$) has a A_2 value of -0.21 .

Table 2.4: A_2 coefficient for stretched transitions and $\sigma/J = 0.3$.

Type	L	A_2
Dipole	1	-0.21
Quadrupole	2	0.28
Octupole	3	0.46

⁵Using tabulated values for F_2 and B_2 from Ref. [Mate 74] for $\sigma/J = 0.3$.

2.5. ANGULAR ANISOTROPIES FOR DETERMINING MULTI-POLARITIES

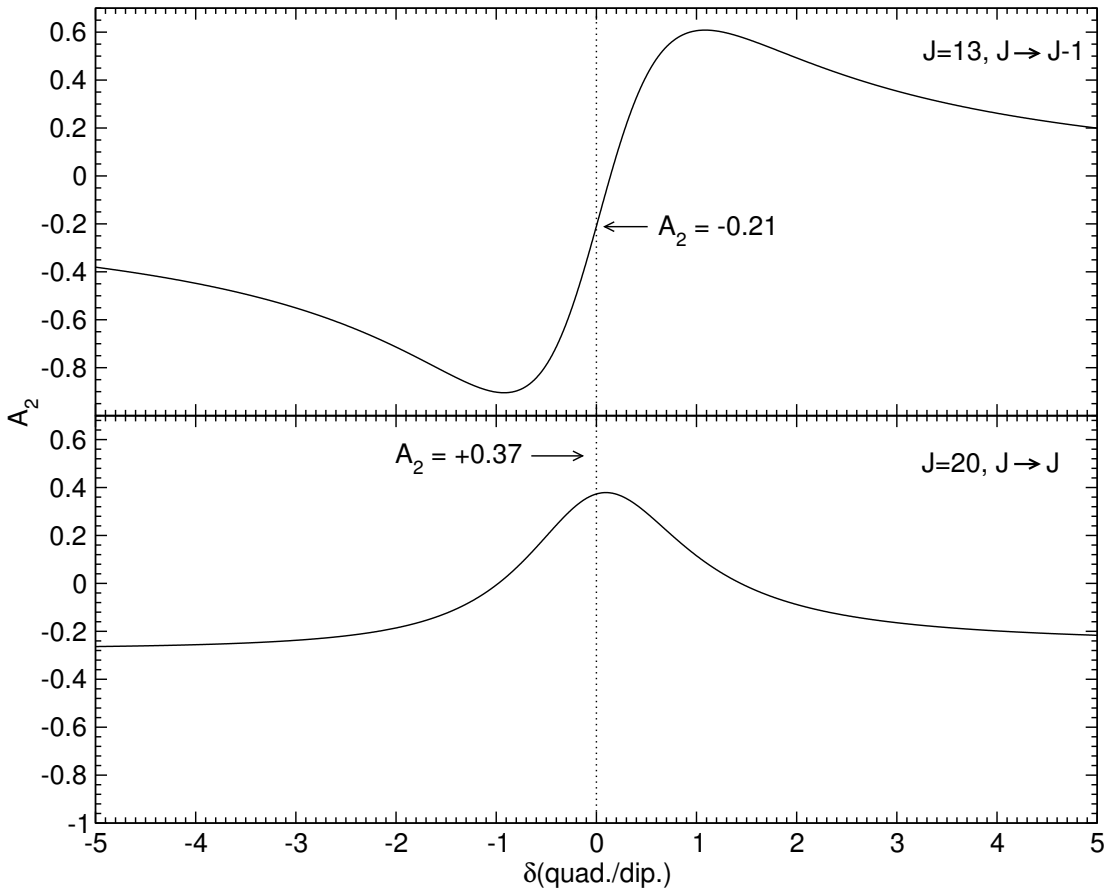


Figure 2.9: Values of the A_2 coefficient for quadrupole/dipole $J \rightarrow J$ and $J \rightarrow J - 1$ transitions as a function of the mixing ratio δ .

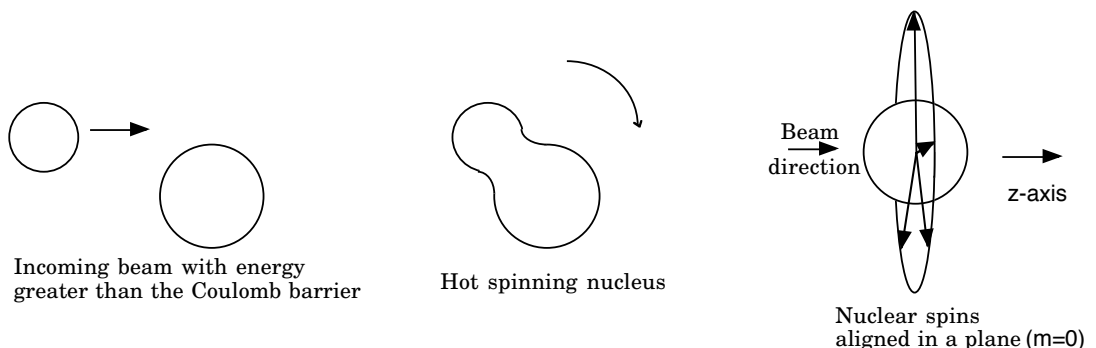


Figure 2.10: Alignment of the nuclear spins in the plane perpendicular to the beam following a heavy-ion reaction. This figure is adapted from Figure 3.1 in Ref. [Lane 95].

2.5.3 Correlations in gated angular distributions

The angular distribution should be measured in singles. It is, however, often more practical to measure angular distributions in gated spectra where contamination is eliminated. Possible correlation effects must then be considered. As shown in Fig. 2.11, since the statistical tensor for the state J_1 depends on the direction of propagation of g_1 , and hence its angular distribution, the statistical tensor for the state with J_2 also depend on it and not only on k_2 . If there are enough detectors in the array (e.g. covering close to the full 4π sphere) so that the angular intensity can be measured at enough angles, then the correlation effects average out. This is the case at Gammasphere for instance [Lane 98]. The CAESAR array, however, only covers three angles and is not symmetric. Gated angular distributions will, therefore, slightly differ, if one gates on dipole or quadrupole transitions for example but not to the level where multi-polarity assignments could be perturbed.

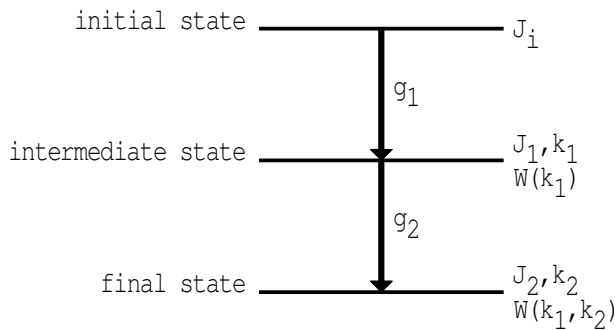


Figure 2.11: Cascade of γ -rays decaying from an initial aligned state.

2.6 Techniques for lifetime measurements

Information regarding the lifetime of an excited state is important for the description of the structure of a nucleus as it often provides key arguments for the assignment of a particular configuration to, not only the isomeric state in question, but also states populated in the direct and intermediate decay. (In this work the lifetime is always used to describe the meanlife of the state, not the half-life.)

In order to measure isomer lifetimes, several techniques can be used based on direct electronic measurement of γ -ray times with respect to either the beam or to other γ -ray times. For example, measuring the absolute time of arrival of γ -rays with respect to the beam pulse yields better results when the γ -ray studied is in a region of low contamination, but only if one lifetime is involved. Otherwise the

Table 2.5: Measurement of angular distribution for transitions in ^{211}Fr and ^{206}Po .

Nucleus	E_γ (keV)	$\sigma\lambda$	Source	A_2 (<i>a</i>)	A_4 (<i>a</i>)	A_2/A_0 singles(<i>b</i>)	A_2/A_0 gated(<i>b</i>)
^{206}Po	395.5	$E2$	activity		+0.03(3)		
	477.0	$E2$	activity		+0.07(6)		
^{211}Fr	173.7	$E2$	in-beam	-0.16(1)	0.04(2)	-0.23(5)	
	233.4	$E2$	in-beam	+0.12(6)	-0.00(1)	+0.163(7)	
	264.0	$M1/E2$	in-beam	-0.43(8)	-0.02(4)	-0.30(3)	
	327.3	$M1$	in-beam	-0.23(2)	0.02(3)	-0.28(4)	-0.26(7)
	357.6	$E2$	in-beam	+0.17(2)	-0.08(3)	+0.23(6)	
	450.2	$E1$	in-beam	-0.11(1)	0.00(2)	-0.12(3)	
	652.6	$E2$	out-of-beam			+0.01(3)	
	800.3	$E2$	in-beam	+0.14(6)	-0.02(8)	+0.15(3)	+0.16(4)
	800.3	$E2$	out-of-beam			+0.01(3)	
	820.9	$E2$	in-beam	+0.20(2)	-0.02(3)	+0.20(4)	

(*a*) Values from Ref. [Byrn 86b], the measurements included A_4 and were done in singles.

(*b*) Assuming $A_4=0$.

γ - γ -time difference matrices can be used with gates above and below the isomer. These technique can provide measurements down to 0.5 ns when used with the centroid shift method (see below and Refs. [Bay 50, Lobn 75, Stod 91]). For lifetimes greater than a few hundred nanoseconds, evaluation of the time dependence of γ -ray intensities in the out-of-beam region can generally yield better results. Figure 2.12 presents the measurement of the lifetime of the isomer at 4657 keV in ^{211}Fr and confirms the results obtained by Byrne *et al.* [Byrn 86b] while narrowing the uncertainty. Contamination by coincidences with γ -rays from long-lived decay activities is eliminated by subtracting events late in the time interval, that is, after the isomer has decayed, see Figures 2.13 and 2.14.

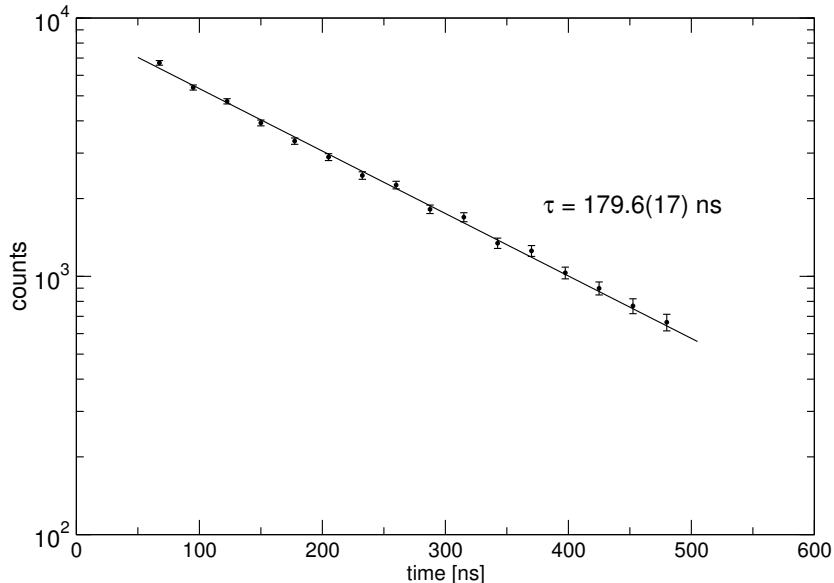


Figure 2.12: Measurement of the lifetime of the isomeric state at 4657 keV in ^{211}Fr obtained by adding the intensities of several transition together. The measured lifetime by Byrne *et al.* [Byrn 86b] was 178(20) ns.

Centroid Shift Method

A time spectrum, $F(t)$, is the convolution of the prompt response (noted $pr(t)$ and dependent on the detector and electronics) and the nuclear decay curve $f(t)$ that would be a simple exponential in the case of a single lifetime. It can be written as:

$$F(t) = \int_0^{+\infty} f(t') pr(t - t') dt' \quad (2.17)$$

2.6. TECHNIQUES FOR LIFETIME MEASUREMENTS

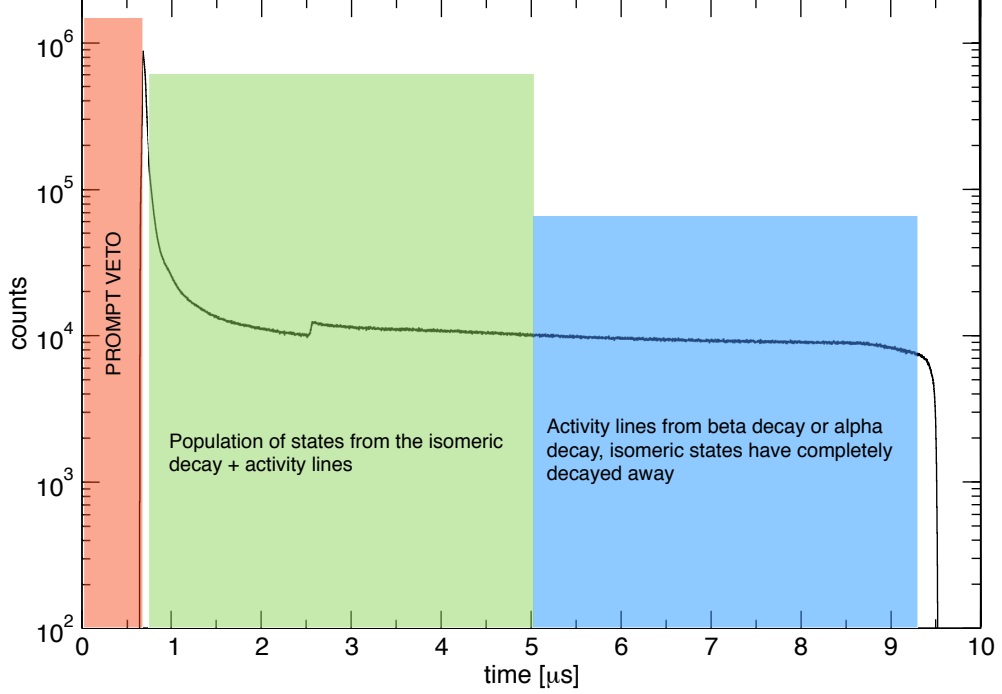


Figure 2.13: Total TAC spectrum for all γ -rays together with the definitions of the time regions. Note that the time axis has been reversed for this figure. The step in the middle of the green section reflects the time required for the electronics to recover from the high intensity that occurs during the in-beam period, note that it occurs after $1.8 \mu\text{s}$.

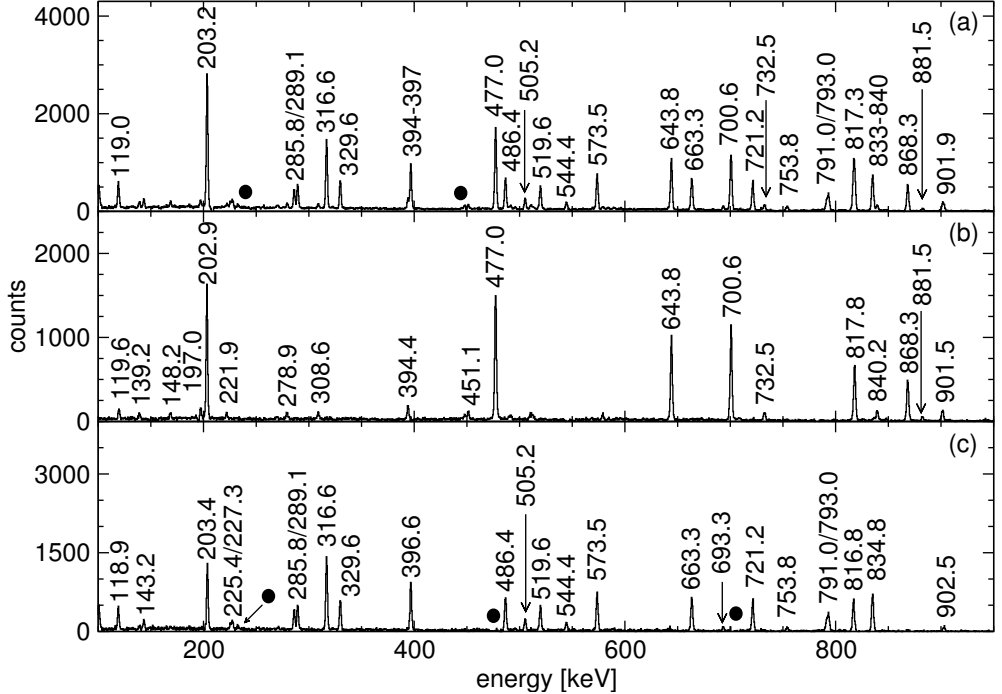


Figure 2.14: Gate on the 257 keV line from (a) 0.8 to 5 μs and (b) 5 to 9.2 μs . (c) Normalised difference between (a) and (b). Filled circles denote subtraction artefacts.

Bay [Bay 50] showed that, since the moment of a function is:

$$M^{(n)}[f(x)] = \int_{-\infty}^{+\infty} x^n f(x) dx \quad (2.18)$$

then the lifetime τ is given by the difference between the first moments of the prompt curve and the delayed curve. The first moment of a function being its mean value, the centroid shift method states that if a shift s is observed between a prompt time curve and any time curve then $s = \tau$. This is only practical for short τ and when direct fitting of the slope of the exponential decay curve is not precise enough. By fitting the whole curve both the moment and the lifetime are included.

To determine the shift s , the prompt response of the detector must be known. It is energy dependent and can be determined by looking at transitions nearby in energy that are known to be prompt. If the time- γ - γ spectrum is shifted from the prompt position by an amount “ s ”, then either one of the states in between the two γ -rays has a lifetime $\tau = s$, or it could mean that several states in between the γ -rays have a lifetime and $\sum_i \tau_i = s$.

The centroid shift method can be applied to measure very short lifetimes. The statistical time limitation of the method is the statistical uncertainty for a Gaussian function (σ/N_0) and therefore only depends on the width of the signal output of the HPGe which is of the order of $\sigma = 10$ ns. The uncertainty of the method due to the statistical nature of the spectra used, is negligible for any decent time spectrum ($N_0 = 10^3$ and $\sigma = 10$ ns gives a statistical uncertainty of 0.01 ns). The propagation of the uncertainty in the decay curve fits can, however, yield large uncertainties in the measurement of the lifetime.

Ideal time responses are symmetric Gaussian functions. However the prompt response varies as a function of energy, and even prompt time-differences have asymmetric Gaussian shapes (see Figure 2.15). Hence the energy dependence of the prompt time response can be indirectly taken into account by fitting those responses with asymmetric instead of symmetric Gaussians. This is shown in Figure 2.16, which presents the measurement of the lifetime of the isomeric state at 1686 keV in ^{211}Fr . The points in the fit are reported in Table 2.6. The lifetime is obtained through the difference between weighted averages of the prompt blue points and the red points that exhibit a lifetime using the equation:

$$\tau = \left| \frac{\sum_i (pr_i - dr_i)/\varepsilon_i^2}{\sum_i 1/\varepsilon_i^2} \right|, \quad (2.19)$$

2.6. TECHNIQUES FOR LIFETIME MEASUREMENTS

where pr means (prompt) time zero position, dr (delay) time zero position and ε uncertainty on the time zero position (prompt or delay).

Table 2.6: Centroid position for various combinations of time- γ - γ projections (time difference spectra). Several transitions in the same energy region are used, regardless of which nucleus they belong to, to determine the prompt time-zero position. The other points, giving the lifetime of the isomer, are, however, determined by using γ -rays of similar energies. For example, in ^{211}Fr two γ -rays are in the 800 keV region (800 and 821 keV), but they cannot be used together because they have several isomers between them, so that only the 800 keV γ -ray is used to obtain the time-zero curve.

E_{γ_1} (keV)	E_{γ_2} (keV)	ΔT (centroid position in ns)	Prompt (P) or lifetime (L)
800	174	1.63(26)	L
800	233	-0.37(10)	P
800	450	3.07(10)	L
800	563	3.14(36)	L
800	653	-0.01(8)	P
793	204	0.60(42)	P
793	257	-0.62(22)	P
793	289	-0.09(17)	P
793	520	-0.37(15)	P

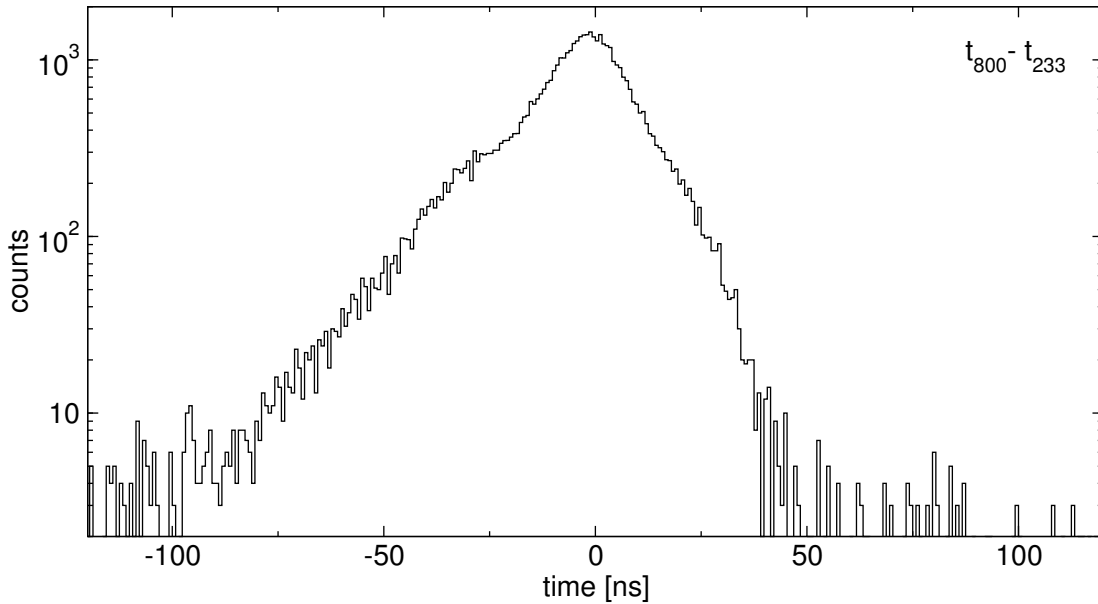


Figure 2.15: Time difference between the 800 and 233 keV γ -rays in ^{211}Fr . With no intervening lifetime this should be symmetric, however, because the time response for a lower energy γ -ray is longer than for a higher energy one (walk), the main part of the spectrum is in the negative time.

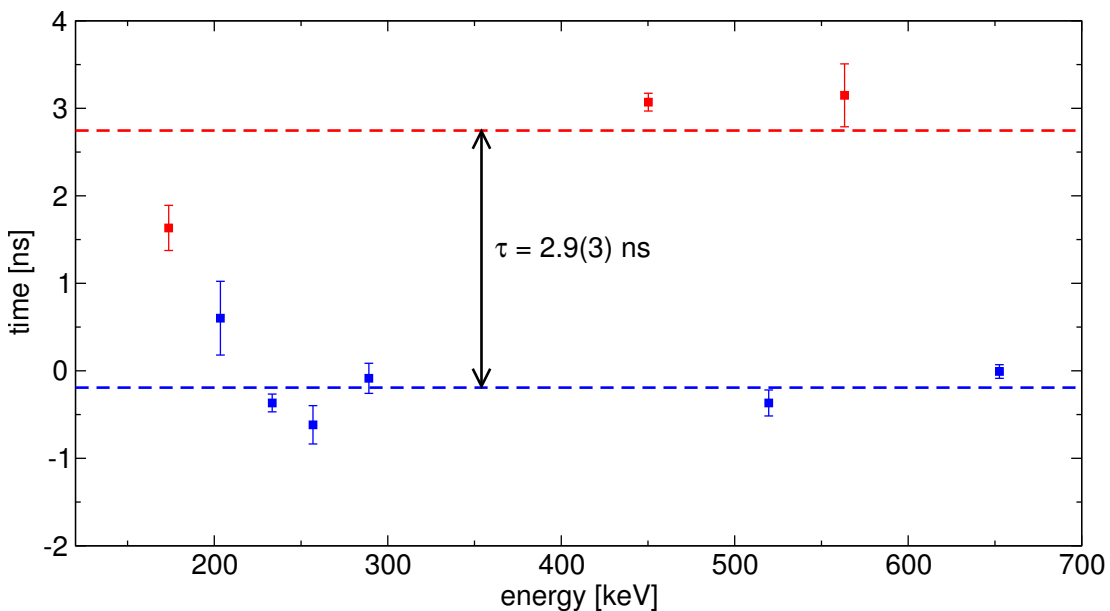


Figure 2.16: Centroid position for time- $\gamma\gamma$ with both gates below an isomer (blue) or across the isomer at 1686 keV in ^{211}Fr (red). A lifetime $\tau = 2.9(3)$ ns is deduced. The method used for the determination of the red and blue points of this figure is shown in Table 2.6.

Chapter 3

Experimental results

“La tour Eiffel entièrement faite avec des allumettes. 346422 exactement.”

– Jacques Villeret (as François Pignon), in Le dîner de cons.

This chapter presents results from the experimental measurements conducted as a part of this work. The determination of the level scheme for ^{210}Fr through the use of γ - γ -time coincidence techniques is discussed in Sections 3.1 & 3.2. Lifetime measurements are presented in Section 3.3 and are followed by a discussion of spin and parity assignments and the deduced transition strengths (Section 3.4).

Preliminary considerations

Although the study of the α -decay of ^{214}Ac into ^{210}Fr by Kuusiniemi *et al.* [Kuus 04] had identified several states at low spin, the level scheme for ^{210}Fr had not been investigated at high spin before the start of this work and the level scheme was constructed with no initial assumptions. States up to around 5 MeV and $J \sim 26\hbar$ were identified, including four isomeric states. None of the isomers, however, could be used for the isolation of separate cascades of γ -rays that could be simply placed in the level scheme since the lifetimes are either too short or are in weakly populated branches. Furthermore, the level scheme has many parallel cascades and is highly fragmented. The presentation of the level scheme is consequently split into two phases. First, the level scheme from the decay of a high-spin, long-lived isomer (the subject of a short report [Marg 12]) is discussed, and this is used to introduce the more complex complete level scheme deduced from the study of the in-beam γ - γ -time coincidences. Details of the two major experiments are presented in Table 3.1. Note that this exposition of the level scheme is opposite to the order in which the experiments were performed.

In the first experiment with 1/1712 ns pulsing the presence of a long-lived high-spin isomer in the level scheme was deduced. A second experiment con-

centrating on out-of-beam coincidences, measured with $1/9\ \mu\text{s}$ beam chopping, was performed to improve upon the isomer measurement. Since only transitions populated in the decay of the long-lived isomeric state are observed, construction of the scheme is naturally simplified.

Table 3.1: Measurements for ^{210}Fr .

Measurements	Reaction	Beam timing	Energy (MeV)
Singles	$^{197}\text{Au}(^{17}\text{O},4\text{n})^{210}\text{Fr}$		85, 90
excitation function	$^{197}\text{Au}(^{18}\text{O},5\text{n})^{210}\text{Fr}$		88 ¹ , 97, 102
γ - γ -time	$^{197}\text{Au}(^{18}\text{O},5\text{n})^{210}\text{Fr}$	pulsed 1/1712 ns	97
beam- γ			
γ - γ -time	$^{197}\text{Au}(^{18}\text{O},5\text{n})^{210}\text{Fr}$	chopped 1/9 μs	97
beam- γ			

¹ Prior measurement [Drac 09a].

3.1 Decay of the high-spin, long-lived isomer

The study presented in this section used the time-gated subtraction techniques outlined in Section 2.6 to suppress the unwanted long-lived activities. All of the transitions depopulating states fed by the decay of the isomer can be seen in the out-of-beam coincidence spectrum for the 256.9 keV transition (Figure 3.2). The level scheme for the decay of this isomer is presented in Figure 3.1. Properties of the transitions are given in Table 3.2.

Placement of transitions in the level scheme also benefits from the presence of a short lived isomer at 2206 keV. While the lifetime of the state is not long enough to allow early-delayed gating, inspection of the time differences between γ -rays assigned to ^{210}Fr provides an ordering of those transitions with regards to the position of the isomer. This will be discussed in more detail in Section 3.3.

The coincidence spectra presented in this section are background subtracted, and contamination from long-lived activities has also been subtracted. However some artefacts cannot be suppressed. For example the very high intensity of the 477.0 keV γ -ray populated in the β -decay of ^{206}At (the α -decay product of ^{210}Fr) into ^{206}Po means that a slight (statistical) shift of the peak energy between the two time regions can generate single channel “spikes” left over from subtraction. Such artefacts have been labelled with filled circles in the various γ -ray spectra figures presented in this chapter.

3.1. DECAY OF THE HIGH-SPIN, LONG-LIVED ISOMER

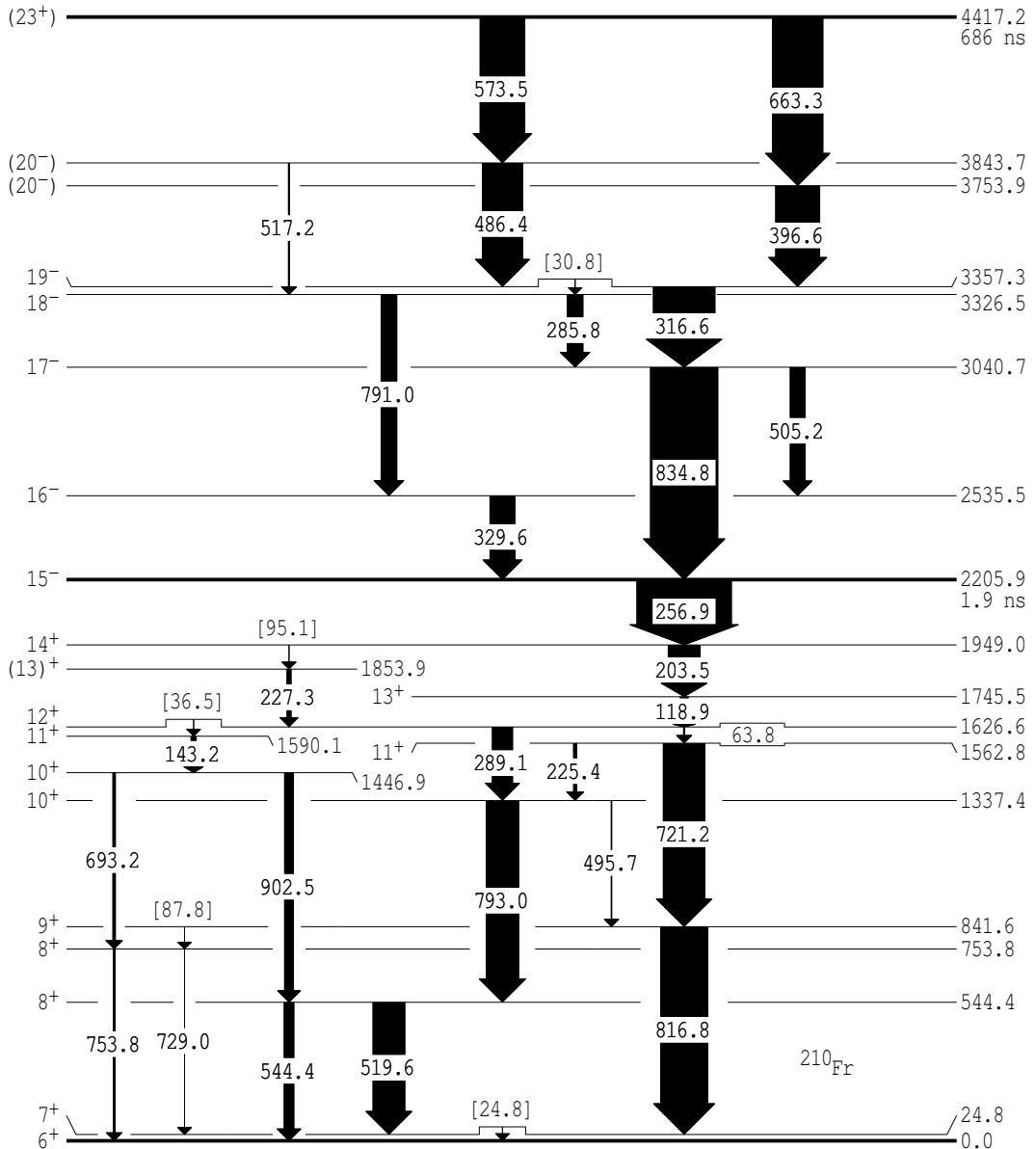


Figure 3.1: Partial level scheme for ^{210}Fr showing the decay of the isomer at 4417 keV. The widths of the transitions indicate the out-of-beam γ -ray intensities. Transition energies in brackets are inferred from coincidences – the γ -rays have not been observed directly.

CHAPTER 3. EXPERIMENTAL RESULTS

Table 3.2: Properties of transitions assigned to the decay of the high-spin, long-lived isomer in ^{210}Fr . Transitions in italics with no γ -ray intensity given have been inferred from coincidence relationships and were not observed directly.

E_γ	I_γ	E_i	E_f
24.8		25	0
30.8		3358	3327
36.5		1627	1447
63.8	21(4)	1627	1563
87.8		842	754
95.1		1949	1854
118.9	95(6)	1746	1627
143.2	63(3)	1590	1447
203.5	343(11)	1949	1746
225.4	42(5)	1563	1337
227.3	52(6)	1854	1627
256.9	1000(26)	2206	1949
285.8	172(5)	3327	3041
289.1	221(6)	1627	1337
316.6	655(17)	3358	3041
329.6	272(8)	2536	2206
396.6	471(18)	3754	3358
486.4	431(15)	3844	3358
495.7	14(3)	1337	842
505.2	166(5)	3041	2536
517.2	21(6)	3844	3327
519.6	343(10)	544	25
544.4	111(9)	544	0
573.5	478(13)	4418	3754
663.3	537(15)	4418	3754
693.2	35(6)	1447	754
721.2	446(13)	1563	842
729.1	7(3)	754	25
753.8	28(4)	754	0
791.0	174(8)	3327	2536
793.0	349(10)	1337	544
816.8	503(13)	842	25
834.8	715(20)	3041	2206
902.5	102(11)	1447	544

3.1. DECAY OF THE HIGH-SPIN, LONG-LIVED ISOMER

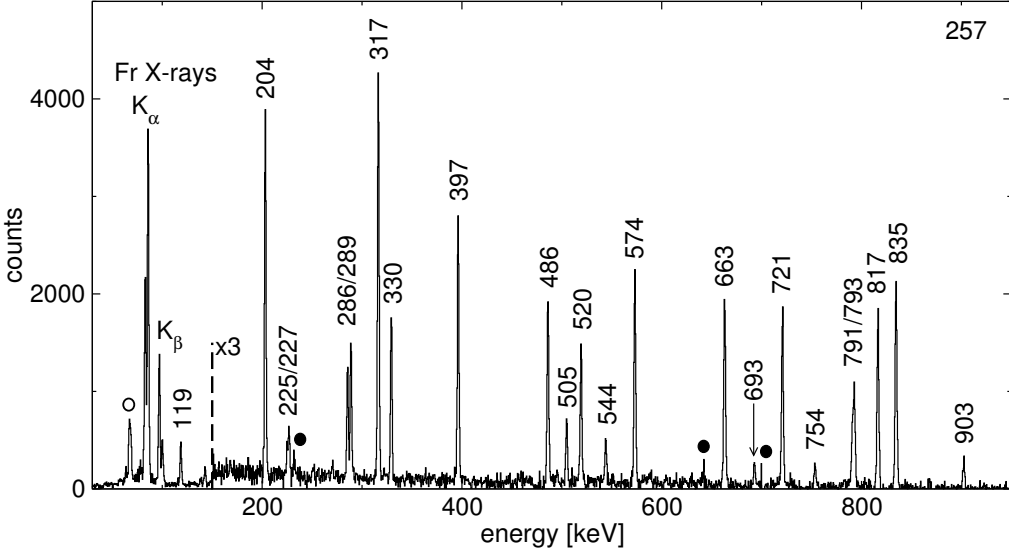


Figure 3.2: Out of beam γ -ray coincidences for the 256.9 keV transition. The open circle denotes known contaminants (in this case Au X-rays). Long-lived activities have been subtracted and the filled circles denote subtraction artefacts. (Note that filled circles will consistently be used for this purpose in the following.) The 573.5 and 663.3 keV γ -rays that are observed here are absent in the equivalent in-beam spectrum.

3.1.1 States and transitions below the isomer at 2206 keV.

The fragmented nature of the level scheme means that a conventional “bottom-up” approach for the description of the level scheme construction, starting with the most intense transitions, would not be the clearest method of presentation. Although the construction of the level scheme was actually tackled in reality in a different order, it is appropriate to start this discussion with the 519.6 and 544.4 keV transitions.

The spectra with out-of beam gates on the 519.6 (see Figure 3.3) and 544.4 keV γ -rays are identical, supporting their placement in parallel. These spectra select out five transitions at 143.2, 225.4, 289.1, 793.0 and 902.5 keV. Furthermore the strong 721.2 and 816.8 keV peaks that are observed in Figure 3.2, as well as the weaker 693.2 and 753.8 keV, are absent. The latter two γ -rays are, however, observed in the out-of-beam gate on the 143.2 keV transition together with the 902.5 keV while all of the others are absent. Note that the 753.8 keV was also observed to feed the ^{210}Fr ground state in the ^{214}Ac α -decay study by Kuusiniemi *et al.* [Kuus 04]. Taken together with the fact that the energy sum of the 902.5 and 544.4 keV γ -rays matches that of the 693.2 and 753.8 keV transitions and that a gate on the 902.5 keV γ -ray does not see either the 693.2 or 753.8 keV

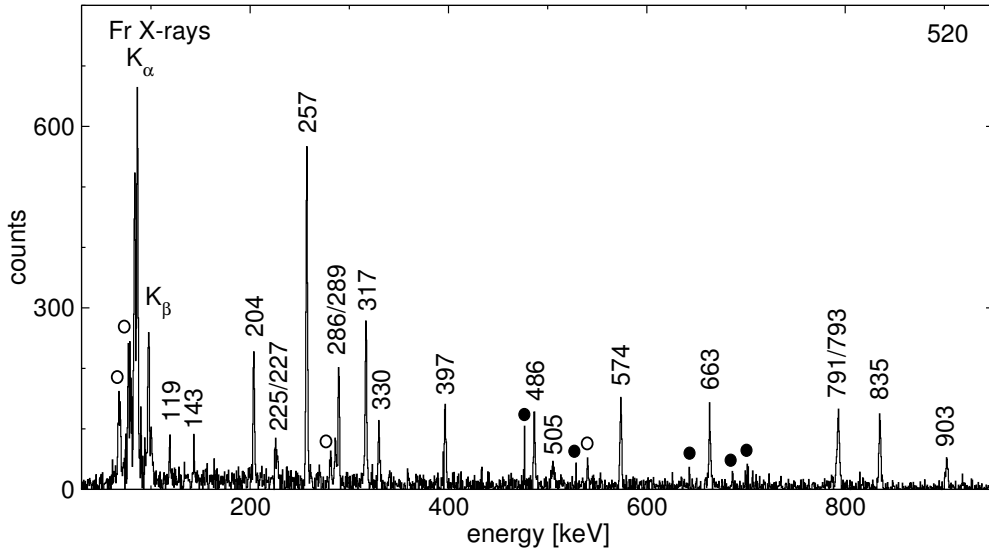


Figure 3.3: Out of beam γ -ray coincidences for the 519.6 keV transition. The open circles denote contaminants (Au X-rays and an unidentified nucleus). Long-lived activities have been subtracted. The 544.4 keV γ -ray is absent here, as are the 721.2 and 816.8 keV transitions.

transitions, this confirms that the 693.2/753.8 and 544.4/902.5 keV paths are parallel to each other and both feed the ground state.

The out-of-beam coincidence spectrum for the 289.1 keV line (see Figure 3.4) shows the 793.0 keV transition, however the 902.5 and 721.2 keV γ -rays are not apparent. A low intensity line at 816.8 keV is observed which is evidence for a 495.7 keV transition linking the two different paths. Hints of such a transition were found in the gate on the 256.9 keV transition. This is critical for the level scheme since it seals the placement of unseen transitions such as those at 24.8 and 87.8 keV. The out-of-beam coincidence spectrum for 816.8 keV (see Figure 3.5) also shows the 63.8 keV transition, which is placed above the 721.2 keV transition. This is also deduced from the coincidence spectra for the 225.4 and 289.1 keV γ -rays which are essentially the same as the parallel 519.6 and 544.4 keV coincidence spectra. Furthermore, a gated spectrum on the 63.8 keV line observed in the LEPS detectors shows the 225.4, 721.2, 793.0 and 816.8 keV γ -rays amongst others (see Figure 3.6).

Finally, the out-of-beam spectra with gates on the 118.9 and 203.5 keV lines are almost identical to that on the 256.9 keV γ -ray, with the exception of a 227.3 keV transition. It was also observed in coincidence with all transitions below the 1627 keV state. This suggests two other unseen transitions: a 36.5 keV transition to fill the gap above the 143.2 keV transition and a 95.3 keV γ -ray transition above the 227.3 keV transition, connecting the 1949 and 1854 keV states.

3.1. DECAY OF THE HIGH-SPIN, LONG-LIVED ISOMER

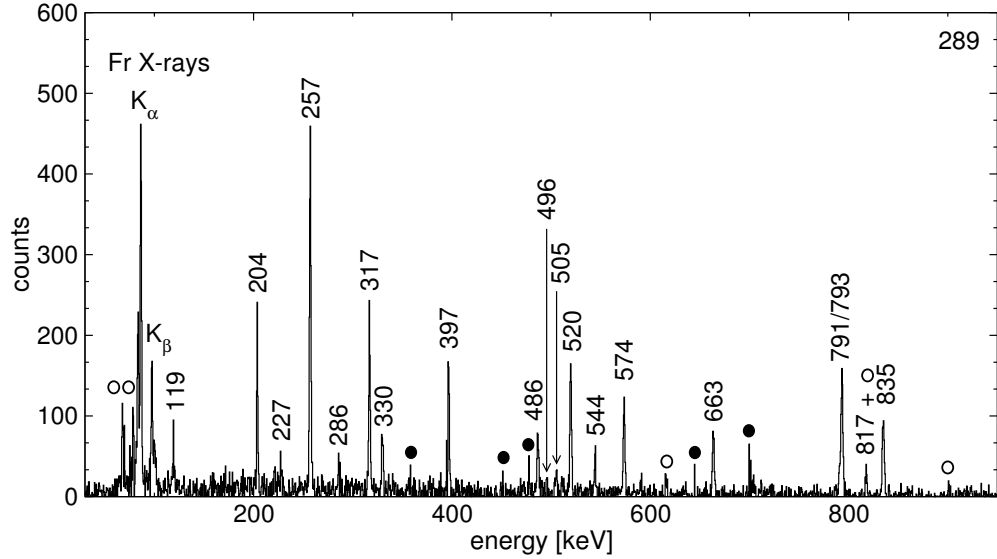


Figure 3.4: Out of beam γ -ray coincidences for the 289.1 keV transition. The open circles denote known contaminants (Au X-rays plus contamination from a close-lying transition in ^{210}Rn that could not be deconvoluted due to poor statistics). The 721.2 keV transition is absent here, however the 816.8 keV and 495.7 keV γ -rays can be observed.

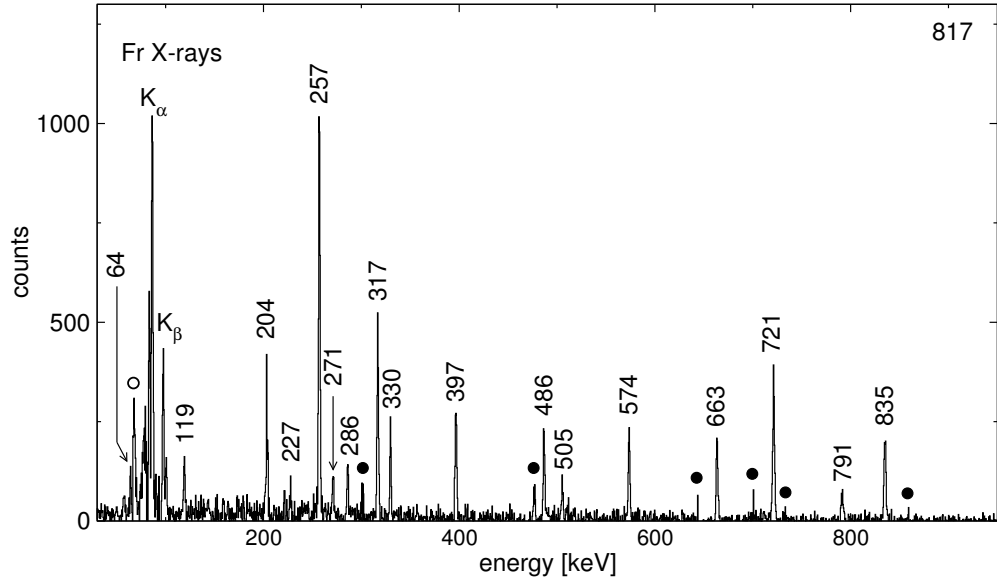


Figure 3.5: Out of beam γ -ray coincidences for the 816.8 keV transition, obtained using the deconvolution methods for unresolved γ -rays (see Section 2.3.3 and Appendix A). The 271.0 keV transition appears in another branch of the level scheme (see Figure 3.9 and Section 3.2.3 below) and decays via a $\tau \sim 30$ ns isomer.

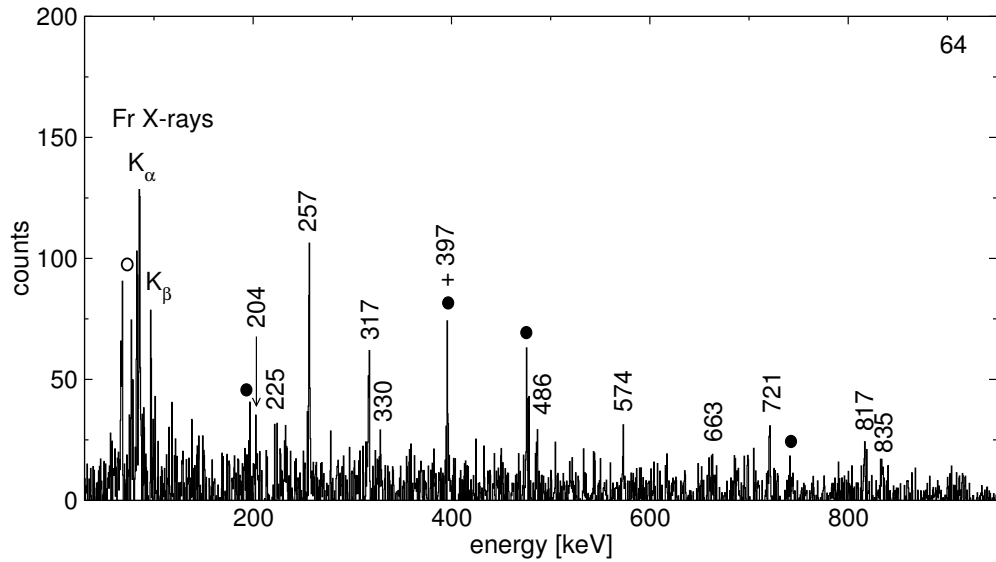


Figure 3.6: Out of beam HPGe coincidences for the 63.8 keV transition observed in the LEPS detectors.

3.1.2 States and transitions above the isomer at 2206 keV

The out-of-beam spectrum for the 256.9 keV line shown in Figure 3.2 contains ten transitions that are placed above the state at 2206 keV. The out-of-beam coincidence spectrum for the 834.8 keV transition (see Figure 3.7) is missing three of these at 329.6, 505.2 and 791.0 keV. The sum of the first two matches 834.8 keV so that they are placed in parallel to this γ -ray. The 791.0 keV transition is also absent in the out-of-beam coincidence spectrum for the 316.6 keV line but is clearly present in that for the 329.6 keV transition (see Figure 3.7). The 285.8 and 505.2 keV γ -ray cascade matches the 791.0 keV gap. Because all these transitions are present in the out-of-beam coincidence spectra for the 396.6 and 486.4 keV lines, a 30.8 keV transition is inferred between the 3357 and the 3327 keV states. The lower intensity ratio for the 316.6 and 329.6 keV transitions in the out-of-beam gate on the 573.5 keV line, compared to that on the 663.3 keV transition (see Figure 3.8), provides further evidence for this placement. All transitions, including the 316.6 keV γ -ray, have the same relative intensities in both spectra, except the 329.6 keV peak that has an excess of around seventy counts in the 573.5 keV spectrum. This excess cannot be explained by the uncertainty in the fitting. A 517.2 keV transition is thus tentatively placed between the 3844 and 3327 keV states. If this assumption is correct, a 517.2 keV peak in the 573.5 keV gate should have \sim 45 counts. Hints of such a transition are seen and are further corroborated by the slight shift of the 791.0/793.0 keV doublet towards 791.0 keV in the spectrum for the 573.5 keV gate (see Figure 3.8).

3.1. DECAY OF THE HIGH-SPIN, LONG-LIVED ISOMER

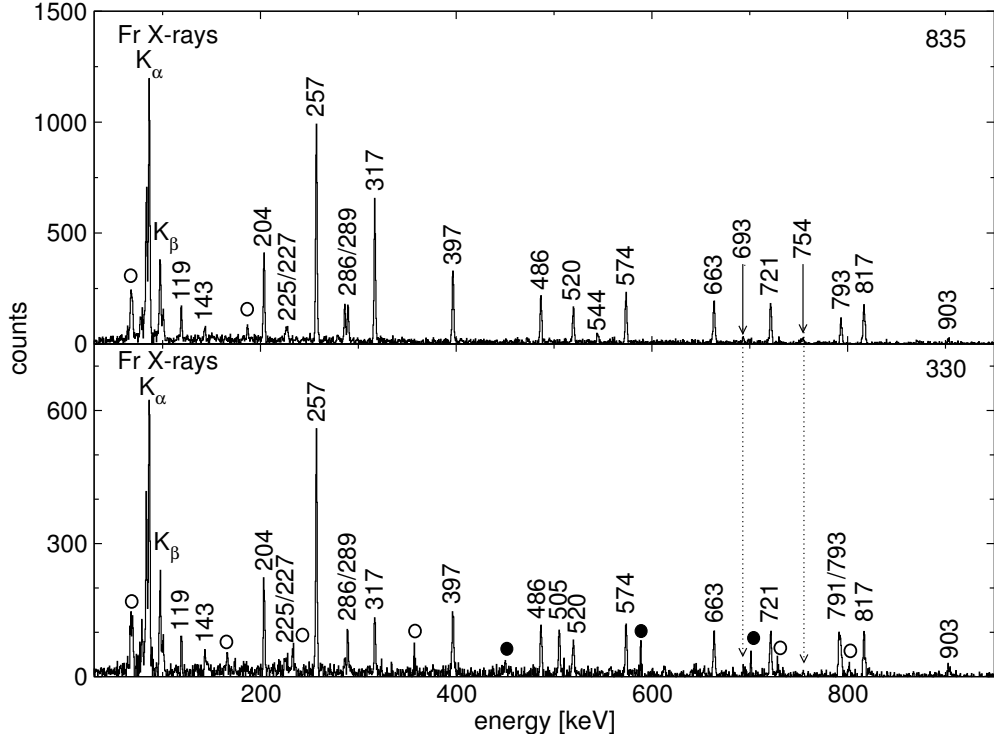


Figure 3.7: Out of beam γ -ray coincidence spectra for the 834.8 keV transition (top) and the 329.6 keV (bottom) transition. The open circles denote known contaminants: Au, Po (transitions near 835 keV) and ^{211}Fr (one transition at 327.3 keV).

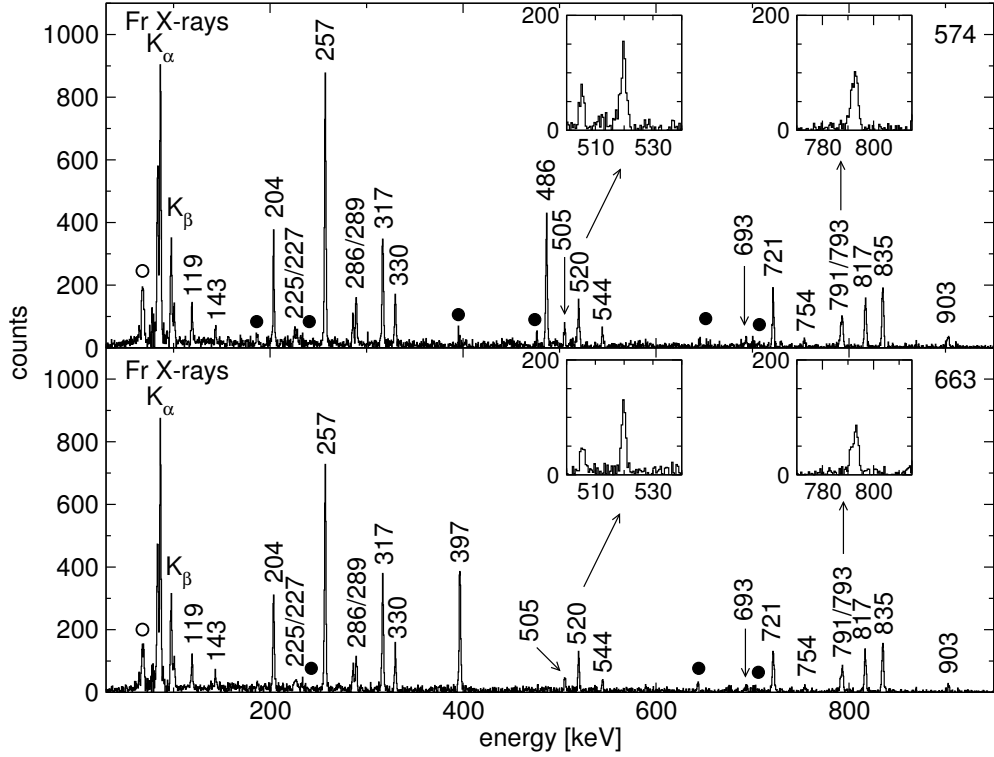


Figure 3.8: Out of beam γ -ray coincidence spectra for the 573.5 (top) and 663.3 keV (bottom) transitions.

3.2 The level scheme for ^{210}Fr

With this basic skeleton, the construction of the full level scheme for ^{210}Fr , shown in Figure 3.9, was made much easier. The description of this level scheme is separated into three parts. The first two treat the left hand side of the level scheme below and above the isomeric state at 2206 keV, the third discusses the right hand side of the level scheme. Properties of all transitions and states assigned to ^{210}Fr are presented in Table 3.3.

3.2.1 States and transitions below the state at 2206 keV

Ordering of transitions

In the region of the level scheme below the 2206 keV state, there are only five γ -rays, with energies of 304.2, 716.5, 774.5, 867.9 and 885.7 keV, that are observed in the prompt coincidences and that are not observed in the out-of-beam spectra. Of these transitions, the 867.9 and 885.7 keV lines are only in coincidence with the 816.8 keV γ -ray. This can be seen by subtracting the long out-of-beam coincidences from the prompt wide coincidences (see Figure 3.10). The 716.5 and 774.5 keV lines by-pass the isomer at 2206 keV, and do not reconnect with any of the higher energy states fed by the decay of the high spin isomer.

The pulsed beam data provides higher statistics and therefore more clarity with respect to the lowest intensity transitions that were originally shown in Figure 3.1. For example, the coincidence between the 721.2 and 753.8 keV lines is clearer (see Figure 3.11), similarly the coincidences between the parallel transitions, 225.4 and 289.1 keV transitions, and the 816.8 keV line are also more obvious. The prompt-wide spectrum for the 495.7 keV transition, however, is not convincing as the ratio of the 791 and 289 keV lines does not correspond to that expected for a transition placed between the 1337 and 842 keV states. This can be explained by the existence of a second 495.7 keV transition much higher in the scheme, explaining the presence of a relatively high intensity 791.0 keV peak, as well as a 793.0 keV γ -ray that should not be seen if there were to be only one 495.7 keV γ -ray in the level scheme (see Figure 3.11). Note also the absence of a 316.6 keV γ -ray in Figure 3.11. Finally the spectrum for the 63.8 keV line has more counts and confirms the argument made in the previous section (compare Figures 3.6 and 3.12).

3.2. THE LEVEL SCHEME FOR ^{210}Fr

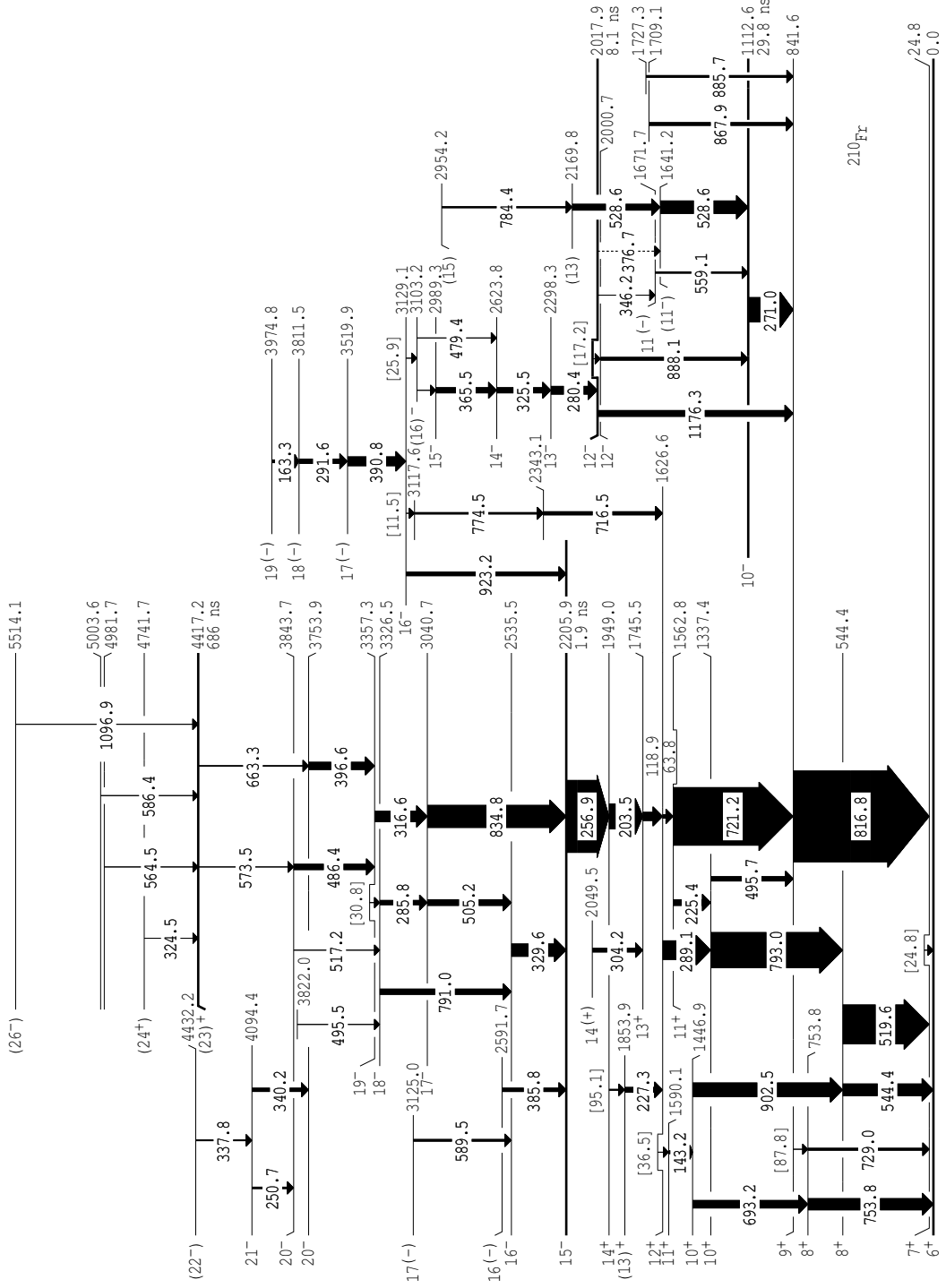


Figure 3.9: Level scheme for ^{210}Fr . The transition width indicates the prompt γ -ray intensity. States with a long lifetime are drawn with thicker lines and a label below the energy label indicates the lifetime. Transitions in square brackets and with no γ -ray intensity given are inferred from coincidence relationships and are not observed directly.

CHAPTER 3. EXPERIMENTAL RESULTS

Table 3.3: Properties of transitions assigned to ^{210}Fr .

$E_\gamma^{(a)}$	I_γ	A_2/A_0	E_i	E_f	J_i^π	J_f^π
11.5			3129.1	3117.6	16 $-$	
17.2			2017.9	2000.7	12 $-$	11 $-$
24.8			24.8	0	7 $+$	6 $+$
25.9			3129.1	3103.2	16 $-$	15 $-$
30.8			3357.3	3326.5	19 $-$	18 $-$
36.5			1626.6	1590.1	12 $+$	11 $+$
63.8	62(8)		1626.6	1562.8	12 $+$	11 $+$
87.8			841.6	753.8	9 $+$	8 $+$
95.1			1949.1	1854.0	14 $+$	(13) $^+$
113.9			3103.2	2989.3	15 $-$	14 $-$
118.9	125(7)	+0.36(4) ^(b)	1745.5	1626.6	14 $+$	12 $+$
143.2	52(4)	-0.32(4) ^(c)	1590.1	1446.9	11 $+$	10 $+$
154.8	15(5)					
163.3	50(5)	-0.29(4)	3129.2	2966.0	19 $(-)$	18 $(-)$
173.7	36(5)	-0.36(4) ^(c)				
203.5	355(9)	-0.39(4) ^(d)	1949.1	1745.5	15 $+$	14 $+$
225.4	90(8)	-0.21(4)	1562.8	1337.4	11 $+$	10 $+$
227.3	78(8)	+0.37(4)	1853.9	1626.6	13 $(+)$	12 $+$
250.7	32(5)	-0.26(7)	4094.4	3843.7	21 $-$	20 $-$
256.9	1000(25)	-0.27(3) ^(d)	2205.9	1949.0	16 $-$	15 $+$
265.6	51(5)	-0.30(7) ^(c)				
271.0	346(9)	-0.13(4) ^(d)	1112.6	841.6	10 $-$	9 $+$
280.4	119(3)	-0.11(4) ^(d)	2298.3	2017.9	13 $-$	12 $-$
285.8	71(5)	-0.35(2) ^(c)	3326.6	3040.8	18 $-$	17 $-$
289.1	268(9)	+0.29(3)	1626.6	1337.4	12 $+$	10 $+$
291.6	71(8)	-0.19(3)	3811.6	3520.0	18 $(-)$	17 $(-)$
304.2	64(6)	-0.32(4)	2049.7	1745.5	15 $(+)$	14 $+$
316.6	156(7)	+0.34(3)	3357.3	3040.7	20 $-$	18 $-$
324.5	6(3)		4741.7	4417.2		(23) $^+$
325.5	84(3)	-0.29(4)	2623.8	2298.3	14 $-$	13 $-$
329.6	182(7)	-0.42(4)	2535.5	2205.9	16 $-$	15 $-$
337.8	23(4)		4432.2	4094.4	22 $(-)$	21 $-$
340.2	58(7)	-0.28(5)	4094.4	3753.9	21 $-$	20 $-$
346.2	12(5)		2017.9	1671.7	12 $-$	11 $(-)$
365.5	84(3)	-0.54(3) ^(d)	2954.3	2623.8	15 $-$	14 $-$
376.7	8(4)		2017.9	1641.2	12 $-$	11 $(-)$
385.8	59(5)	-0.37(3)	2591.7	2205.9	16 $(-)$	15 $-$
390.8	134(8)	-0.41(4)	3520.0	3129.2	17 $(-)$	16 $-$
396.6	112(8)	-0.28(3)	3753.9	3357.3	20 $-$	19 $-$
405.6	71(7)	-0.54(6)				

Table 3.3. (*Continued*)

E_γ	I_γ	A_2/A_0	E_i	E_f	J_i^π	J_f^π
479.4	10(4)		3103.4	2623.8	16 $(-)$	14 $-$
486.4	86(6)	-0.34(4)	3843.7	3357.3	20 $-$	19 $-$
495.5			3822.0	3326.5		19 $-$
495.7	62(3)		1337.4	841.6	10 $^+$	9 $^+$
505.2	90(8)	-0.69(4)	3040.7	2535.5	17 $-$	16 $-$
519.6	547(15)	-0.44(3)	544.4	24.8	8 $^+$	7 $^+$
528.6	277(10) ^(e)		1641.2	1112.6	11 $(-)$	10 $-$
528.6	277(10) ^(e)		2169.8	1641.2		11 $-$
544.4	172(7)	+0.40(3) ^(c)	544.4	0	8 $^+$	6 $^+$
559.1	28(3)	-0.73(3) ^(d)	1671.7	1112.6	11 $-$	10 $-$
564.5	3(2)		4981.7	4417.2		(23) $^+$
573.5	13(5)	+0.35(7)	4417.2	3843.7	(23) $^+$	20 $-$
586.4	5(3)		5003.6	4417.2		(23) $^+$
589.5	36(5)	-0.69(9) ^(c)	3125.0	2535.5	18 $(-)$	17 $-$
663.6	18(6)	+0.41(6)	4417.2	3753.9	(23) $^+$	20 $-$
678.4						
693.2	115(4)	+0.16(4) ^(c)	1446.9	753.8	10 $^+$	8 $^+$
716.5	55(10)		2343.1	1626.6		
717.8	48(8)	+0.33(10) ^(c)				
721.2	803(20)	+0.27(3) ^(d)	1562.8	841.6	11 $^+$	9 $^+$
729.0	39(4)		753.8	24.8	8 $^+$	7 $^+$
753.8	166(8)	+0.37(3) ^(c)	753.8	0	8 $^+$	6 $^+$
774.5	31(6)	+0.42(21) ^(f)	3117.6	2343.1		
784.4	27(5)	+0.49(13) ^(g)	2954.2	2169.8		
791.0	85(7)	+0.25(10) ^(f)	3326.5	2535.5	18 $-$	16 $-$
793.0	495(12)	+0.33(4)	1337.4	544.4	10 $^+$	8 $^+$
796.5						
816.8	1259(28)	+0.28(2)	841.6	24.8	9 $^+$	7 $^+$
834.8	315(10)	+0.36(3) ^(c)	3040.7	2205.9	17 $-$	15 $-$
867.9	51(4)	-0.35(4) ^(d)	1709.1	841.6		10 $^+$
885.7	37(2)	(-0.16(16) ^(d))	1727.3	841.6		10 $^+$
888.1	51(3)	+0.77(27) ^(g)	2000.7	1112.6	11 $-$	10 $-$

Table 3.3. (*Continued*)

E_γ	I_γ	A_2/A_0	E_i	E_f	J_i^π	J_f^π
902.5	200(6)	+0.32(3)	1446.9	544.4	10^+	8^+
923.2	61(6)	-0.33(3)	3129.1	2205.9	$16^{(-)}$	15^-
1096.9	8(3)		5514.1	4417.2	(26^-)	$(23)^+$
1176.3	92(4)	+0.27(5)	2017.9	841.6	12^-	9^+

(*a*) Transitions in italics are inferred from coincidence logics and have not been directly observed.

(*b*) Angular anisotropy in a 519.6 keV gate.

(*c*) Angular anisotropy in a 256.9 keV gate.

(*d*) Angular anisotropy in a 816.8 keV gate.

(*e*) Sum of the intensities for the doublet of transitions at 528.6 keV; in the level scheme the intensity (width of the line) is shared 2/3 for the bottom transition and 1/3 for the top transition, see Figure 3.9.

(*f*) Angular anisotropy in the sum of gates on high intensity $E2s$ (specific $E2$ transitions depending upon the contamination in the gate) from the bottom of the level scheme.

(*g*) Angular anisotropy in a 271.0 keV gate.

Intensity flow

The structure of the level scheme is very fragmented above the ground state, with the four main paths (excluding the 816.8/271.0 keV and 816.8/1176.3 keV cascade), recombining at the 1627 keV state. The main cascade intensity passes through the 816.8/721.2 keV cascade but the 519.6(544.4)/792.9/289.1 keV path carries a quarter of all the intensity to the ground state. The two last paths are quite marginal in intensity, especially the 753.8(729.0)/693.3 cascade. The 716.5/774.5 keV branch bypasses the 2206 keV isomer from the 1627 keV state; it decays from a state that appears in the right-hand side of the level scheme. Above the 1627 keV state is fed by the 118.9/203.6/256.9 keV γ -ray cascade up to 2206 keV.

More detailed evidence for the placement of transitions is given in Appendix B.

3.2.2 States and transitions above the state at 2206 keV

The prompt-wide gated spectra for γ -rays below the state at 2206 keV show transitions not produced in the decay of the high-spin, long-lived isomer (see Figure 3.13). The 385.8 keV γ -ray is only seen in those spectra and there are no coincidences between this transition and γ -rays between the state at 2206 keV and the isomer. The 923.2 keV γ -ray is placed in a decay from 3129 keV state; this is shown on the right hand side of the level scheme. The 589.5 keV transition

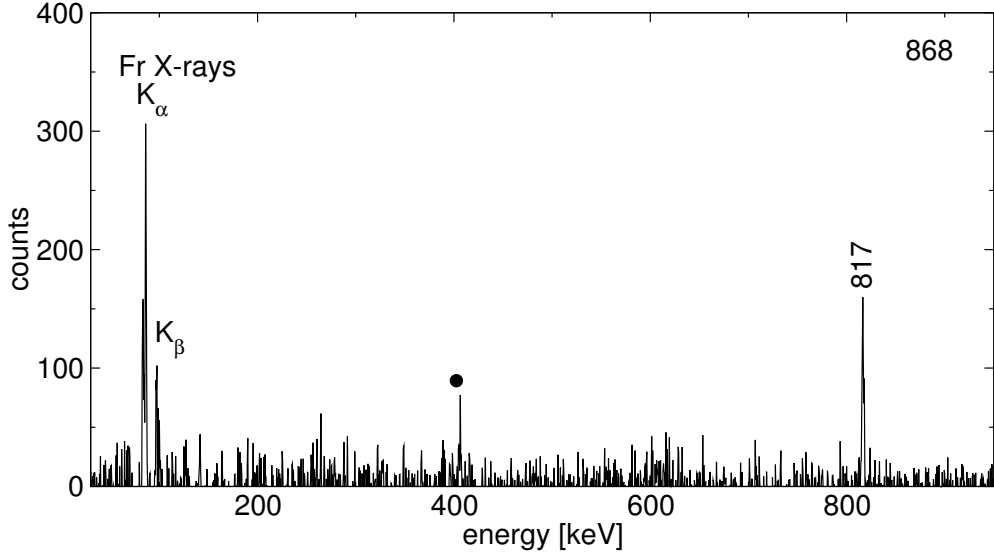


Figure 3.10: Prompt-wide spectrum for the 867.9 keV transition. The out-of-beam long coincidence spectrum has been normalised and subtracted. A similar spectrum is obtained for gates on the 885.7 keV transition.

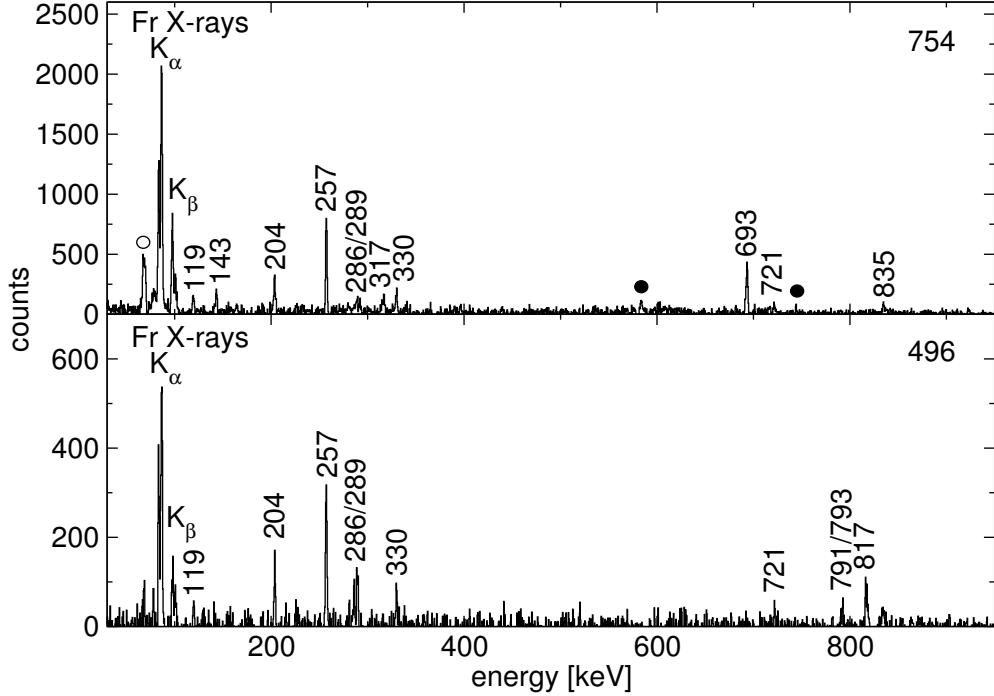


Figure 3.11: Prompt-wide coincidence spectra for the 753.8 keV line (top) and the 495.7 keV line (bottom). In the latter spectrum, note the similarity of the 386/330 keV ratio with that observed in the out-of-beam region. This suggests a 495.5 keV transition above the cascade. However the ratio 817/721 keV is too high, suggesting a second 495.7 keV γ -ray is parallel to the 721.2 keV transition. (See text for further details.)

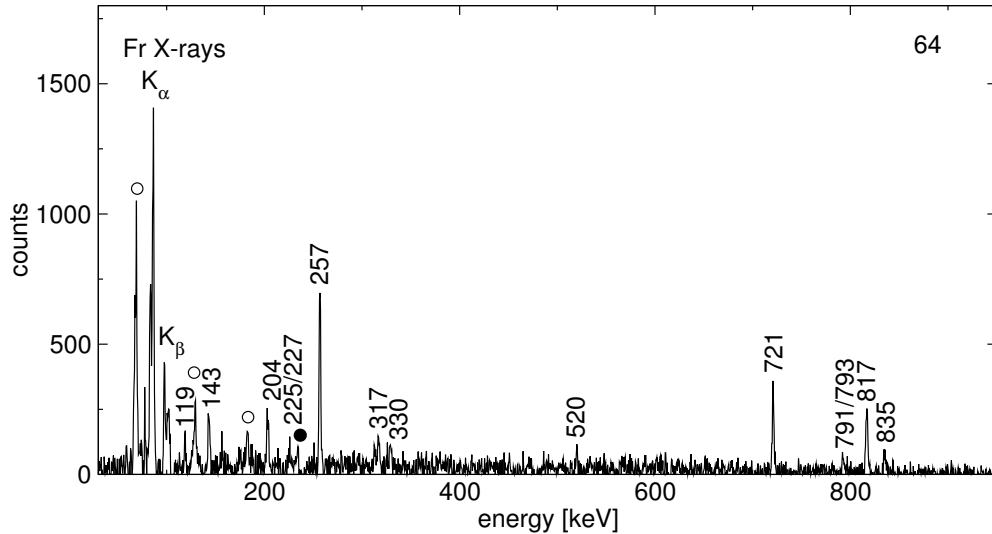


Figure 3.12: Prompt-wide HPGe coincidence spectrum for the 63.8 keV γ -ray observed in the LEPS detectors.

is observed in the prompt wide spectrum for 329.6 keV and for any transitions below the state at 2206 keV. A group of transitions at 154.8, 173.7, 265.6, 405.6 and 717.8 keV is seen in coincidence with the γ -rays below the state at 2206 keV. Some can also be seen in a prompt wide spectrum for 329.6 keV. Without more evidence, however, it is not possible to make definite assignments with regard to their placement in the level scheme. Finally, the group of transitions at 250.7, 337.8 and 340.2 keV are observed in all possible spectra from transitions in the decay from the high-spin, long-lived isomer, with the 250.7 keV absent from the coincidence spectrum for the 396.6 keV transition and the 340.2 keV from that for the 486.4 keV. Consequently this line defines a weak branch bypassing the long-lived isomer, up to a state at 4432 keV. The isomeric nature of the 4417 keV state is obvious from a study of prompt coincidences in which both the 663.3 and the 573.5 keV γ -rays are absent (see Figure 3.13).

Above the high-spin, long-lived isomer at 4417 keV

A sum of early-delayed long gates on the most intense transitions below the isomer (see Figure 3.14) shows four transitions at 324.5, 564.5, 586.4 and 1096.9 keV. These transitions are not in mutual coincidence so they have been placed in parallel feeding the 4417 keV isomer.

3.2. THE LEVEL SCHEME FOR ^{210}Fr

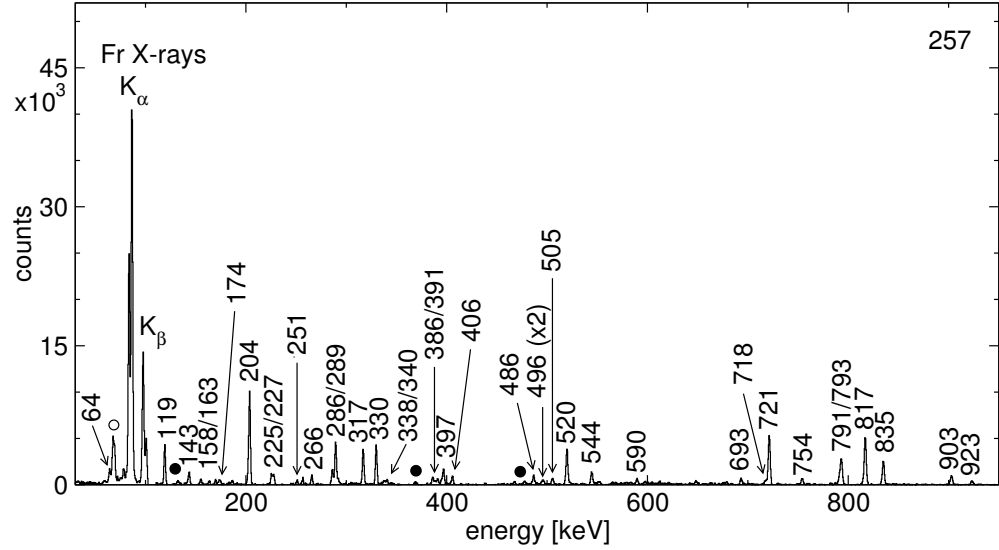


Figure 3.13: Prompt-wide coincidence spectrum for the 256.9 keV line. Note the absence of γ -rays at 574 and 663 keV.

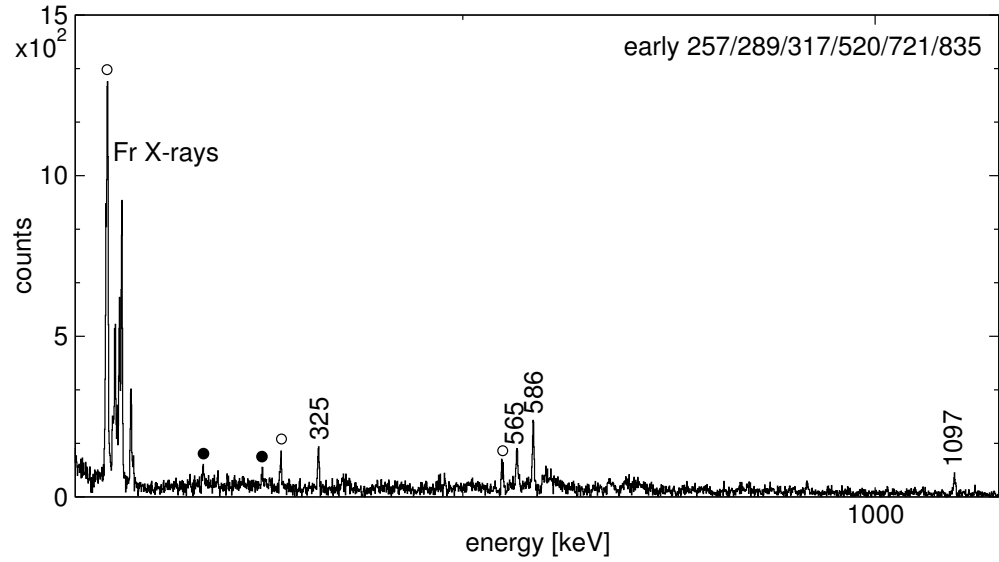


Figure 3.14: Sum of early coincidence spectra for 257, 289, 317, 520, 721 and 835 keV gates. (Other transitions had contaminated early coincidence spectra.)

3.2.3 States and transitions on the right hand side of the level scheme

Above the 842 keV state there are two transitions that feed from a distinct part of the level scheme: these are a 271.0 keV transition which leads to the 10^- isomer at 1113 keV and a 1176.3 keV that bypasses the isomer. The use of the $\gamma\gamma\gamma$ cube with gates on the 271.0 and 816.8 keV transitions shows the 528.6, 528.6, 784.4 branch. The prompt coincidence spectrum for the 528.6 keV γ -ray (see Figure 3.15) shows a second 528.6 transition and prevents the extraction of individual intensities for each of the two 528.6 keV γ -rays. It also exhibits a weak 784.4 keV transition. This path carries much of the intensity above the isomer at 1113 keV. However the early coincidence spectrum for the 271.0 keV transition demonstrates the presence of an additional two parallel paths. Comparison of the prompt coincidence spectra for 559.1, 888.1 and 528.6 keV (the last two are shown in Figure 3.15) clearly demonstrates that each of these γ -rays must directly feed the 1113 keV level.

The 280.4, 365.5, 325.5 keV lines are observed in early coincidence with the 271.0 keV transition and their prompt coincidence spectra clearly show the 1176.3 and 888.1 keV transitions. They also exhibits a different ratio $I_\gamma(816.8) / I_\gamma(271.0)$ to that observed in the prompt coincidence spectra for 528.6, 559.1 and 888.1 keV. This is a strong indication that the cascade is above the 1176.3 and 888.1 keV decays, with the 1176.3 keV transition feeding the 841.6 keV state, effectively bypassing the isomer at 1113 keV. It also suggests an unobserved 17.2 keV transition connecting the initial state of the 888.1 keV transition (2001 keV) to the final state of the 1176.3 keV transition (2018 keV).

The lack of coincidences between the 365.5 and the 479.4 keV γ -rays, places these in parallel, above the 280.4 and the 325.5 keV transitions. Three γ -rays at 163.4, 390.8 and 291.6 keV with tentative ordering can be observed above the 2989 keV state. The prompt coincidence spectra for each of these show all the transitions from the de-excitation of the isomer at 2206.0 keV. They also show the 716.5 and 774.5 keV transitions which were observed in the prompt gates for transitions from decays below the 1627 keV state. If the 923.2 keV transition is directly between the 2206 keV state and the 163.3/291.6/390.8 keV cascade, then two low energy transitions (11.6 and 26.0 keV) are required to fill the energy gaps between the 3129 keV state and the 3118 and 3103 keV states.

The prompt coincidence spectra for the 816.8, 271.0, 559.1, 280.4, 325.5 and 365.5 keV transitions show a weak 346.2 keV transition whose intensity places it above the 559.1 keV γ -ray.

3.3. LIFETIMES

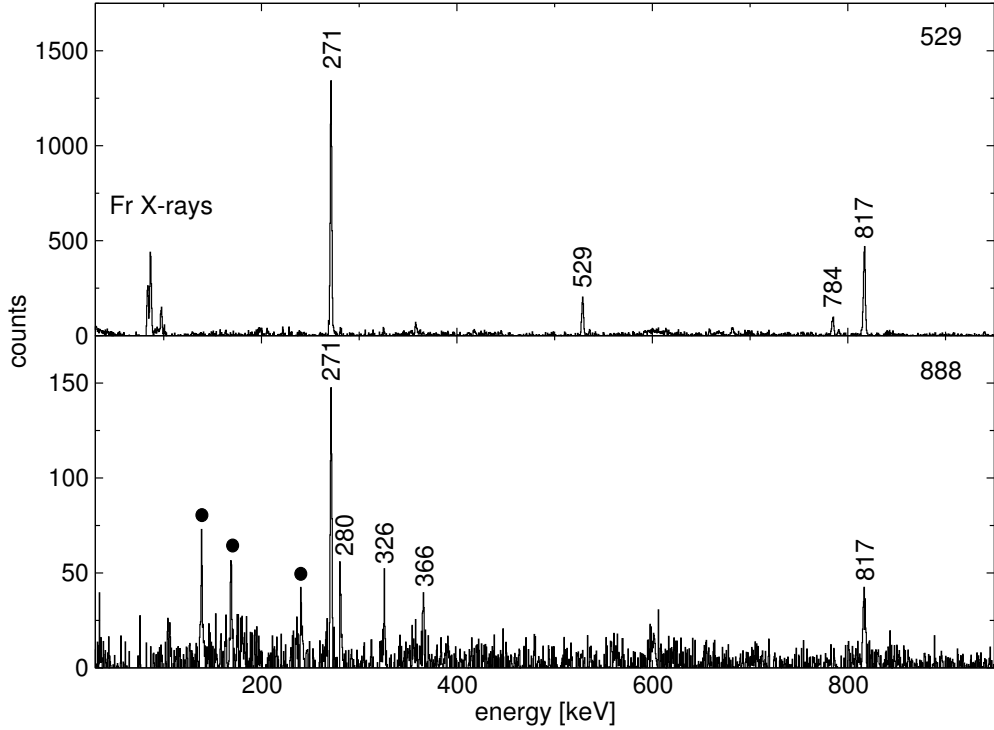


Figure 3.15: Prompt-wide coincidence spectra with gates on the 528.6 and 888.1 keV lines.

3.3 Lifetimes

This section reports the lifetime measurements for each of the isomers observed in ^{210}Fr .

The different mean-lives require the different techniques that were explained in Chapter 2. Figures 3.16 through 3.20, respectively, show the various lifetime determinations.

3.3.1 The isomer at 1113 keV

Because of the high level of contamination around the 271.0 keV γ -ray, especially the two 269 keV transitions produced via Coulomb excitation of the ^{197}Au target, the beam- γ data could not be used for the determination of the mean-life of the 1113 keV state. Instead the lifetime was determined from $\gamma\text{-}\gamma\text{-}\Delta T$ spectra obtained in the 1/15 beam pulsing experiment (1/1712 ns). Figure 3.16 shows the $\gamma\text{-}\gamma\text{-}\Delta T$ spectrum with gates on the 817 and 529 keV lines.

An independent confirmation of this lifetime was obtained from the decay curve of the 271.0 keV transition observed in the second experiment. The combination of the two measurements shown in Figures 3.16 and 3.17 gives the lifetime

of the 10^- state in ^{210}Fr at $29.8(11)$ ns.

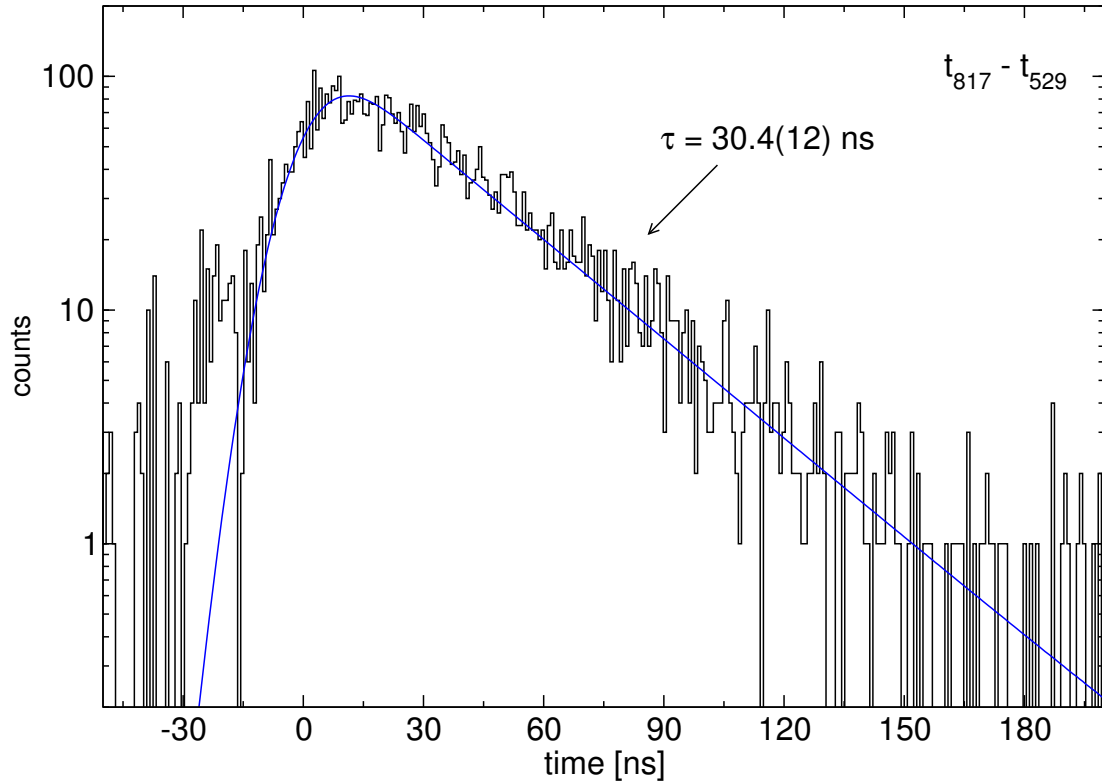


Figure 3.16: Time difference between the 816.8 and 528.6 keV transitions. A lifetime of $\tau = 30.4(12)$ ns is inferred for the state between the two transitions.

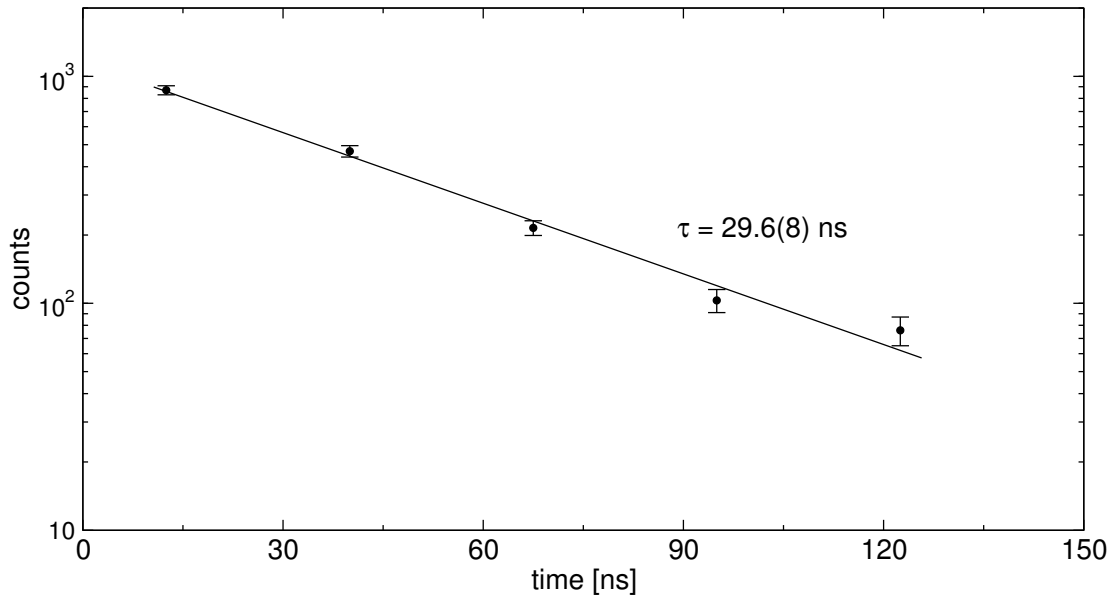


Figure 3.17: Intensity of the 271.0 keV γ -ray as a function of time in the $1/9 \mu\text{s}$ long chopping data. A lifetime of $\tau = 29.6(8)$ ns is deduced.

3.3. LIFETIMES

3.3.2 The isomer at 2018 keV

Figure 3.18 shows a beam- γ measurement of the lifetime for the state at 2018 keV that decays via the 1176.3 keV transition. A lifetime of $8.1(4)$ ns is deduced. Although this is supported by γ - γ -time difference measurements, for example that obtained from the 1176.3/280.4 keV transition pair, the lower statistics that results from the requirement that both of the two γ -rays must be measured, meant that no reliable fitted lifetime could be determined from those spectra.

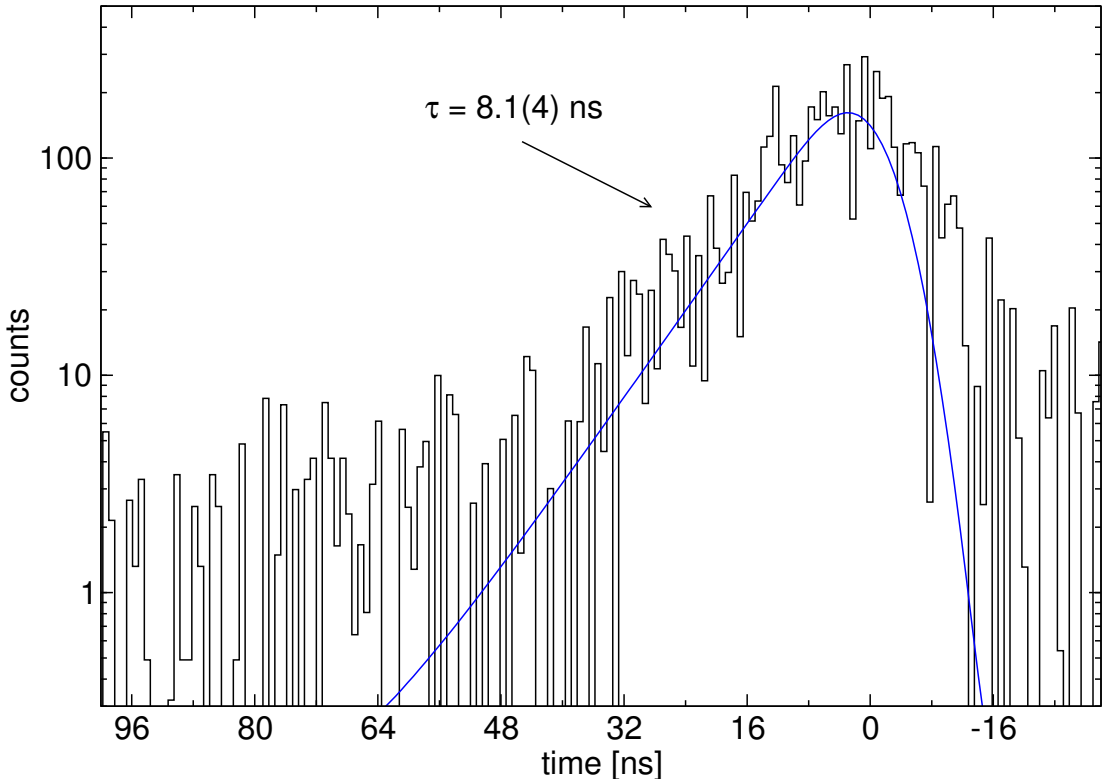


Figure 3.18: Intensity of the 1176.3 keV γ -ray as a function of time with respect to the beam pulse. A lifetime of $\tau = 8.1(4)$ ns is seen.

3.3.3 The isomer at 2206 keV

The lifetime of the isomer at 2206 keV was obtained using the centroid shift method (see Section 2.6) for time responses measured in the γ - γ - ΔT cube. This method requires the knowledge of the prompt responses between a γ -ray in a narrow energy region (call it region A) and a range of γ -rays with different energy. This will yield a prompt response curve. Note that the prompt curve can be determined using coincidence relationships from other nuclei produced in the experiment, providing that those nuclei have at least one transition with energy in region A as well. Measuring time differences across the isomer with one of

the energy gates still in region A will show a constant time gap with the prompt response that corresponds to the lifetime of the isomer. In practice, this is done as of Figure 3.19. If a lifetime is assumed at the 2206 keV level, blue points represent time differences between pairs of transitions nominally in prompt coincidence, while red points are for pairs nominally separated by the isomer. The difference corresponds to the isomer lifetime and the directions of the observed shifts of the time difference spectra always have the correct sign expected given the placement of the isomer at the 2206 keV level. In Figure 3.19 (bottom panel) two different gates are used (on the 256.9 keV line, top panel, and on the 816.8 keV line, bottom panel) with fits of the time responses that correct for the energy-dependent walk, resulting in approximatively constant behaviour. This can be performed for a wide range of γ -rays and the results obtained are presented in Table 3.4. Not correcting for the walk results in a brutal fall of the time differences at low energies (see top panel of Figure 3.19), due to the longer time for low energy transitions' detection. The lifetime deduced for the 2206 keV isomer, combining the two techniques (and using Eq. 2.19), is 1.9(4) ns.

Table 3.4: The average of the time responses for transitions in prompt coincidence (2nd column) and in delayed coincidence (3rd column) with γ_1 is compared. (The method for obtaining the quoted values for the 256.9 and 816.8 keV transitions is presented in Figure 3.19, bottom panel.) The signs of the time difference (ΔT) values always agree with the placement of the isomer being at the 2206 keV level. The weighted average is: $\tau = 1.9(4)$ ns .

E_{γ_1} (keV)	Prompt Resp. (ns)	Across isomer Resp. (ns)	$ \Delta T $ (ns)	Number of centroids
203.6	0.09	2.33	2.2(4)	8
256.9	0.71	2.77	2.1(5)	14
329.6	-0.58	1.30	1.9(6)	7
519.6	0.48	2.70	2.1(4)	8
544.4	0.41	1.23	0.8(3)	6
721.2	0.43	2.24	1.8(2)	6
792.9	-0.28	1.59	1.9(5)	9
816.8	-0.22	1.94	2.2(3)	9
834.8	-0.02	-1.69	1.7(3)	7

3.3.4 The isomer at 4417 keV

While the presence of an isomer was apparent in the first pulsed beam experiment, the pulse separation was not optimal for the isomer lifetime, given that

3.3. LIFETIMES

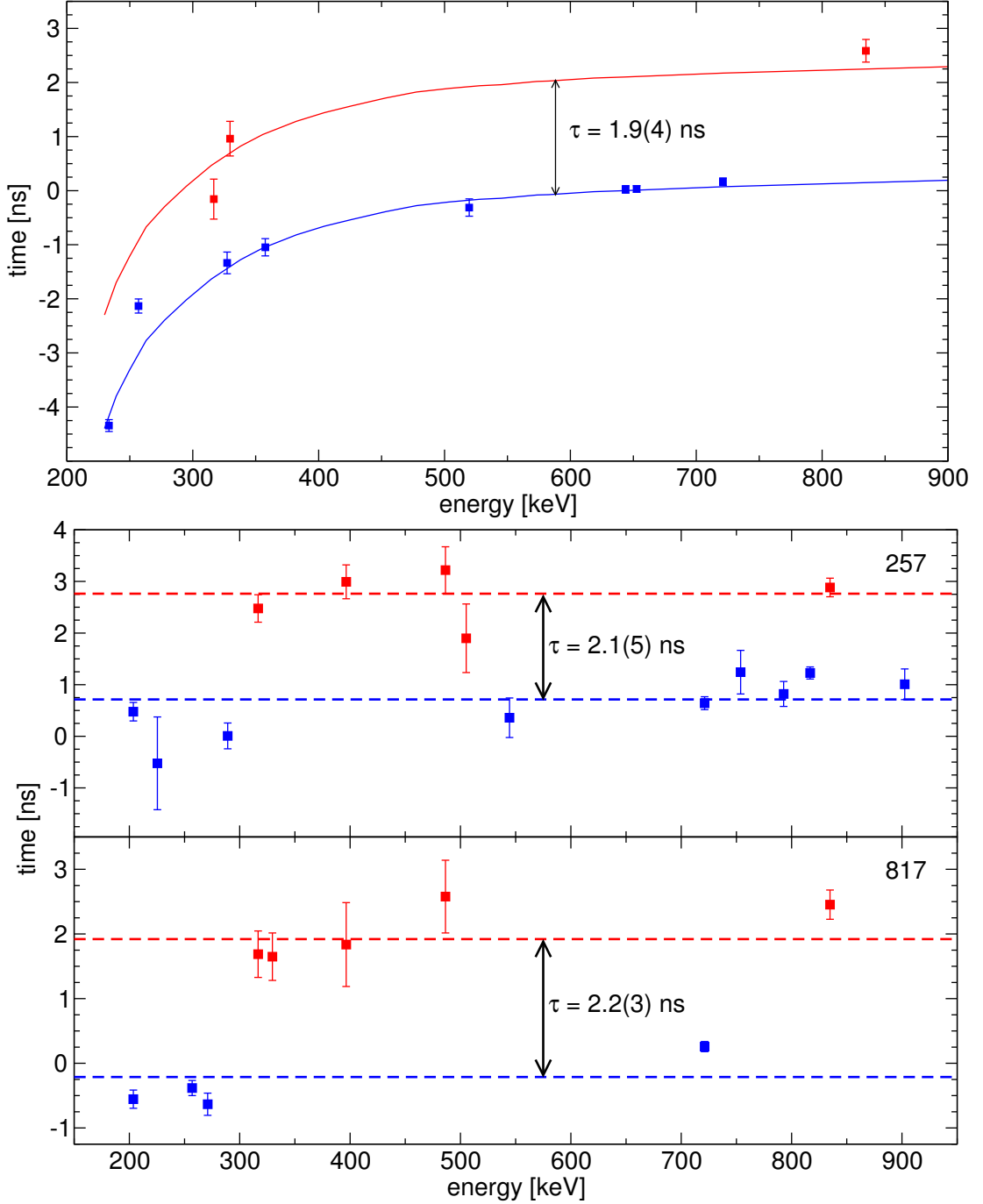


Figure 3.19: (Top panel) Centroid positions for the time difference between (mainly) the 816.8 keV transition and other γ -rays as a function of their energy. The ΔT spectra were fitted using a symmetric Gaussian. (Bottom panel) Centroid positions for the time difference between the 816.8 keV (and 256.9 keV) transition and other transitions as a function of their energy. The ΔT spectra were fitted using an asymmetric Gaussian to take the walk into account. See text for more details.

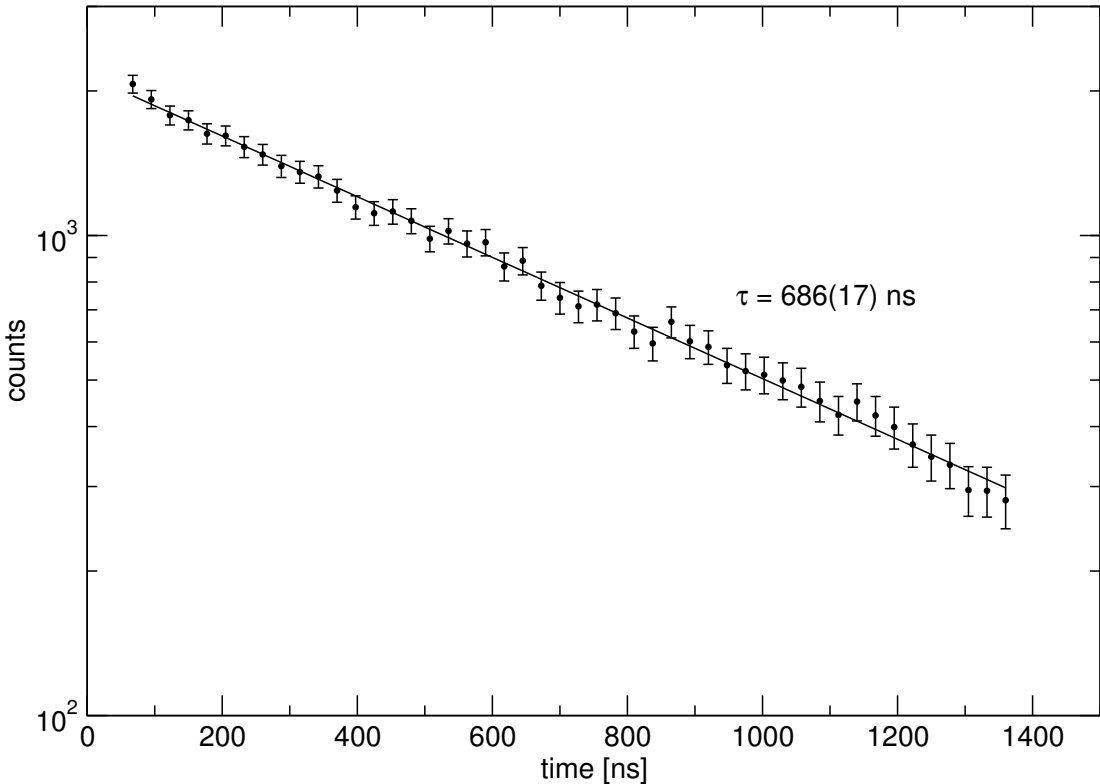


Figure 3.20: Intensity of γ -ray coincidences below the 4417 keV isomer as a function of time.

the isomer lifetime was too long to render a γ - γ - ΔT measurement practical. The lifetime was obtained in the second experiment by measuring the time-dependence of the coincidence intensity for the de-exciting γ -rays. The lifetime of the isomer is 686(17) ns (see Figure 3.20). Each point on this curve represents the γ -ray intensities measured in gated spectra obtained with contiguous time gates after contamination from long-lived activity was subtracted.

3.4 Spin and parity assignments

The ground state spin of ^{210}Fr was measured to be $6\hbar$ through on-line atomic beam magnetic resonance techniques [Ekst 78]. Positive parity can be safely assumed from the expected ground state configuration of ^{210}Fr , $\pi(h_{9/2}^5)\nu(p_{1/2}^{-2}f_{5/2}^{-1})$. In the ground state the two neutron holes in the $p_{1/2}$ orbital and four protons in the $h_{9/2}$ shell will couple to zero angular momentum while the remaining $\pi h_{9/2}\nu f_{5/2}^{-1}$ can couple to $J = 1\dots 7$. The proton-neutron interactions, however, do not favour mutual alignment of protons and neutron-holes and $J = 6$ is energetically favoured (see for example Ref. [Kuo 71]). Calculations (see Chapter 4) suggest that the

3.4. SPIN AND PARITY ASSIGNMENTS

lowest 6^+ and 7^+ members of the $\pi(h_{9/2}^5) \nu(p_{1/2}^{-2}f_{5/2}^{-1})$ multiplet will lie close to each other (see Figure 4.9). This is supported through the observation of the 24.8 keV state. Therefore the spin and parity assignments in this section start from an assumption of 6^+ for the ground state of ^{210}Fr .

Transition multi-polarity assignments in the following sections rely on γ -ray angular anisotropies and total conversion coefficient measurements from intensity balances. Angular distributions for uncontaminated transitions assigned to ^{210}Fr were measured by projecting spectra for the three set of angles from the $\gamma\gamma$ coincidence data. In some other cases, angle-projected gated coincidence spectra were used. The values deduced for A_2/A_0 (A_4 was set to zero) are given in Table 3.3.

When discussing the multi-polarities it is important to consider implied transition strengths. For example, one would expect to see a long lifetime when making $M2$ or $E3$ assignments for transitions of less than a few hundred keV. The expected lifetimes for a state decaying by a pure transition of strength 1 W.u. for any of $E1$, $M1$, $E2$, $M2$, $E3$ and $M3$ multi-polarity are shown in Figure 3.21. Strengths deduced from the observed lifetimes or lifetime limits and the spin assignment are presented in Table 3.5.

3.4.1 States below the isomer at 2206 keV

The angular distributions measured for the 817 and 721 keV γ -rays are $+0.28(2)$ and $+0.27(3)$, respectively, consistent with quadrupole assignments. Alternative $M2$ or $E3$ multi-polarities are excluded due to the observed lifetime limits for the 842 and 1563 keV states of < 1.5 ns.

The angular distribution for the 520 keV γ -ray is $-0.44(3)$ while the 544 keV transition has a large positive value, $A_2/A_0 = +0.40(3)$. The coefficient for the 520 keV transition is consistent with stretched dipole or mixed $\Delta J=1$ dipole/quadrupole, while the 544 keV γ -ray could be stretched $E2$, $M2$, $E3$ or mixed $M1/E2$ or $E1/M2$. The implied transition strength for the 544 keV γ -ray, however, eliminates the $M2$ (> 3.8 W.u.) and $E3$ ($> 7.1 \times 10^3$ W.u.) possibilities. Hence the 544 keV transition must not change the parity between the parent and daughter states which rules out mixed $E1/M2$ assignment for the 520 keV transition. Finally the conversion coefficient measured for the 544.4 keV transition from intensity balances, $0.19(7)$, is also in agreement with an $M1$ value. As a result, $M1/E2$ and $E2$ assignments for the 520 keV and the 544 keV γ -rays, respectively, are the most consistent choice and give $J^\pi = 8^+$ for the state at 544 keV.

Similar arguments for the 754 and 729 keV γ -rays lead to another 8^+ state at 754 keV. The low spin compared to the ground state is consistent with its

Table 3.5: Gamma-ray branching ratios and transition strengths for selected states in ^{210}Fr .

Initial state, τ	Final state, J^π	E_γ (keV)	I_γ	$\sigma\lambda$	$\alpha_T^{(a)}$	$B(\sigma\lambda)$ ($e^2\text{fm}^{2\lambda}$ or $\mu_0\text{fm}^{2(\lambda-1)}$)	Transition strength (W.u.)
$8^+ 544 \text{ keV}$ $< 1.5 \text{ ns}$	6^+ 7^+	544.4 519.6	345(13) 1000(28)	$E2$ $M1$	0.03023 0.1472	> 0.2 $> 1.0 \times 10^{-4}$	> 0.0028 $> 7.6 \times 10^{-6}$
$8^+ 754 \text{ keV}$ $< 1.5 \text{ ns}$	6^+ 7^+	753.8 729.0	1000(34) 256(19)	$E2$ $M1$	0.01496 0.06008	> 1.6 $> 1.9 \times 10^{-5}$	> 0.02 $> 1.1 \times 10^{-5}$
$9^+ 842 \text{ keV}$ $< 1.5 \text{ ns}$	7^+	816.8	1000	$E2$	0.01272	> 1.5	> 0.02
$10^+ 1337 \text{ keV}$ $< 1.5 \text{ ns}$	8^+ 7^+	793.0 495.7	1000(30) 76(10)	$E2$ $M1$	0.01350 0.1667	> 1.5 $> 1.9 \times 10^{-5}$	> 0.02 $> 1.0 \times 10^{-5}$
$10^+ 1447 \text{ keV}$ $< 1.5 \text{ ns}$	8^+ 7^+	902.5 693.3	1000(31) 657(24)	$E2$ $E2$	0.01044 0.01781	> 0.5 > 1.3	> 0.007 > 0.01
$11^+ 1563 \text{ keV}$ $< 1.5 \text{ ns}$	9^+ 10^+ 10^+	721.2 225.4 225.4	1000(29) 109(7) 109(7)	$E2$ $M1$ $M1$	0.01639 0.1436 0.184(78)	> 2.3 $> 3.0 \times 10^{-4}$ $> 2.9 \times 10^{-4}$	> 0.03 $> 1.7 \times 10^{-4}$ $> 1.6 \times 10^{-4}$
$11^+ 1590 \text{ keV}$ $< 1.5 \text{ ns}$	10^+ 10^+	143.2 1000	M1 M1	5.156 5.39(63)	> 0.002 > 0.002	> 0.001 > 0.001	
$12^+ 1627 \text{ keV}$ $< 1.5 \text{ ns}$	10^+ 11^+ 11^+	289.1 63.8 36.5	1000(40) 152(20) $20(3)$	$E2$ $M1$ $M1$	0.1620 9.9(11) 53.84	> 61 > 0.005 > 0.003	> 0.82 > 0.003 > 0.002

Table 3.5. (*Continued.*)

Initial state, τ	Final state, J^π	E_γ (keV)	I_γ	$\sigma\lambda$	$\alpha_T^{(a)}$	$B(\sigma\lambda)$ ($e^2 \text{fm}^2 \text{ or } \mu_0 \text{ fm}^2 \text{ s}^{-1}$)	Transition strength (W.u.)
14 ⁺ 1746 keV	12 ⁺	118.9	1000	$E2$	4.266	$> 4.3 \times 10^3$	> 58
< 1.5 ns							
13 ⁺ 1746 keV	12 ⁺	118.9	1000	$M1$	8.752	$> 2.3 \times 10^{-3}$	$> 1.3 \times 10^{-3}$
< 1.5 ns							
13 ⁺ 1746 keV	12 ⁺	118.9	93(5)	$M1$	8.752	$> 1.91(15) \times 10^{-3}$	$> 1.07(8) \times 10^{-3}$
< 1.5 ns		36(6)		$E2$	4.266	$> 752(132)$	$> 10(2)$
14 ⁺ 1854 keV	12 ⁺	227.3	1000	$E2$	0.3532	$> 6.58 \times 10^2$	> 8.8
< 1.5 ns							
15 ⁻ 2206 keV	14 ⁺	256.9	1000	$E1$	0.04881	$1.96(44) \times 10^{-5}$	$8.6(19) \times 10^{-6}$
1.9(4) ns							
16 ⁻ 2536 keV	15 ⁻	329.6	1000	$M1$	0.533(92)	$> 5.7 \times 10^{-4}$	$> 3.2 \times 10^{-4}$
< 1.5 ns							
17 ⁻ 3041 keV	15 ⁻	834.8	1000(31)	$E2$	0.01218	> 0.6	> 0.009
< 2.5 ns	16 ⁻	505.2	172(11)	$M1$	0.1587	$> 2.3 \times 10^{-5}$	$> 1.3 \times 10^{-5}$
18 ⁻ 3327 keV	16 ⁻	791.0	1000(38)	$E2$	0.01350	> 0.5	> 0.007
< 2.5 ns		285.8	621(30)	$M1$	0.7437	$> 2.6 \times 10^{-4}$	$> 6.8 \times 10^{-5}$
19 ⁻ 3357 keV	17 ⁻	316.6	1000(31)	$E2$	0.1233	> 65	> 0.9
< 2.5 ns		30.9	4.3(5)	$M1$	88.03	$> 2.0 \times 10^{-3}$	$> 1.1 \times 10^{-3}$

Table 3.5. (*Continued.*)

Initial state, τ	Final state, J^π	E_γ (keV)	I_γ	$\sigma\lambda$	$\alpha_T^{(a)}$ $(e^2 \text{fm}^{2\lambda} \text{ or } \mu_0 \text{fm}^{2(\lambda-1)})$	$B(\sigma\lambda)$ $(e^2 \text{fm}^{2\lambda} \text{ or } \mu_0 \text{fm}^{2(\lambda-1)})$	Transition strength (W.u.)
$(23)^+ 4417 \text{ keV}$							
686(17) ns	20^-	663.3	524(14)	$E3$	0.0569	$2.21(8) \times 10^4$	8.4(3)
	20^-	573.5	476(12)	$E3$	0.0861	$5.56(21) \times 10^4$	21.2(8)
$(22)^+ 4417 \text{ keV}$							
686(17) ns	20^-	663.3	524(14)	$M2$	0.1980	$3.52(13) \times 10^{-1}$	$6.03(2) \times 10^{-3}$
	20^-	573.5	476(12)	$M2$	0.3033	$6.61(23) \times 10^{-1}$	$1.13(4) \times 10^{-2}$
$(22,23)^+$							
4417 keV							
686(17) ns	$(20,21)^-$ $(19,20)^-$	663.3 573.5	524(14) 476(12)	$M2$ $E3$	0.1980 0.0861	$0.384(16)$ $5.20(21) \times 10^4$	$6.58(3) \times 10^{-3}$ 19.9(8)
$(22,23)^+$							
4417 keV							
686(17) ns	$(19,20)^-$ $(20,21)^-$	663.3 573.5	524(14) 476(12)	$E3$ $M2$	0.0569 0.3033	$2.02(8) \times 10^4$ $0.703(28)$	$7.7(3)$ $1.20(5) \times 10^{-2}$
$12^- 2018 \text{ keV}$							
8.1(4) ns	9^+	1176.3	92(4)	$E3$	0.04053	$3.8(4) \times 10^4$	14.5(15)
	11^-	376.7	8(4)	$M1$	0.351	$9(4) \times 10^{-6}$	$5(3) \times 10^{-6}$
11-	346.2	12(5)	$M1$	0.440		$1.7(7) \times 10^{-5}$	$9(3) \times 10^{-6}$
	11-	17.2	< 5 ^(b)	$M1$	123.6 ^(c)	$9.3(25) \times 10^{-3}$	$5.2(14) \times 10^{-3}$
10 ⁻ 1113 keV							
29.8(11) ns	9^+	271.0	100	$E1$	0.0431	$1.01(4) \times 10^{-6}$	$4.5(2) \times 10^{-7}$

(a) Values taken from Ref. [Kibe 08].

(b) Estimated from $I_\gamma(888.1 \text{ keV}) = 574(37)$, $\sigma\lambda(888.1 \text{ keV}) = M1$ and $\alpha_T(888.1 \text{ keV}) = 0.0358$.(c) A $J \rightarrow J$ transition is likely to be a mixed $M1/E2$. In such a case the IGC would be higher ($\alpha_T(17.2 \text{ keV}; E2) = 29490$).

3.4. SPIN AND PARITY ASSIGNMENTS

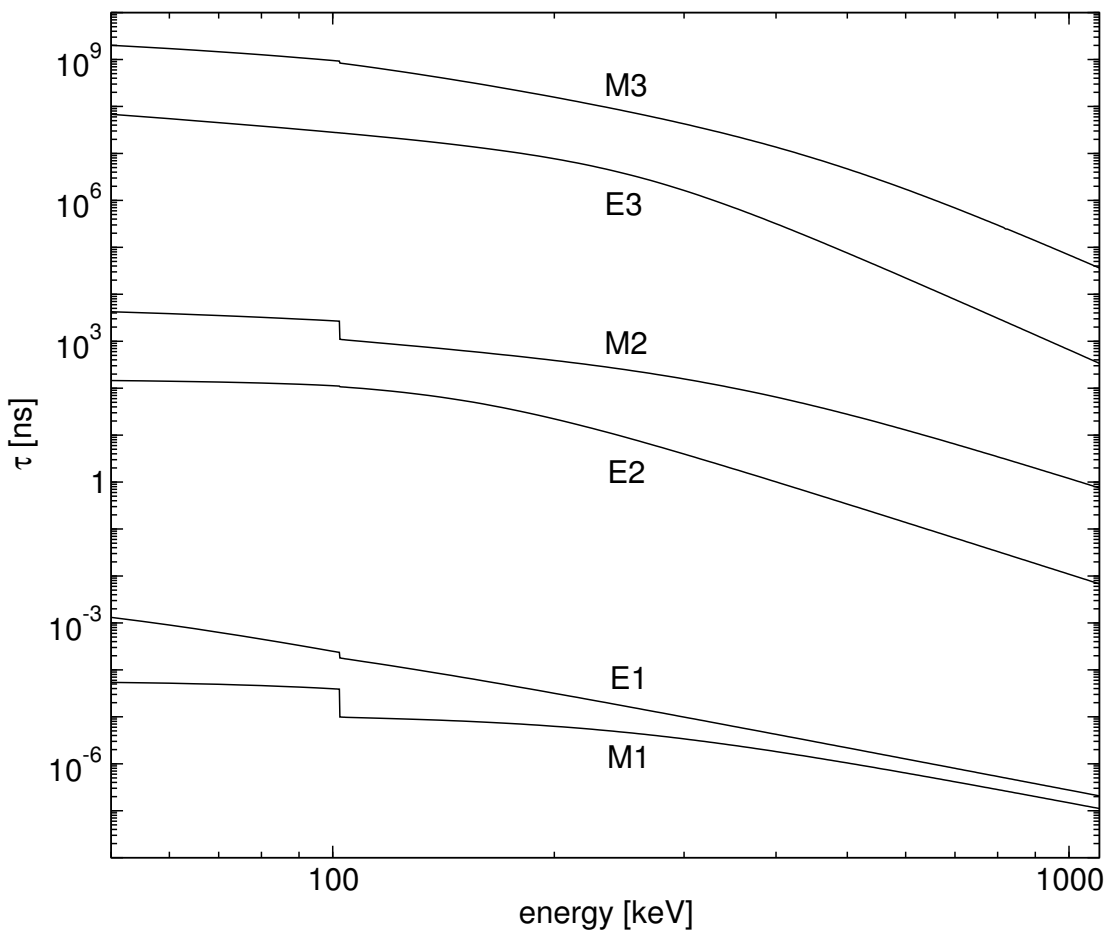


Figure 3.21: Expected lifetimes for states that decay through pure multi-polarity transitions with a strength of 1 W.u., as a function of the transition energy. The effects of internal conversion are included and the calculations are for Z=87 (francium).

Table 3.6: Total conversion coefficients for selected transitions in ^{210}Fr , deduced from intensity balance measurements.

E_γ (keV)	α_T measured	$\alpha_T^{(a)}$					Details ^(b)
		$E1$	$M1$	$E2$	$M2$	$E3$	
63.9	28(5)	0.355	10.4	74.1	319.7	3051	Tables C.1, C.2
118.9	9.8(6)	0.311	8.75	4.27	59.2	89.96	Tables C.3, C.4
143.2	2.7(4)	0.198	5.16	1.98	30.0	32.7	Tables C.2, C.3, C.4
203.5	1.94(15)	0.0846	1.91	0.520	8.61	5.31	Table C.2
256.9	0.06(5)	0.0488	0.998	0.235	3.88	1.75	Table C.1
271.0	< 0.07	0.0431	0.861	0.198	3.24	1.37	Table C.7
285.8	0.8(3)	0.0382	0.744	0.168	2.71	1.09	Table C.1
316.6	0.13(7)	0.0303	0.562	0.123	1.94	0.701	Tables C.1, C.2
329.6	0.40(9)	0.0277	0.503	0.110	1.70	0.594	Table C.1
519.6	0.19(7)		0.147				

^(a) Calculated values from Ref. [Kibe 08].

^(b) Complete detail of the measurements can be found in the indicated tables of Appendix C.

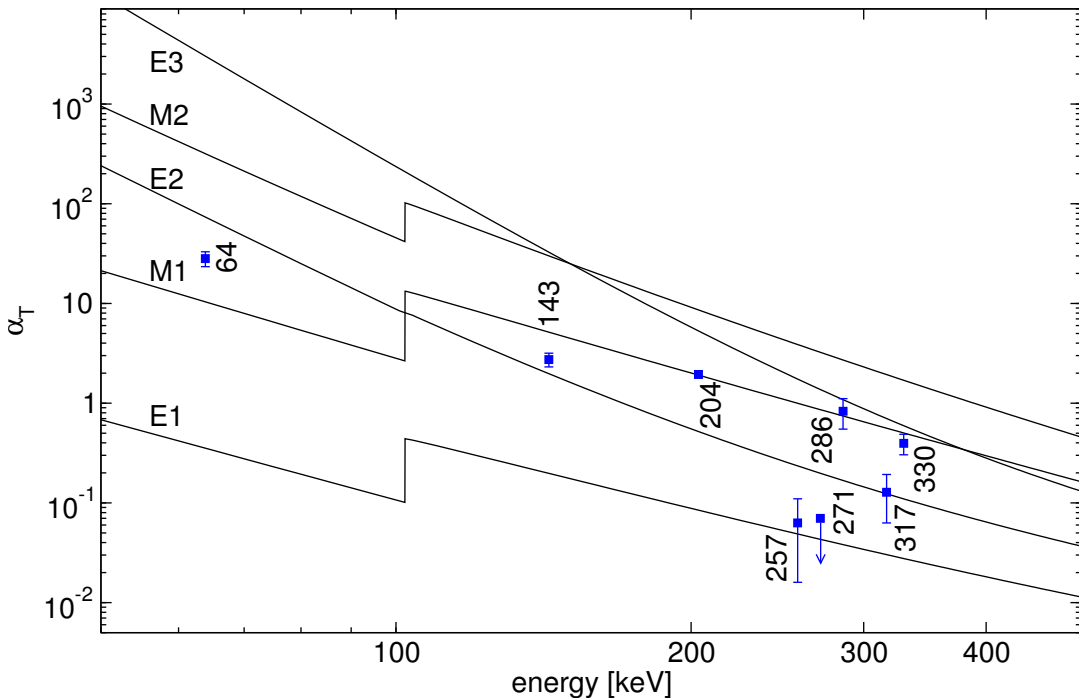


Figure 3.22: Comparison of measured total conversion coefficients for selected transitions in ^{210}Fr with calculated values for pure transitions from Ref. [Kibe 08].

3.4. SPIN AND PARITY ASSIGNMENTS

population in the α decay of ^{214}Ac as observed by Kuusiniemi *et al.* [Kuus 04].

The 793 keV transition has a positive anisotropy, +0.33(4), and is competing with a low intensity 495.7 keV transition for which the angular distribution cannot be obtained. However on the basis of strength requirements the only possibilities for the 793 and 496 keV transitions are $E2$ and $M1$, respectively. This results in $J^\pi = 10^+$ for the state at 1337 keV. As a result, an $M1$ or mixed $M1/E2$ assignment for the 225 keV transition is indicated.

The 693 and 903 keV transitions with angular distributions +0.16(4) and +0.32(3), respectively, can be assigned stretched $E2$ multi-polarities, establishing a second 10^+ state at 1447 keV. Above this state, the 143.2 keV γ -ray has a large negative angular distribution (see Table 3.3) that indicates a $\Delta J=1$ dipole/quadrupole transition while the conversion coefficient, 2.7(4), is consistent with a $M1/E2$ assignment. This gives $J^\pi = 11^+$ for the state at 1590 keV.

Information for the 64 keV transition is difficult to obtain due to the proximity of the (gold) X-rays and the low detection efficiency at that energy. In particular, angular distribution measurements were not possible. However, the total conversion coefficient $\alpha_T = 28(5)$, is consistent with an $M1/E2$ assignment (see Table 3.3) and $J^\pi = 12^+$ for the state at 1627 keV. Two other branches reach that state. The 289 keV transition has an angular distribution of +0.29(3) which agrees with a stretched $E2$ multi-polarity and, being constrained to decay from the 1627 to the 1337 keV states (from coincidence requirements), is most likely a pure $E2$ γ -ray. The transition strength limit, > 0.82 W.u., also supports the assignment and further suggests the state may have a possible lifetime of some fraction of a nanosecond. This is, indeed, similar to the 233 keV, $21/2^- \rightarrow 17/2^-$, $E2$ transition in ^{211}Fr which decays from a state with a 3.0(3) ns lifetime and has a $B(E2)$ of 4.0(4) W.u. [Byrn 86b]. The configurations in ^{211}Fr and ^{210}Fr are expected to have similarities in this region of the level scheme; these will be discussed in Chapter 4.

The 119 keV γ -ray has $A_2/A_0 = +0.36(4)$, suggesting $E2$, $M2$, $E3$ or mixed $M1/E2$ or $E1/M2$ assignment. Pure $M2$ and $E3$ assignments are clearly unrealistic for such a low energy transition so that, at first glance, one would expect an $E2$ assignment. However the measured conversion coefficient of 9.8(6) is in agreement with an $M1$ assignment (see Table 3.3). Note that the total internal conversion coefficient and the angular distribution do not agree as no $M1/E2$ mixing ratio can explain both simultaneously. The 204 keV transition has a distribution and conversion coefficient that agree with an $M1$ assignment. The angular distribution for the 227 keV γ -ray suggests an $E2$ assignment, however $M1/E2$ character cannot be excluded. As a result the state at 1949 keV is 14^+ ,

with the 1854 keV state having $J^\pi=13^{(+/-)}$ or 14^+ . Finally, the measured conversion coefficient for the 257 keV transition that decays from the 1.9 ns isomer at 2206 keV, is in agreement with a pure $E1$ assignment, as is the measured transition strength of 4.5×10^{-7} W.u.

3.4.2 States below the isomer at 4417 keV

The anisotropy for the 835 keV γ -ray indicates that the transition could be stretched $E2$, $M2$ or $E3$ or mixed $M1/E2$ or $E1/M2$, although the $M2$ and $E3$ possibilities can be rejected on the basis of transition strengths implied by the lifetime limit. This γ -ray competes with another branch consisting of a 505/330 keV cascade. The angular distribution coefficient for the 330 keV γ -ray, $-0.42(4)$, is consistent with a $J \rightarrow (J-1)$ dipole assignment while the conversion coefficient $0.40(9)$ suggests a mixed $M1/E2$ assignment. A mixing ratio of $-0.6(4)$ reproduces both measurements¹. The 505 keV transition has a large negative angular anisotropy, $A_2/A_0 = -0.69(4)$, suggesting a dipole/quadrupole assignment. The total conversion coefficient for the 330 keV transition measured in an out-of-beam gate on the 505 keV γ -ray is consistent with a mixed $M1/E2$ assignment. Hence the state at 3041 keV has $J^\pi = 17^-$. The 791 keV transition has an angular distribution consistent with stretched $E2$, $M2$ or $E3$ or mixed $M1/E2$ or $E1/M2$ assignments although again the $M2$ and $E3$ possibilities can be eliminated. Further coincidence relationships impose an $E2$ assignment.

The angular distribution for the 286 keV γ -ray parallel to the 791 keV transition is consistent with a dipole. The anisotropy for 317 keV ($A_2/A_0 = +0.34(3)$) indicates a stretched $E2$ assignment, as is confirmed by the total conversion coefficient value of $0.14(7)$. This results in $J^\pi = 19^-$ for the state at 3358 keV. The angular distributions for the 397 and 486 keV γ -rays, of $-0.28(3)$ and $-0.34(4)$ respectively, are consistent with stretched dipole assignments. The two γ -rays observed to decay from the isomer at 4417 keV, at 663.3 and 573.5 keV, have A_2/A_0 values, of $+0.41(6)$ and $+0.35(7)$ respectively, that both seem to agree with a stretched $E3$ assignment. However an $M2$ assignment, especially for the 573.5 keV γ -ray, cannot be totally eliminated², as will be discussed in more detail in Section 4.3.

¹Note that more accurate measurements of the mixing ratio require the measurement of the A_4 coefficient.

²Note that internal conversion coefficient measurements do not provide further definitive argument, see Appendix C.

3.4.3 States on the right hand side of the level scheme

Both the measured anisotropy and the total conversion coefficient for the 271 keV transition are in agreement with an $E1$ assignment, establishing a 10^- state. The 1176 keV γ -ray bypassing the isomer has an angular distribution consistent with stretched $E2$, $M2$ or $E3$ or mixed $M1/E2$ or $E1/M2$ assignments. Above the 12^- isomer, the three transitions at 280.4, 325.5 and 365.5 keV have angular distributions (see Table 3.3) that most likely support $M1$ assignments for these γ -rays, giving $J^\pi = 15^-$ for the state at 2989 keV.

CHAPTER 3. EXPERIMENTAL RESULTS

Chapter 4

The structure of ^{210}Fr

“C'est un plan pour construire un pédalo en forme de canard figure toi.”
– in **OSS117 - Rio ne répond plus.**

4.1 The nuclear shell model

The description of the structure of nuclei is a challenging task. Ideally, one may describe the motion of the constituents of the nucleus from the interaction of each nucleon with every other:

$$V_{nucleus} = \sum_{i,j,k} \langle i^k | V_k | j^k \rangle, \quad (4.1)$$

where i and j represent the nucleons and k the order of the many-body interaction (2-body, 3-body etc ...). Although somewhat successful for light nuclei, this no-core shell model approach is yet to produce detailed agreement, for masses higher than $A \sim 10$, mainly due to the prohibitive computational power that is required. It is, moreover, not clear whether the model will work because small problems will be magnified.

Fortunately, the (first order) inertness brought about by the closed-shell (magic) core within a nucleus has allowed for semi-empirical approaches to be developed. In the mass region where ^{210}Fr resides, the core is ^{208}Pb with 82 protons and 126 neutrons. The energy of the states observed in one nucleus is first anticipated as being a result of the motion of the valence nucleons in the nuclear potential. The energy of the states can consequently be expressed as a sum over the valence nucleons:

$$E = \sum_{ij} \langle i | V_{ij} | j \rangle + \sum_i \langle i | H_{0,i} | i \rangle, \quad (4.2)$$

where V_{ij} is the two-body residual interaction and $H_{0,i}$ describes the independent-particle motion of the i^{th} nucleon:

$$H_{0,i} = \frac{p_i^2}{2m} + V_1(r_i, p_i) + V_2(r_i, p_i) \underline{\sigma}_i \cdot \underline{\ell}_i, \quad (4.3)$$

V_1 is often taken as a Wood-Saxon potential, V_2 is an attractive potential and $\underline{\sigma}_i \cdot \underline{\ell}_i$ is the spin-orbit interaction that is required to reproduce the familiar magic shell gaps (see, for example, Ref. [Laws 80]).

4.1.1 Single particle potential and semi-empirical energies

Equation 4.3 shows that the single particle potential for a nucleon depends on its orbital angular momentum and hence the single particle potential is the same for all nucleons within a particular orbital. The corresponding bound energy level can be determined empirically from the mass excess of a nucleus with one particle or hole away from the core nucleus and with the nucleus lying in the relevant level. For example, the single particle potential for a proton in the $h_{9/2}$ orbital is:

$$\begin{aligned} \varepsilon_{h_{9/2}} &= \text{B.E.}(^{209}_{83}\text{Bi}_{126}) - \text{B.E.}(^{208}_{82}\text{Pb}_{126}) \\ &= -3.799\text{MeV}, \end{aligned} \quad (4.4)$$

since the $h_{9/2}$ level is the ground state in ^{209}Bi . Excited states in ^{209}Bi due to other proton orbitals are used to define their single particle energies (see Figure 4.1). The binding energies (B.E.) are taken from Ref. [Audi 03] and give the single particle energies in the Pb region, shown in Figure 4.1.

4.1.2 Two-body interactions

Recoupling two particles to different values of the total angular momentum results in a different energy. This adds to the energy of the core and therefore the energy from the coupling of those two nucleons is called an effective two body residual interaction. Such interactions can be determined from experimental values when they are available (see e.g. Bayer *et al.* [Baye 99]). In Figure 4.2 the sum of the two $h_{9/2}$ single particle energies is compared to the experimental energies for different angular momentum couplings in ^{210}Po in order to derive the residual interactions. Theoretical calculations are used where relevant experimental states are known (see for example Ref. [Kuo 71]). A comparison of those theoretical values with known experimental interaction energies shows differences up to several hundred keV (see Appendix E and Ref. [Baye 99]).

4.1. THE NUCLEAR SHELL MODEL

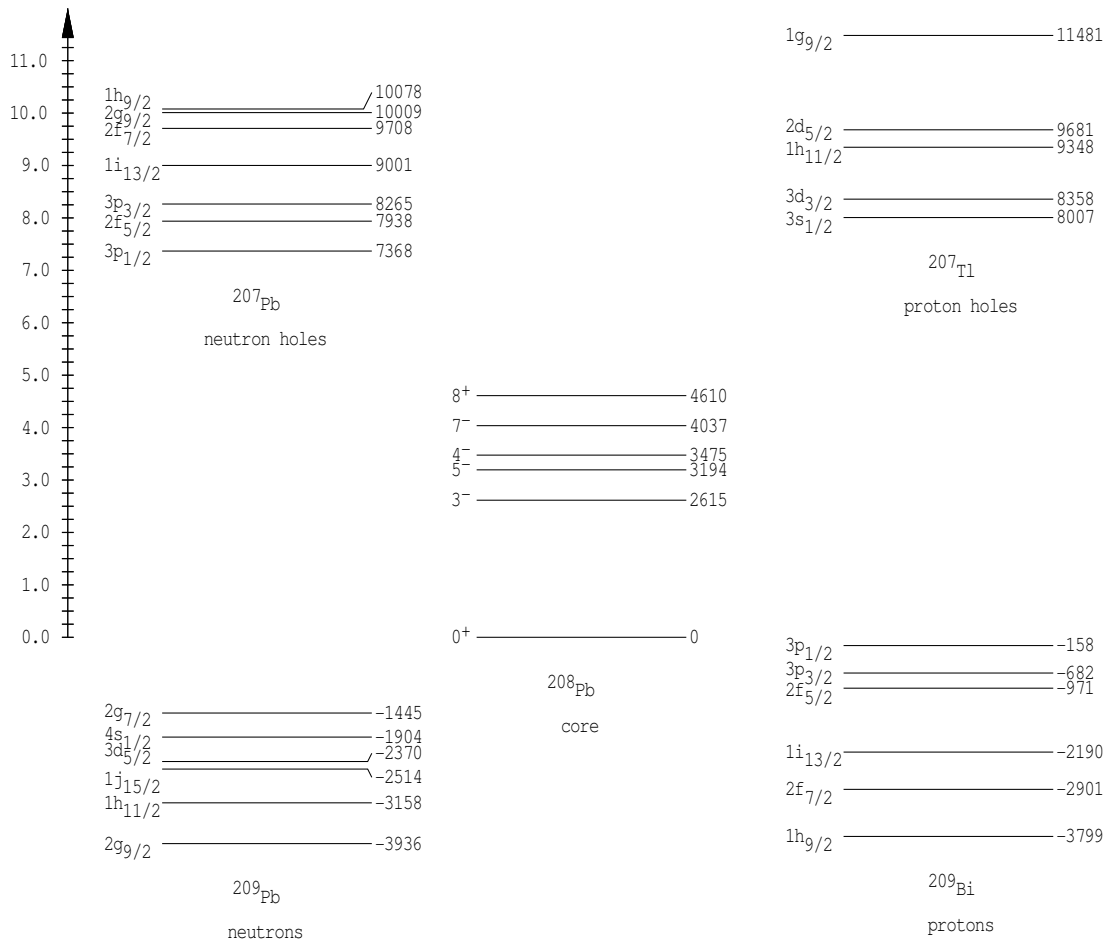


Figure 4.1: Experimental single particle energies for orbitals near the lead core (adapted from Ref. [Byrn 86a]).

It is important to note that these two body residual interactions contain the

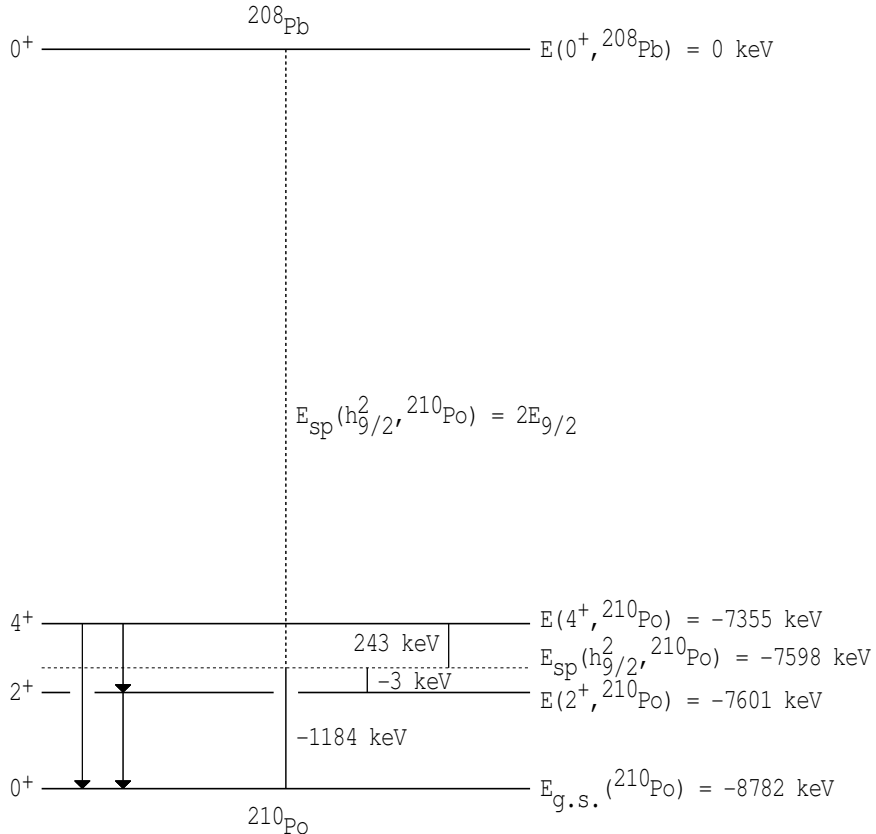


Figure 4.2: Determination of two body residual interaction for the 0^+ , 2^+ and 4^+ elements of the $(h_{9/2})^2$ multiplet. Solid arrows and levels represents experimental values. The dotted level is the ground state energy of ^{210}Po relative to the ^{208}Pb core, assuming that two non-interacting $h_{9/2}$ protons form the state. The experimental two-body interactions, shown in the picture, are: $\langle h_{9/2} | V | h_{9/2} \rangle_{0^+} = -1184 \text{ keV}$, $\langle h_{9/2} | V | h_{9/2} \rangle_{2^+} = -3 \text{ keV}$ and $\langle h_{9/2} | V | h_{9/2} \rangle_{4^+} = +243 \text{ keV}$. Note that the energies are not to scale.

effects of phenomena such as core polarisation, possible three-body interactions and even collective excitations, for example the effect of the coupling of the 3^- octupole phonon in ^{208}Pb will be contained in the relevant empirical two body residual interactions.

4.1. THE NUCLEAR SHELL MODEL

4.1.3 n -nucleon wave function and angular momentum re-coupling

For two nucleons coupled to angular momentum (I, M) (where $M = I_z$), the wave functions can be decomposed as a sum of the individual wave functions for the constituents of the system:

$$\Phi_{IM}(1, 2) = \frac{1}{\sqrt{2}} \sum_{m_1 m_2} \langle j_1 j_2 m_1 m_2 | IM \rangle \{ \phi_{j_1 m_1}(1) \phi_{j_2 m_2}(2) - \phi_{j_1 m_1}(2) \phi_{j_2 m_2}(1) \}, \quad (4.5)$$

where the $\langle j_1 j_2 m_1 m_2 | IM \rangle$ are the Clebsh-Gordan coefficients. This can be generalised for the n -nucleon wave function,

$$\Psi_{j^n v \alpha IM}(1 \dots n) = \sum_{J \beta v_1} \langle j^{(n-1)} v_1 \beta J, j | \{ j^n v \alpha J \} \times [\Psi_{j^{(n-1)} v_1 \beta J}(1 \dots (n-1)) \times \phi_j(1 \dots n)] , \quad (4.6)$$

where $\Psi_{j^n v \alpha IM}(1 \dots n)$ is normalised and totally antisymmetric upon the interchange of any two particles (see the case for $n = 2$ in Eq. 4.5), v is the seniority of the wave function¹, α (and β) contain all the quantum numbers required for the unique determination of the wave functions, I and J are the total angular momenta (of the n -nucleon and $(n-1)$ -nucleon wave functions) and M is the z -component. Finally, the $\langle j^{n-1} v_1 \beta J, j | \{ j^n v \alpha J \} \rangle$ terms are the so-called “coefficients of fractional parentage” (cfp) introduced by Racah [Raca 43, Laws 80]. Those coefficients have been tabulated by Bayman and Lande [Baym 66] and an explicit (recursive) formula was given by both Bayman and Lande [Baym 66] and Redmond [Redm 54]. The cfp’s ensure that the antisymmetry of the n th nucleon with the first $(n-1)$ nucleons is effective.

Macfarlane and French [Macf 60] have developed a very practical diagrammatic representation for Eq. 4.6:

$$\quad (4.7)$$

¹The seniority of a state is defined, following Racah’s definition [Raca 43], as “the number of unpaired nucleons in the eigenfunction describing the state”.

4.1.4 Calculation of states I - Empirical shell model calculation

The previous section has shown that it is possible to describe a state with n nucleons in terms of a sum over states with $(n - 1)$ nucleons. The $(n - 1)$ nucleon states can be further broken down so as to eventually express the wave function as a sum of two body wave functions. As a result, the energy of a state can be calculated through knowing all the two-body residual interactions like those shown in the previous section. Consider the configuration $[(j_1)_{J_1\beta_1}^{n_1} \otimes (j_2)_{J_2\beta_2}^{n_2}]_{I,M}$ (n_1 nucleons in the orbital j_1 and n_2 in j_2); the energy of the state from this configuration is due to three components [Laws 80]:

- the motion and interaction of the nucleons within the orbital j_1 (H_1),
- the motion and interaction of the nucleons within the orbital j_2 (H_2),
- the interaction between the nucleons in j_1 and those of j_2 (H_3).

The elements of the energy matrix can be obtained through²:

$$\langle [(j_1)_{J'_1\beta'_1}^{n'_1} \otimes (j_2)_{J'_2\beta'_2}^{n'_2}]_{I,M} | H_{(1+2)} + H_3 | [(j_1)_{J_1\beta_1}^{n_1} \otimes (j_2)_{J_2\beta_2}^{n_2}]_{I,M} \rangle. \quad (4.8)$$

From Eq. 4.6, H_1 and H_2 are a sum of the single particle energies ($n_1\varepsilon_1 + n_2\varepsilon_2$) and of the interaction energies for two nucleons on j_1 (or j_2) coupling to angular momentum J_1 , or J_2 (two-body matrix element for two nucleons in the same orbital), with the appropriate coefficient of fractional parentage due to the n_i -nucleon wave function partial decomposition³. The third Hamiltonian can also be developed using Eq. 4.6 (see Eq. 1.96 in Ref. [Laws 80]). An estimation of the contribution of H_3 to the total energy of a state for the case of the $29/2^+$ state in ^{213}Fr is shown in Appendix F.

Such a method is used in semi-empirical shell model program such as Sesame [Davi 05] to calculate the energy of excited states with respect to the Pb core.

This method has yielded calculated energies in very good agreement with experiment (see for example Ref. [Baye 01]) for nuclei with a few nucleons outside

²Note that the seniority of a state will be written as β in the following.

³Note that there are also Kronecker delta symbols to ensure that the quantum numbers in the bra and ket are equal. For example consider the interaction of three protons in the $h_{9/2}$ orbital with angular momentum $J = 17/2$. The interaction of the three protons on this orbital is calculated for any combination that gives this angular momentum, e.g. $(9/2, 5/2, 3/2)$ and $(9/2, 7/2, 1/2)$ for the bra and the ket, respectively. The seniority must also be the same. For example for those three protons the matrix element for $J = 9/2$ is zero if the members of the multiplet are $(9/2, 1/2, -1/2)$ (seniority 1) and $(5/2, 3/2, 1/2)$ (seniority 3) but is not always zero for $(5/2, 3/2, 1/2)$ (seniority 3) and $(7/2, 3/2, -1/2)$ (seniority 3).

4.2. PRELIMINARY CONSIDERATIONS FOR CONFIGURATION ASSIGNMENTS IN ^{210}Fr

the lead core. The inclusion of additional valence particles/holes in the system results in progressively poorer agreement. One of the reasons is that mixing of different configurations (see below) increases with nucleon number. It can also be noted that while empirical two-body interactions can contain effects of higher order nucleon-nucleon interactions, these elements are incorporated using a method that considers the interaction as being of 2-body type.

4.1.5 Calculation of states II - Partial decomposition

A more direct approach to the calculation of state energies is to decompose the wave function for a state as a sum of other wave functions for which equivalent states, and hence empirical interactions, are known. Consider the configuration $[\pi(j_1^2 j_2)_I \otimes \nu(j_3^2)_{0+}]$. This can be decomposed as:

$$\begin{aligned} \langle \pi[(j_1^2)_{I_1} (j_2)_{I_2}]_I \otimes \nu(j_3^2)_{0+} \rangle_I &= \langle \pi j_1^2 j_2^1 \rangle_I + \langle \pi j_1^2 \otimes \nu(j_3^2)_{0+} \rangle_{I_1} \\ &\quad + \langle \nu j_3^2 \rangle_{0+} + \langle \pi j_2^1 \otimes \nu(j_3^2)_{0+} \rangle_{I_2} \end{aligned}$$

Hence the energy for the configuration on the left hand side can be calculated if all of the terms on the right hand side are known as well. As example, a calculation for the state at 3327 keV in ^{210}Fr with $J^\pi = 19^-$ is shown in Appendix D (see also Refs. [Pole 85, Blom 83]).

4.2 Preliminary considerations for configuration assignments in ^{210}Fr

In this section, calculations from a semi-empirical shell model program for different francium and lead nuclei are presented and discussed. These calculations can provide agreement to within tens of keV for nuclei with only a few particles outside the lead core. They are, however, expected to be significantly less definitive for the assignment of configurations in nuclei with many valence nucleons (particles or holes), eight in the case of ^{210}Fr , mainly due to the presence of configuration admixtures that are ignored in the empirical calculation because of the computational power required for a proper treatment. This can be an issue for configuration assignments, in particular if a number of pure configurations are energetically competitive then the mixed configuration states are split further apart and the lowest state arising from that mixing can lie much lower in energy.

The first major contribution to the structure comes from the motion of protons and neutrons independent from one another. Since ^{210}Fr has 123 neutrons

and 87 protons, some guidance to the behaviour can be obtained from looking at ^{205}Pb , with three neutron-holes, and ^{213}Fr , with five valence protons. Further, more precise guidance can be found by studying the competition between proton and neutron excitations in other Fr nuclei, in particular ^{211}Fr and ^{212}Fr . ^{212}Fr is similar to ^{210}Fr but simpler in having two fewer neutron-holes, although differences are expected due to the odd neutron-hole occupying a different shell in ^{212}Fr ($p_{1/2}$) compared to ^{210}Fr ($f_{5/2}$).

As a first step, the agreement between calculations and observations in these previously studied nuclei is investigated prior to attempting to understand ^{210}Fr . There is no intention to assign configurations to the measured levels in those nuclei, only the general behaviour and agreement are discussed. Note that in any case the previous work on these nuclei has already assigned configurations. Details for $^{211,212,213}\text{Fr}$ (see Byrne *et al.* [Byrn 86b, Byrn 86a]), ^{209}Fr (see Dracoulis *et al.* [Drac 09a]) and ^{205}Pb (see Lindén *et al.* [Lind 76] and [Pole 94]) are already published.

The calculations in the following sections have been performed anew with Sesame, so as to obtain results up to date with the most recent observations (and estimates) of two-body residual interactions used in the calculations. The elements used in this work are shown in more detail in Appendix E.

4.2.1 Neutron configurations - ^{205}Pb

From the calculations performed as part of this work, and shown in Figure 4.3, it seems that mixing is not so prevalent in ^{205}Pb since the states are generally well reproduced (for experimental states see Refs. [Lind 76, Pole 94]), with the exception of the lowest energy $5/2^-$ and $7/2^-$ states. These discrepancies probably result from the neglect of pairing interactions. This is consistent with the fact that the calculated $5/2^-$ and $7/2^-$ states (from $\nu(p_{1/2}^{-2}f_{5/2}^{-1})$ and $\nu(p_{1/2}^{-1}f_{5/2}^{-2})$, respectively) agree with the experimental energy difference for those states (~ 700 keV). Much better agreement is found at higher spin with states up to $25/2^-$ calculated within a maximal energy difference of some tens of keV. A notable exception to the detailed agreement is the $9/2^-$ state at 987 keV that is not reproduced by any state from the $\nu(p_{1/2}^{-1}f_{5/2}^{-2})$ or $\nu(f_{5/2}^{-3})$ multiplets.

4.2.2 Proton configurations - ^{213}Fr and ^{211}Fr

The proton core for ^{210}Fr is ^{213}Fr . The new calculation done as part of this study (see Figure 4.4) shows that the ground state energy is overestimated, which is probably another indication of the necessity for the pairing interaction to be in-

4.2. PRELIMINARY CONSIDERATIONS FOR CONFIGURATION ASSIGNMENTS IN ^{210}FR

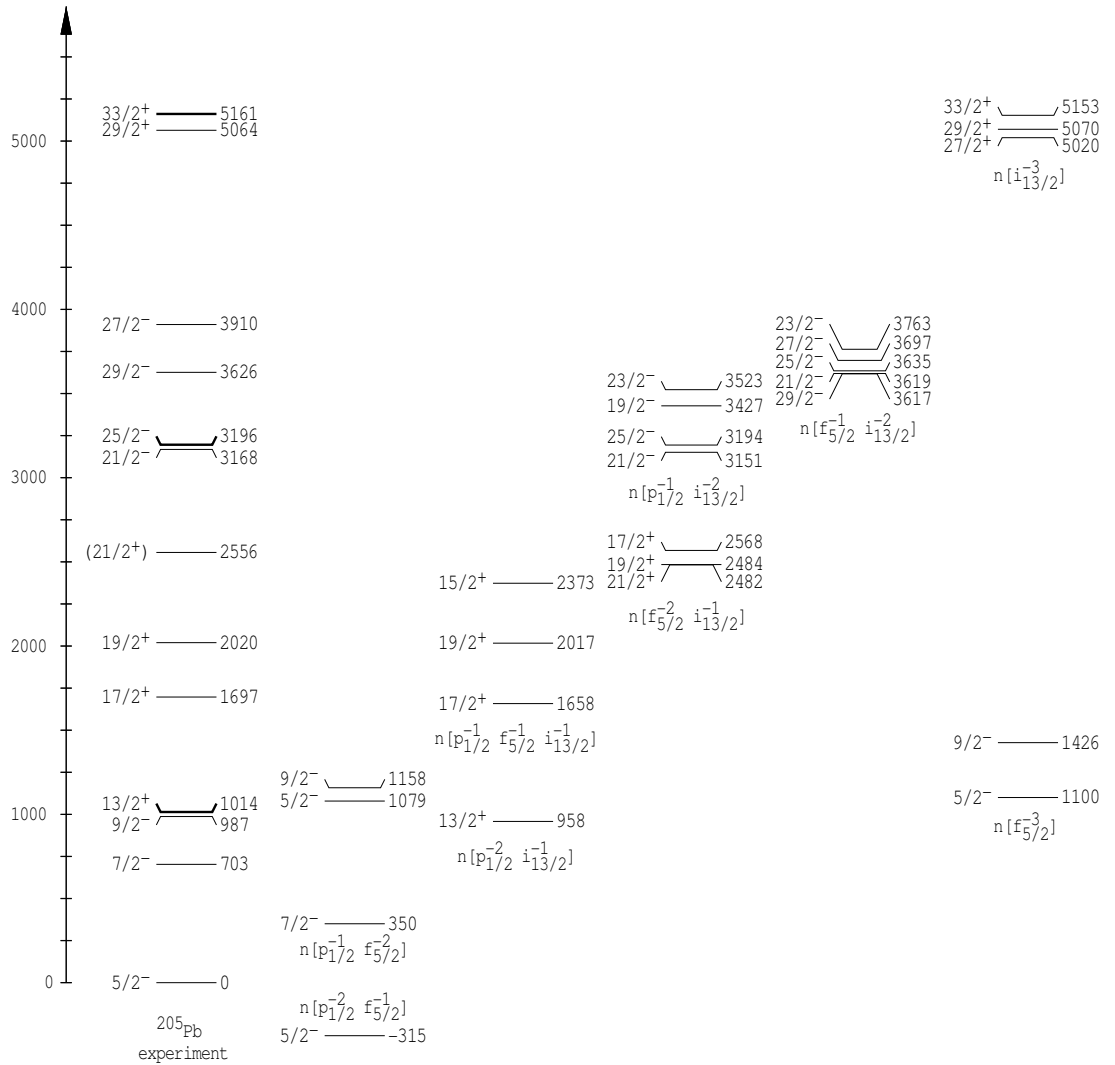


Figure 4.3: Comparison between the calculated and experimentally measured levels in ^{205}Pb . Bold experimental levels represent isomers; in the figure, the Roman letters “p” and “n” are used to describe protons and neutrons, respectively, whereas the Greek letters “ π ” and “ ν ” are used in the text. Note that this will be consistently used in the following figures.

cluded. The reproduction of states in this nucleus is not as good as what has been found in nuclei such as ^{211}At (see Bayer *et al.* [Baye 99]). For example, the first excited state at 1189 keV ($J^\pi = 13/2^-$) is calculated 135 keV above the $13/2^-$ member of the $\pi h_{9/2}^5$ multiplet and 625 keV above the $13/2^-$ member of $\pi(h_{9/2}^4 f_{7/2})$ multiplet. If these configurations are, nevertheless, mixed, the $11/2^-$ and $13/2^-$ states will have different energies. A lowering of both states can be anticipated, and this could result in the mixed $13/2^-$ state lying below the (non-observed) $11/2^-$ state, that the calculation predicts at lower energies than the $13/2^-$ in each multiplet. Similar observations can be made for the negative parity states throughout the level structure of ^{213}Fr , with this suggesting a mixing of the $\pi h_{9/2}^5$ and $\pi(h_{9/2}^4 f_{7/2})$ configurations. Positive parity states are generally in better agreement, and this is consistent with the fact that there are fewer multiplets available for mixing to occur.

The energy spectrum for ^{211}Fr was also calculated with two neutron-holes in the $p_{1/2}$ orbital, see Figure 4.5. These neutron-holes are mostly inert and hence ^{211}Fr should be similar to ^{213}Fr .

The first excited states are not very well reproduced. Similar to ^{211}Fr , mixing of the $\pi h_{9/2}^5$ and $\pi(h_{9/2}^4 f_{7/2})$ configurations is expected, although in this (experimental) case, it is the $11/2^-$ state that is energetically favoured over the $13/2^-$ state. Interestingly, some levels are calculated lower than they are measured. Again, if the multiplets are mixed then some members might not be fed preferably if they slip under low spin levels. For example a mixed $21/2^-$ state might be energetically favoured over a $17/2^-$ level, however if only a $13/2^-$ state is available for the decay then the $17/2^-$ will be observed. As for ^{213}Fr , positive parity states, especially those arising from the $\pi(h_{9/2}^3 i_{13/2} f_{7/2})$ and the $\pi(h_{9/2}^3 i_{13/2}^2)$ multiplets, tend to be very well reproduced by the calculation.

For the interest of the reader the calculation for ^{209}Fr , for which the agreement is very degraded, is shown in Figure 4.6.

Observation of mixing in Rn isotopes, and explicit consideration of octupole coupling

The explicit inclusion of octupole vibration in the calculation of excited states, such as explained by Poletti *et al.* [Pole 86], has been shown to help assigning configurations to observed states in radon isotopes. Several effects described by Poletti *et al.* are expected to have effects on the interpretation of states in ^{210}Fr , which, unfortunately have not been calculated here. At first sight, coupling of the 3^- vibration will result, as explained in the introduction, in admixtures of pure configurations and coupling with the octupole state, in particular for the $\pi i_{13/2}$,

4.2. PRELIMINARY CONSIDERATIONS FOR CONFIGURATION ASSIGNMENTS IN ^{210}Fr

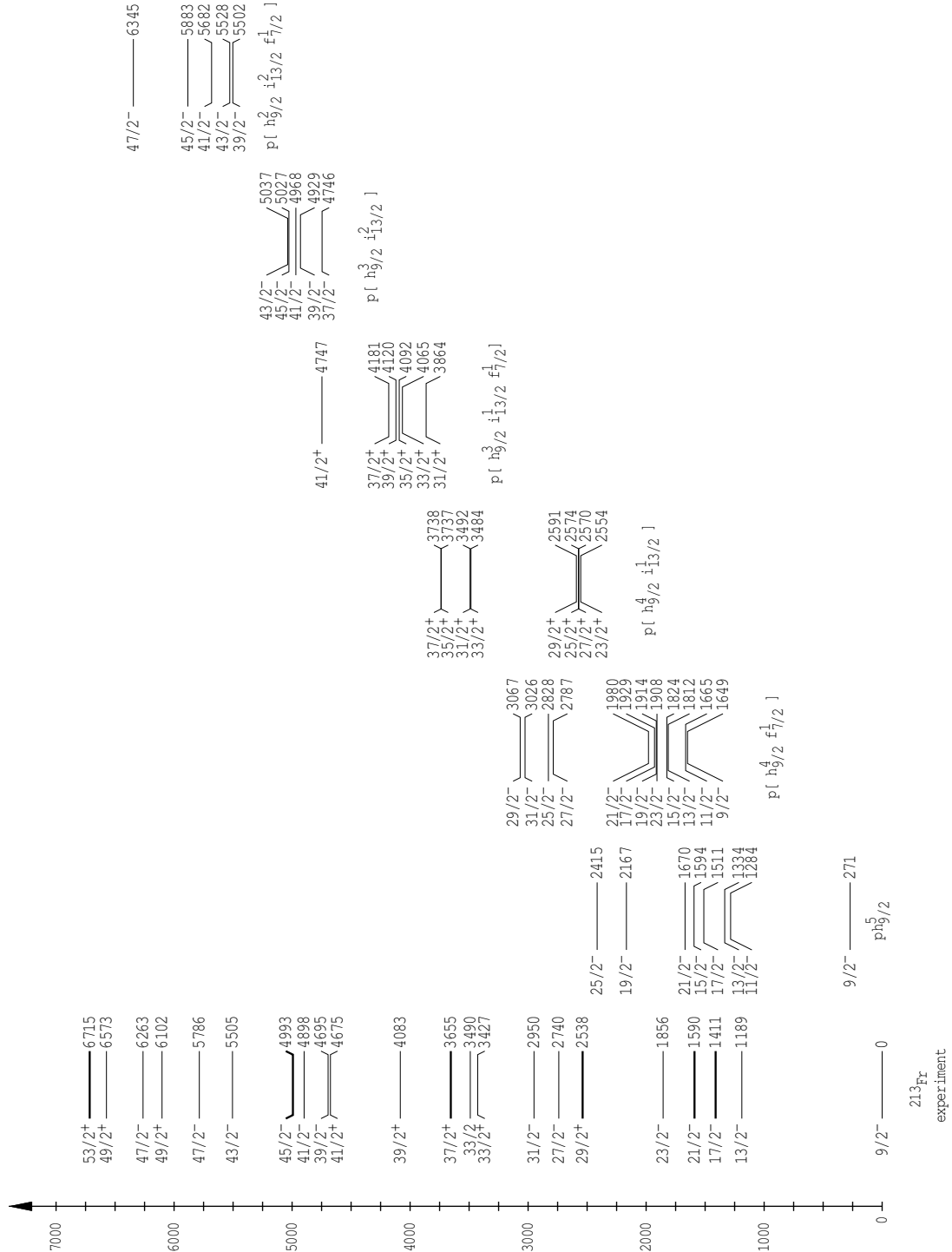


Figure 4.4: Comparison between the calculated and experimentally measured levels in ^{213}Fr .

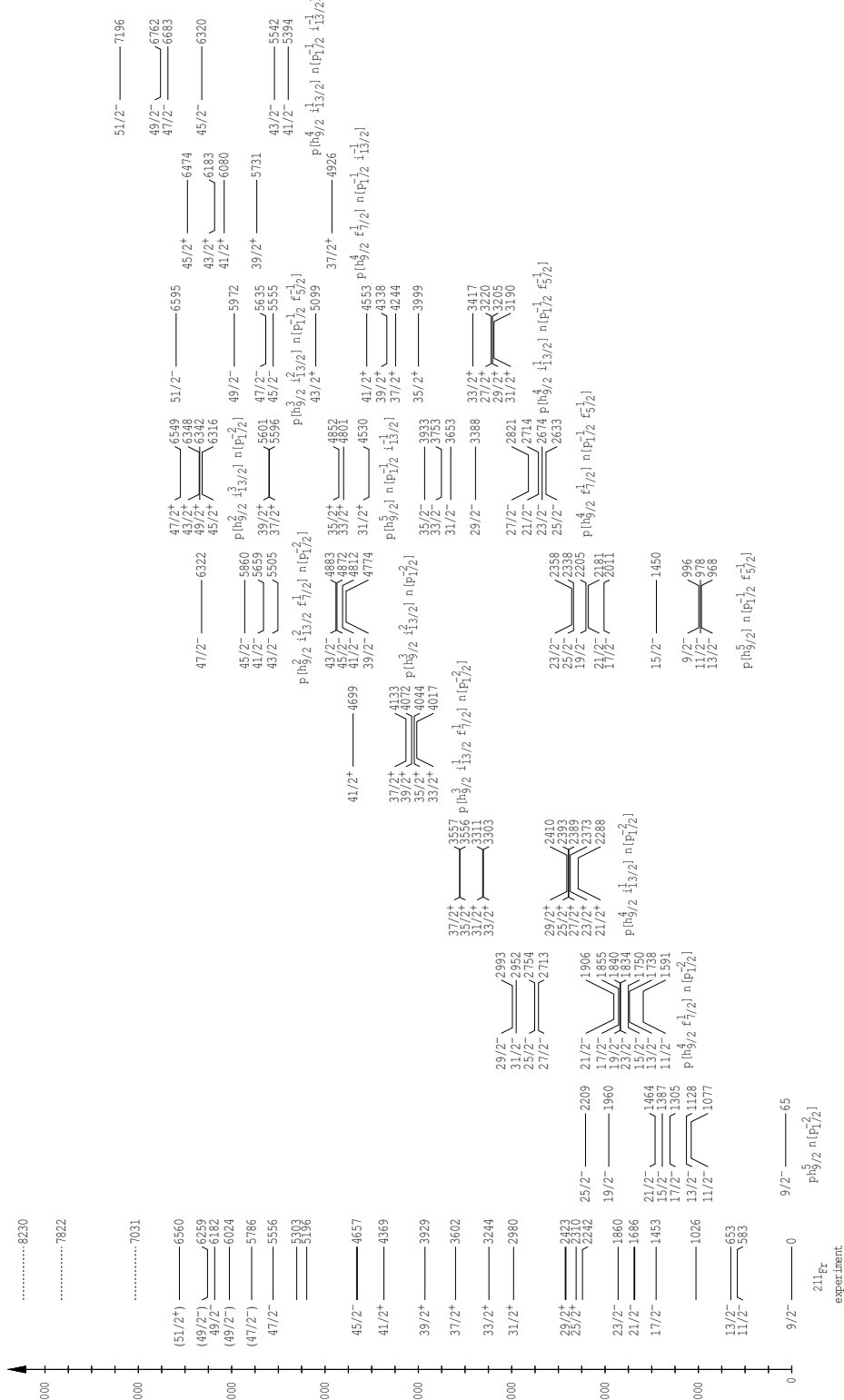


Figure 4.5: Comparison between the calculated and experimentally measured levels in ^{211}Fr .

4.2. PRELIMINARY CONSIDERATIONS FOR CONFIGURATION ASSIGNMENTS IN ^{210}Fr

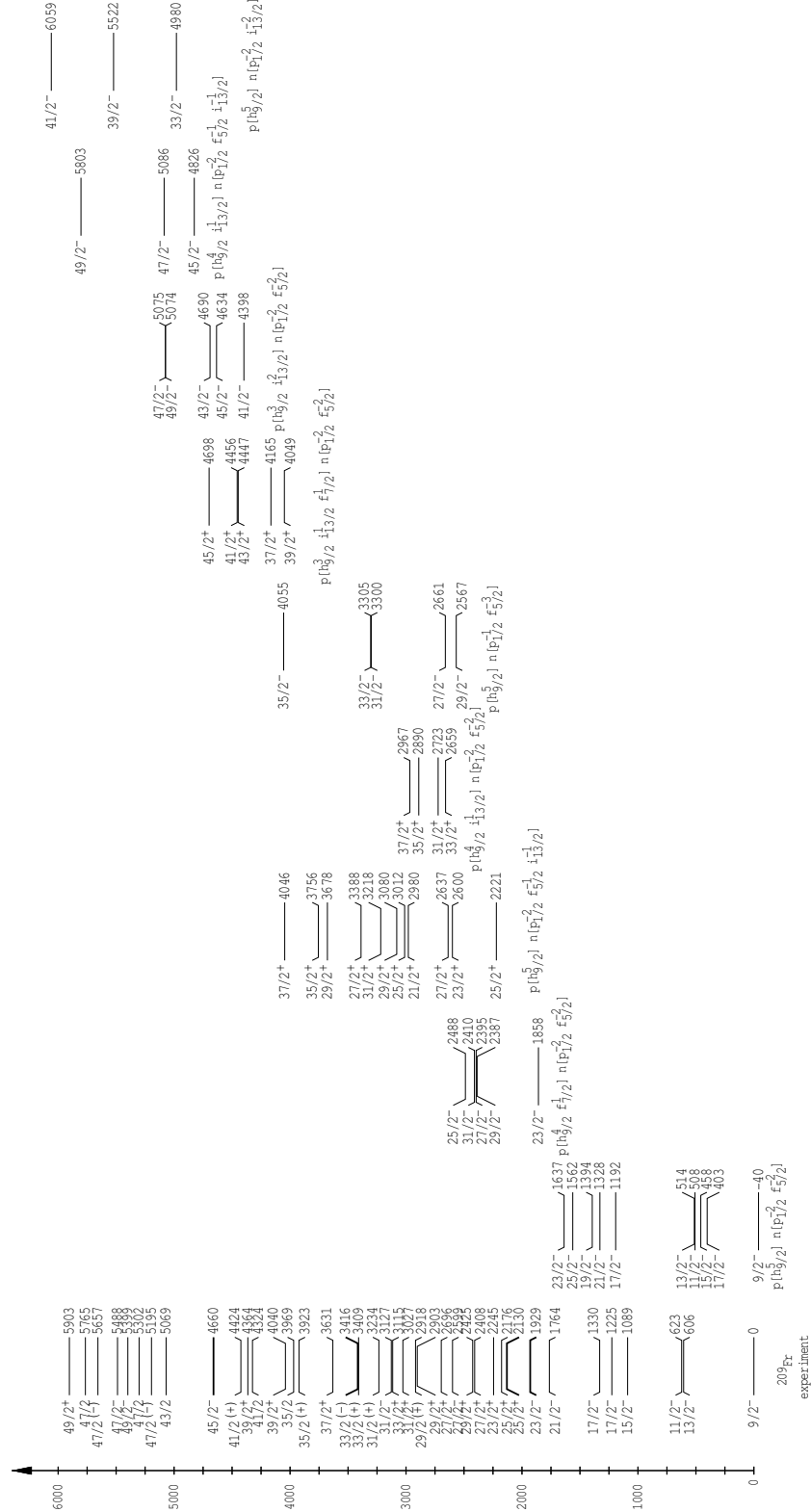


Figure 4.6: Comparison between the calculated and experimentally measured levels in ^{209}Fr .

$\pi f_{7/2}$, $\nu g_{9/2}$ and $\nu j_{15/2}$ levels. However, the 3^- coupling allows for increased admixture of other configurations. This, for example, has a strong effect for the assignment of the configuration of the 20^+ level in the neutron closed shell nucleus ^{212}Rn , that, while mainly from the $\pi h_{9/2}^2 i_{13/2}^2$ coupling, is actually not pure and contains admixtures of $\pi h_{9/2}^3 i_{13/2} \otimes 3^-$, $\pi h_{9/2}^2 i_{13/2} f_{7/2} \otimes 3^-$, $\pi h_{9/2}^2 f_{7/2}^2 \otimes 3^-$, etc. (see Ref. [Pole 86]). In this case the calculated transition strength, for the $E3$ decay to the 17^- state (also containing an admixture of a range of configurations), for nominal configurations is two and a half times lower than that for particle-vibration mixed configurations. Including octupole effects the agreement is brought from very doubtful to very good. Another effect is due to Pauli blocking, leading to underestimation of the energy of the states where a fully aligned proton or neutron in one of the $\pi i_{13/2}$, $\pi f_{7/2}$, $\nu g_{9/2}$ or $\nu j_{15/2}$ is required. Since the 3^- octupole vibration is due to collective motion of many particles it involves numerous transitions behaving coherently such as $\pi i_{13/2} \rightarrow f_{7/2}$, where fully aligned angular momentum are required. Hence, if in any state a fully aligned configuration is required it would *de facto* block the associated component of the collective 3^- state. Yet this is probably not going to affect the assignments for the case of ^{210}Fr , since, as often stressed in this thesis, full angular momentum alignment of proton and neutron-holes is not favoured which means that it is not expected that components of the octupole vibration will be Pauli blocked.

Comprehensive calculation of mixed waved function for even-parity states in ^{210}Rn , which do not contain a coupling with the 3^- state, have also been conducted by Poletti *et al.* [Pole 82], and result in a range of admixtures identified. This was not calculated in the case of ^{210}Fr , however it is obvious from this calculation in ^{210}Rn that this will penalise the agreement in the present case.

4.2.3 The case of ^{212}Fr

In the same way that ^{213}Fr and ^{211}Fr are related, the odd-odd Fr isotopes are also expected to show similarities. ^{212}Fr is, with one neutron hole, an intermediate case in developing our understanding before reaching ^{210}Fr . Figure 4.7 presents the semi-empirical calculation for ^{212}Fr .

In ^{212}Fr , states up to $25\hbar$ are almost uniquely due to valence nucleon excitations while the isomer at 5854 keV with $J^\pi = 27^-$ is due to a neutron core excitation. At low spin, the 5^+ ground state and 7^+ first excited states are both poorly reproduced, similar to the ^{213}Fr case, although the energy difference is lower (179 versus 271 keV). Note that these differences are similar to the case for ^{205}Pb in which the ground state was not very well reproduced by the calculation. A probable explanation could also be related to mixing of the relevant members

4.2. PRELIMINARY CONSIDERATIONS FOR CONFIGURATION ASSIGNMENTS IN ^{210}Fr

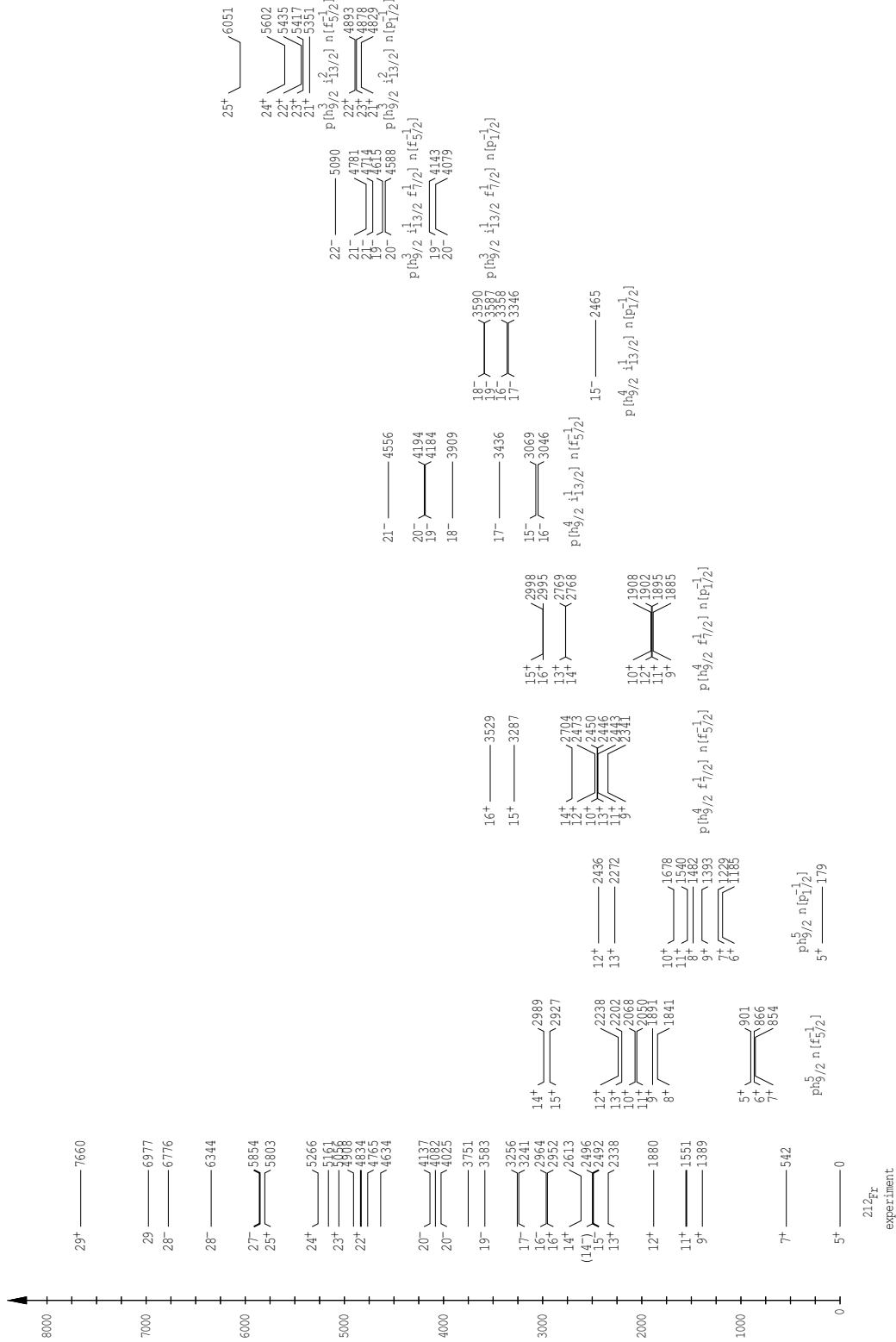


Figure 4.7: Comparison between the calculated and experimentally measured levels in ^{212}Fr .

of the $\pi h_{9/2}^5 \otimes \nu f_{5/2}^{-1}$ and $\pi h_{9/2}^5 \otimes \nu p_{1/2}^{-1}$ multiplets.

The calculation for the $\pi h_{9/2}^5 \nu p_{1/2}^{-1}$ configurations is in very good agreement with the observed 9^+ and 11^+ states. The isomeric nature of the 11^+ state is due to the relatively low energy $E2$ decay, rather than to a configuration change or other structural reason. The next two states, 12^+ and 13^+ , are reproduced by members of the $\pi(h_{9/2}^4 f_{7/2}) \otimes \nu p_{1/2}^{-1}$ and $\pi h_{9/2}^5 \otimes \nu p_{1/2}^{-1}$ multiplets, respectively.

The 15^- isomeric state most likely belongs to the $\pi(h_{9/2}^4 i_{13/2}) \otimes \nu f_{5/2}^{-1}$ configuration. Note that the decay proceeds through a favoured $\pi \tilde{i}_{13/2} \rightarrow \tilde{f}_{7/2}$ $E3$ γ -ray, having a transition strength of $22(1)$ W.u., and a 154 keV $M2$ transition that would feed the experimentally measured 13^+ state is not observed, but this is due to the very weak branching ratio considering the usual strength for a $M2$ transition ($\approx 10^{-2}$ W.u.). All the negative parity states leading up to $J^\pi = 21^-$ are well reproduced by the $h_{9/2}^4 i_{13/2}$ proton configuration, coupled to either the $p_{1/2}^{-1}$ or the $f_{5/2}^{-1}$ neutron-hole.

Finally, the 4834 keV isomer with $J^\pi = 22^+$ can be attributed to the $[\pi(h_{9/2}^3 i_{13/2}^2) \otimes \nu p_{1/2}^{-1}]_{22^+}$ coupling. While an enhanced $E3$ could be expected to feed the 19^- state⁴, the presence of a 21^- state means that the $E1$ decay to this state is instead favoured.

4.3 Configuration assignments in ^{210}Fr

This section presents specific calculations for ^{210}Fr (see Figure 4.8) and features a discussion of how they compare to the experimental observations previously reported in Chapter 3.

The level scheme for ^{210}Fr (see Figure 3.9) is more fragmented at low spin than any of the heavier neutron-deficient francium isotopes discussed in the previous sections. The case of ^{209}Fr is similar, although not to the same degree. Hence the conclusions for neighbouring isotopes carry on to ^{210}Fr in a more pronounced way. For example, the 6^+ ground state and 7^+ first excited states are poorly reproduced by the calculation. The discrepancy between experiment and calculation is very similar to that observed in ^{205}Pb (≈ -330 keV) and contrasts with the overestimation in ^{212}Fr . The lowering of the 9^+ energy means that the 11^+ state which decays to the 9^+ by the 721 keV transition, is not an isomer although it is in ^{212}Fr . Nevertheless, the positive parity states up to 10^+ are all likely to mainly arise from the $\pi h_{9/2}^5 \otimes \nu(p_{1/2}^{-2} f_{5/2}^{-1})$ multiplet with the energy difference between calculation and experiment consistently around 350 keV. The reason why several

⁴The 19^- state configuration is $\pi(h_{9/2}^4 i_{13/2}) \nu p_{1/2}^{-1}$, which would make the $\tilde{i}_{13/2} \rightarrow \tilde{h}_{9/2}$ enhanced $E3$ possible.

4.3. CONFIGURATION ASSIGNMENTS IN ^{210}Fr

states are, however, predicted to be quite different in energy to that experimentally observed (see for example the 11^+ state predicted at 851 keV in Figure 4.8) is not clear, however it can be noted that there are several other multiplets that could participate in some configurations, and mixing may be involved.

States with spins from 11^+ to 14^+ cannot be attributed to a single configuration. However, it may be noteworthy that the $12^+ \rightarrow 10^+$, 289 keV transition in ^{210}Fr has a similar strength to the $21/2^- \rightarrow 17/2^-$, 233 keV transition in ^{211}Fr . This is likely to include a similar structural change between the two states since these two pairs of states, can be linked by the addition of a partially aligned neutron-hole in the $f_{5/2}$ orbital (partially aligned due to the repulsive nature of the proton neutron-hole interaction for full alignment). The 15^- to 12^+ energy gap in ^{210}Fr is similar to that in ^{212}Fr (580 keV compared to 612 keV), however, unlike ^{212}Fr , the isomer decays by a $E1$ transition due to the much lower energy of the 14^+ state in ^{210}Fr , thus favouring the $E1$ branch over the possible $E3$ transition. The 15^- isomer is probably a member of the $\pi(h_{9/2}^4 i_{13/2}) \otimes \nu(p_{1/2}^{-2} f_{5/2}^{-1})$ multiplet. In both this and the ^{212}Fr case, the 16^- state from this multiplet is calculated slightly lower (23 keV in both cases) than the 15^- state which is a probable indication of the level of uncertainty in the calculation within a multiplet. In the case that the experimental state is 15^- , then the calculation suggest a rather low energy $E1$ transition. Such transition have been measured with strength of 10^{-6} to 10^{-7} W.u. in other francium isotopes, and this would imply a lifetime in the nanoseconds range for the 257 keV γ -ray observed here. This is consistent with the presence of a 1.9 ns meanlife and the measured strength of the 257 keV transition, $\approx 9 \times 10^{-6}$ W.u. (see Table 3.5).

The ground state

In making spin and parity assignments in ^{210}Fr (see Section 3.4), the starting point was that the ground state has $J^\pi = 6^+$. This was directly measured by Ekström *et al.* (see Ref. [Ekst 78]). In the present work this cannot be directly confirmed. The observation of a 25 keV transition feeding the ground state, however, agrees very well with such an assignment when compared with semi-empirical calculations that predict the 6^+ and 7^+ to be very close in energy. In Figure 4.9, the lowest levels calculated for different spin members of the multiplet from which the ground state arises is presented. While the (lowest) 7^+ member is calculated below the (lowest) 6^+ member, it can be noted that the small difference is within the level of uncertainty observed in the calculations.

CHAPTER 4. THE STRUCTURE OF ^{210}Fr

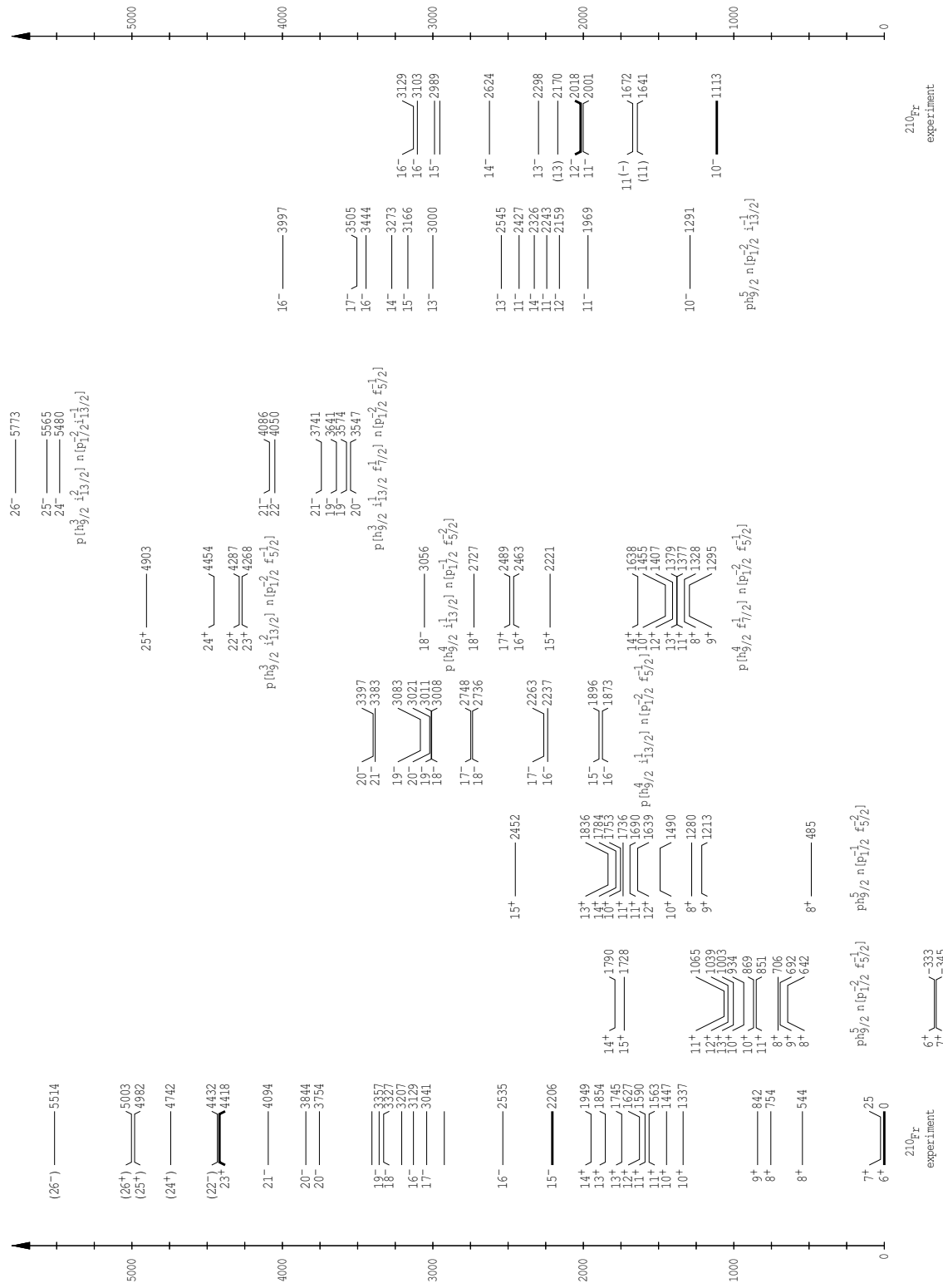


Figure 4.8: Comparison between the calculated and experimentally measured levels in ^{210}Fr . Experimental states are split left and right similarly to the level scheme, see Figure 3.9.

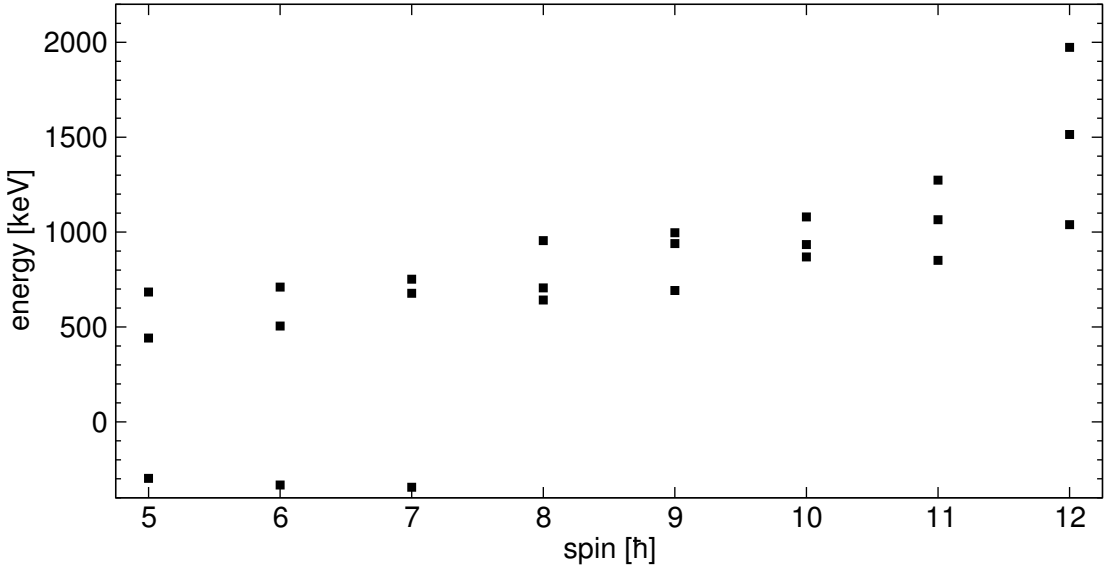


Figure 4.9: Lowest levels calculated for the $\pi(h_{9/2}^5) \nu(p_{1/2}^{-2}f_{5/2}^{-1})$ configuration for angular momenta between 5^+ and 12^+ . The lowest 5^+ , 6^+ and 7^+ are calculated at -298 , -330 , -315 keV, respectively.

The 10^- isomer

The 10^- isomer at 1113 keV in ^{210}Fr decays via an $E1$ transition and is almost certainly from the $\pi(h_{9/2}^5)_{9/2} \otimes \nu(j^{-2})_{0+} i_{13/2}^{-1}$ configuration. The observed hindrance of 2×10^6 is consistent with typical $E1$ transition strengths observed in the lead region, and it is also similar to what has been observed in other odd-odd nuclei in this region (see Ref. [Lonn 88], Table 4.1 and Figure 4.10). This implies that the 9^+ state should be from the $\pi(h_{9/2}^5) \otimes \nu(p_{1/2}^{-2}f_{5/2}^{-1})$ or $\pi(h_{9/2}^4 f_{7/2}) \otimes \nu(p_{1/2}^{-2}f_{5/2}^{-1})$ configurations (or an admixture). Consequently, the difference in angular momentum between the parent and daughter states is bigger than the angular momentum carried by the $E1$ γ -ray (hence j -forbidden) and this explains some of the hindrance observed. The energy of the isomer is related to the $i_{13/2}$ neutron hole energy in odd Pb isotopes (note that a $13/2^+$ isomer is observed in neutron-deficient odd-even nuclei in the Pb region) that falls with neutron number quite rapidly, while the 9^+ state energy depends on details of the proton-excitation since the neutrons are still in the ground state configuration. This is shown in Figure 4.11 and Table 4.2. As one moves to more neutron-deficient isotopes, the energy of the 10^- isomer can potentially fall lower below the 9^+ state so that it can only decay via an $E3$ transition. Such an $E3$ was first observed in ^{208}Bi [Boni 68], however if the 10^- state stays close to, but above, the 9^+ state then one may expect both $E1$ and $E3$ decays to proceed. This is observed in ^{204}Bi and ^{206}Bi but a very weak

$E3$ γ -ray⁵ has also been observed in ^{208}At by Fant *et al.* [Fant 84]. The latter observation is relatively unexpected since the $E3$ transitions are not observed in ^{206}At or ^{208}Fr , where the energy of the $E1$ is much lower than and similar to, respectively, that observed in ^{208}At .

In ^{210}Fr the energy gap between the 10^- state at 1113 keV and the 7^+ state at 25 keV means that the $E3$ transition will not be observed due to the (expected) very weak branching ratio. Note that if the strength of the $E3$ transitions evolve similarly to that for the $E1$ γ -rays in between ^{208}At and ^{210}Fr , and if the $E3$ transition is effectively observed in ^{208}At , then we can expect that transition to be twice as weak in ^{210}Fr . That means that the prompt intensity for the $E3$ transition would be 1 in the units of Table 3.3, too low to be observed in any of the present experiments.

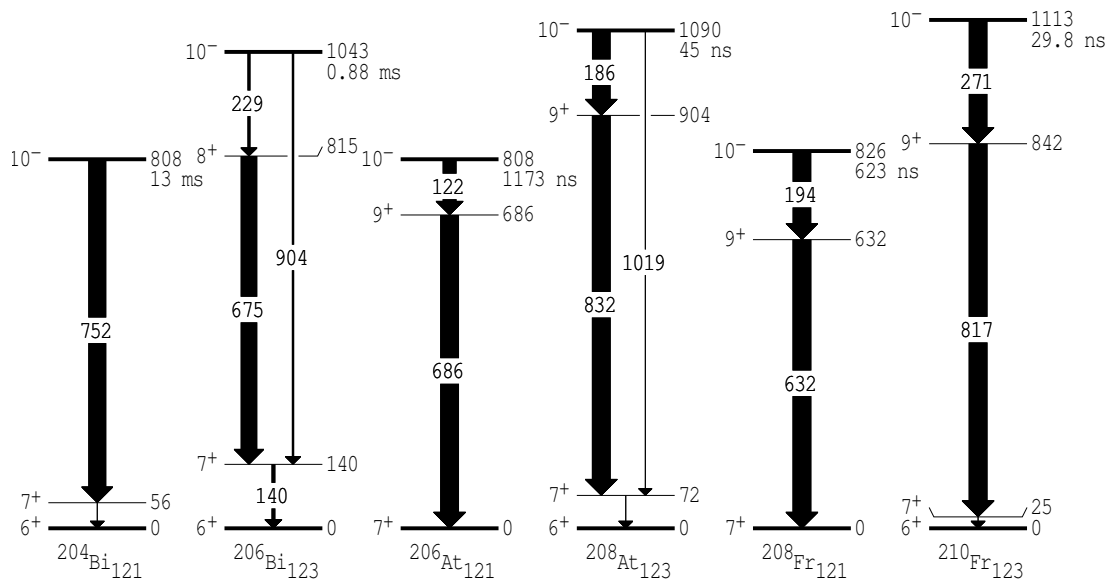


Figure 4.10: Comparison of the decay of the 10^- isomer for selected odd-odd nuclei near ^{208}Pb .

⁵Note that the energy reported by Fant *et al.* [Fant 84] is incorrect and it seems that this carries on to their strength evaluation. The strength was determined here by taking the correct energy and the calculated internal conversion coefficient. Conversion coefficient measurements were conducted by Fant *et al.* but they do not report experimental values for either the 187 keV $E1$ transition or the 1019 keV (actually 1019 keV) $E3$ transition. For a 1119 keV pure $E3$ transition a strength of $113 e^2\text{fm}^6$ is determined here compared to the value of $170 e^2\text{fm}^6$ reported by Fant *et al.* For the (correct energy) 1019 keV pure $E3$ γ -ray we calculate $215 e^2\text{fm}^6$.

Table 4.1: Transition strengths for decays from 10^- isomers in odd-odd bismuth, astatine and francium nuclei.^(a)

Nucleus	Initial state, τ	Final state J^π	E_γ (keV)	I_γ	$\sigma\lambda$	α_T^b	Transition strength (W.u.)
^{204}Bi	808 keV, 13 ms	7^+	752	100	$E3$	0.0326	3.87×10^{-4}
^{206}Bi	1043 keV, 0.88 ms	7^+	904	60	$E3$	0.0207	1.97×10^{-4}
		8^+	229	80	$M2$	4.26	3.85×10^{-4}
^{206}At	808 keV, 1173 ns	7^+	122	100	$E1$	0.282	1.03×10^{-7}
^{208}At	1090 keV, 45 ns	7^+	1019	0.7	$E3$	0.0175	8.40×10^{-2}
		9^+	187	100	$E1$	0.0990	8.53×10^{-7}
^{208}Fr	826 keV, 623 ns	9^+	194	100	$E1$	0.0947	5.56×10^{-8}
^{210}Fr	1113 keV, 29.8 ns	9^+	271	100	$E1$	0.0431	4.49×10^{-7}

^(a) The relevant references are given in Table 4.2.^(b) Values taken from Ref. [Kibe 08].

Table 4.2: Meanlife, energy and mode of decay for the 10^- isomers in a range of bismuth, astatine and francium nuclei. The equivalent isomer in the lead isotopes is $13/2^+$ and is related to the 10^- isomer by the addition of the $f_{5/2}^{-1}$ neutron-hole.

N	^{115}Bi	^{117}Bi	^{119}Pb	^{199}Pb	^{201}Pb	^{203}Pb	^{205}Pb
τ	$42.9(9)$ min	$12.2(3)$ min	$60.8(18)$ s	$6.21(11)$ s	$5.6(2)$ ms		
E (keV)	319	$425+\Delta$	629	825	1014		
Decay	$M4 + \beta^+$	$M4 + \beta^+$	$M4$	$M4$	$M2/E3/M4$		
Refs.	[Rapa 79, Ande 57, Hick 80]	[Ande 55]	[Fisc 55, Stoc 56, Bara 52]	(a)	[Maie 71]		
N	^{198}Bi	^{200}Bi	^{202}Bi	^{204}Bi	^{206}Bi		
τ	$7.7(5)$ s	$0.40(5)$ s	$3.04(6)$ μ s	$13.0(10)$ ms	$0.89(10)$ ms		
E (keV)	$248.5+\Delta$	428	$59+\Delta$	808	1043		
Decay	$E3$	$E3$	$E2$	$E3$	$M2/E3$		
Refs.	[Huys 92]	[Hage 72]	[Rao 81]	[Raki 74]	[Raki 74]		
N	^{200}At	^{202}At	^{204}At	^{206}At	^{208}At		
τ	7.3_{15}^{26} s	$0.46(5)$ s	$108(10)$ ms	$1173(30)$ ns	$45(2)$ ns		
E (keV)	344	487	587	808	1090		
Decay	$E3 + \alpha$	$E3 + \alpha$	$E3 + \alpha$	$E1$	$E1/E3$		
Refs.	[Usi 05]	[Huys 92]	[More 69, Gipp 75]	[Drac 09b]	[Fant 84]		
N	^{202}Fr	^{204}Fr	^{206}Fr	^{208}Fr	^{210}Fr		
τ	$0.29(5)$ s	$0.8(2)$ s	$0.7(1)$ s	$623(16)$ ns	$29.8(11)$ ns		
E (keV)	$0+\Delta$	316	672	826	1113		
Decay	$E3 + \alpha$	α	$E3 + \alpha$	$E1$	$E1$		
Refs.	[Usi 05]	[Usi 05]	[Ritc 81]	[Drac 09b]	Present work		

(a) [Stoc 56, Astr 57, Frit 58, Lind 77]

4.3. CONFIGURATION ASSIGNMENTS IN ^{210}Fr

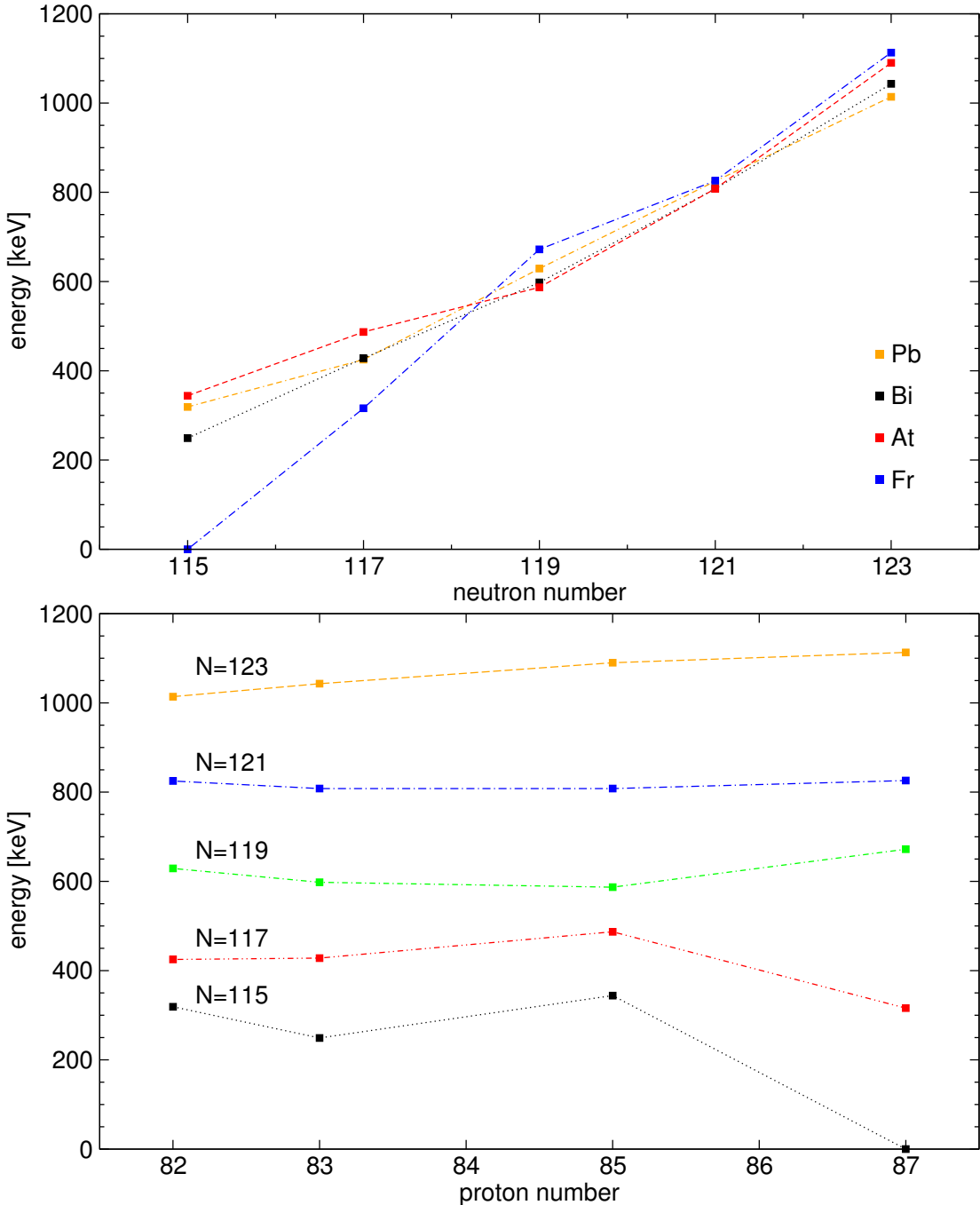


Figure 4.11: A comparison for selected nuclei of the energy of the 10^- isomer for odd-odd isotopes and the $13/2^+$ isomer for even-odd isotopes is shown in the top panel. A similar comparison for isotonic chains is shown in the bottom panel. The point for $Z=82$ represents the $13/2^+$ isomer energy in lead isotopes.

The mysterious case of the 12^- isomer

The 12^- isomer observed at 2018 keV has no equivalent state in neighbouring nuclei. The semi-empirical shell model calculation predicts a 12^- state from the $\pi h_{9/2}^5 \otimes \nu(p_{1/2}^{-2} i_{13/2}^{-1})$ configuration that is in good agreement with the observed energy (see Figure 4.8). Furthermore the energy difference between the calculated 12^- state and the observed state is similar to the agreement for the 10^- isomer (141 keV vs 178 keV) from the same configuration and for which the assignment is more definitive from the systematic behaviour discussed in the previous section. The measured $E3$ transition strength, however, does not agree with the configuration change since $\nu i_{13/2} \rightarrow \nu f_{5/2}$ is $\Delta j = 4$ and anything lower than $M4$ is consequently j -forbidden. Yet the $E3$ strength measured, ~ 15 W.u. (see Table 3.5), is enhanced with respect to the Weisskopf estimate and is suggestive of an enhanced $\pi i_{13/2} \rightarrow \pi f_{7/2}$ or $\nu j_{15/2} \rightarrow \nu g_{9/2}$ $E3$ transition. Possibly the configuration or the level is wrong, although the experimental evidence is plausible.

As said previously, such a transition has not been observed in nearby nuclei. This can be explained by the relatively high energy $E3$ transition that is possible in ^{210}Fr and the E_γ^7 dependence for the strength, while, for example, in ^{208}At , the $12^- \rightarrow 9^+$ energy gap is only 745 keV Ref. [Fant 84]. The situation is similar in ^{206}At (energy gap of 737 keV [Feng 99]), ^{208}Fr (energy gap of 763 keV [Drac 09b]) and ^{204}Bi (energy gap of 522 keV [Lonn 81]). Note that in ^{204}Bi a 12^- state at 1454 keV is observed but there is no 9^+ state.

At this point the structural origin of the isomer at 2018 keV remains uncertain.

The $J^\pi=(23)^+$ isomer

A high-spin isomer was identified in ^{210}Fr at an excitation energy of 4417 keV, with a measured lifetime of $686(17)$ ns (see Chapter 3). The isomer decays through 663.3 and 573.5 keV γ -rays. These two decay paths recombine lower in the scheme at a state with energy 3357 keV. The level scheme for the high spin intermediate decay of the isomer is shown in Figure 4.12.

States from 2206 keV up to the state at 3357 keV (see Figure 3.9) may belong to the $\pi(h_{9/2}^4 i_{13/2}) \otimes \nu(p_{1/2}^{-2} f_{5/2}^{-1})$ multiplet with a maximum possible spin of $21\hbar$, while the two states at 3754 and 3844 keV could be either from this multiplet or from the $\pi(h_{9/2}^3 i_{13/2} f_{7/2}) \nu(p_{1/2}^{-2} f_{5/2}^{-1})$ configuration for which maximal alignment results in $J^\pi = 23^-$. Higher spin states can only be reached by exciting one more proton to the $i_{13/2}$ shell, or through core excitation, with either of these scenarios leading to a parity change. The angular distributions for the 663.3 and 573.5 keV γ -rays, $+0.41(6)$ and $+0.35(7)$, respectively, support $E3$ multi-polarity assign-

Table 4.3: Branching ratios and transition strengths for the decay of the isomer at 4417 keV in ^{210}Fr , and comparison with ^{211}Fr [Byrn 86b] and ^{209}Fr [Drac 09a].

Nucleus	Initial state τ	Final state J^π	E_γ (keV)	I_γ	$\sigma\lambda$	α_T^a	Transition strength (W.u.)
^{210}Fr (b)	$(23)^+ 4417 \text{ keV}$						
	686(17) ns	$(20)^-$	663.3	52.9(14)	$E3$	0.0569	8.5(3)
		$(20)^-$	573.5	47.1(12)	$E3$	0.0861	21.0(8)
	$(23)^+ 4417 \text{ keV}$						
	686(17) ns	$(21)^-$	663.3	52.9(14)	$M2$	0.1980	$6.1(3) \times 10^{-3}$
		$(21)^-$	573.5	47.1(12)	$M2$	0.3033	$1.12(4) \times 10^{-2}$
	$(23)^+ 4417 \text{ keV}$						
	686(17) ns	$(21)^-$	663.3	52.9(14)	$M2$	0.1980	$6.6(3) \times 10^{-3}$
		$(20)^-$	573.5	47.1(12)	$E3$	0.0861	19.6(8)
^{211}Fr	$45/2^- 4657 \text{ keV}$						
	179.6(17) ns ^(c)	$39/2^+$	728.3	100(1)	$E3$	0.045	32.5(5)
^{209}Fr	$45/2^- 4660 \text{ keV}$						
	606(26) ns	$39/2^+$	620.2	100.0(2)	$E3$	0.0686	28.8(12)
		$41/2^+$	335.5	1.1(2)	$M2$	1.602	$4.9(9) \times 10^{-3}$

(a) Values are taken from Ref. [Kibe 08].

(b) For convenience J_i^π and J_f^π only represent one of the possible set of spin assignments for the states.

(c) The lifetime value is from this work (see Figure 2.12).

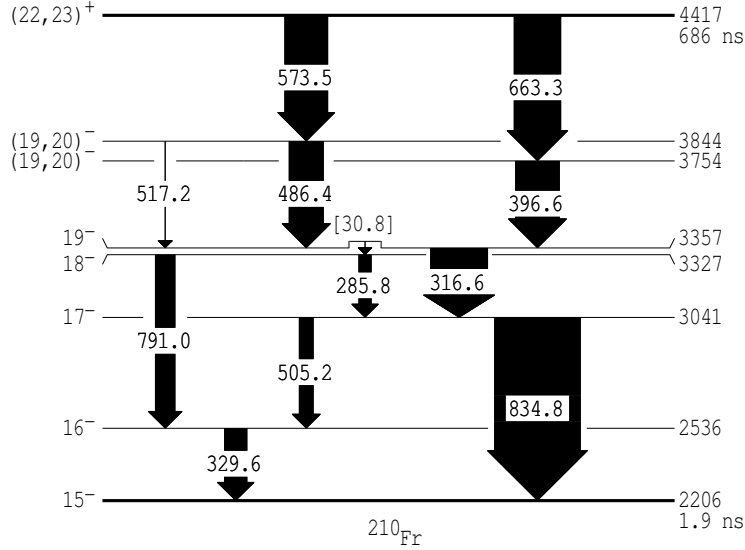


Figure 4.12: Partial level scheme for ^{210}Fr showing the decay of the isomer at 4417 keV.

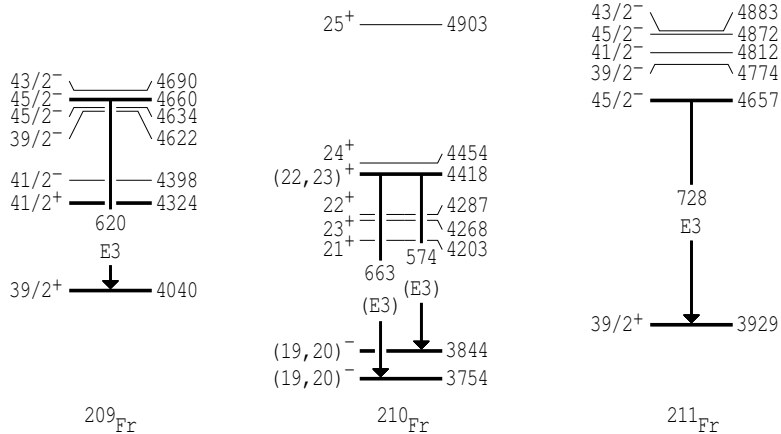


Figure 4.13: Comparison between experimental energies of the isomer states and calculated energies for the different members of the $h_{9/2}^3 i_{13/2}^2$ multiplet (coupled to the appropriate neutron configuration, see text) in ^{209}Fr , ^{210}Fr and ^{211}Fr . Experimental states and transitions are in bold.

ments although the presence of residual alignment with a state of this lifetime is surprising.

In ^{209}Fr [Drac 09a] and ^{211}Fr [Byrn 86b], long lived isomers with $J^\pi = 45/2^-$ have been identified at energies of 4660 and 4658 keV, respectively. The configurations assigned to these isomers are $\pi(h_{9/2}^3 i_{13/2}^2)_{45/2^-} \otimes \nu(p_{1/2}^{-2} f_{5/2}^{-2})_{0+}$ and $\pi(h_{9/2}^3 i_{13/2}^2)_{45/2^-} \otimes \nu(j^{-2})_{0+}$, respectively, in which the neutron-hole pairs are coupled to zero angular momentum. These configurations correspond to the scenario

4.3. CONFIGURATION ASSIGNMENTS IN ^{210}Fr

presented above for ^{210}Fr with the addition of an odd neutron hole in the $f_{5/2}$ orbital: $\pi(h_{9/2}^3 i_{13/2}^2) \otimes \nu(p_{1/2}^{-2} f_{5/2}^{-1})$, for which the maximal spin is 25^+ . However, the residual interactions do not favour mutual alignment of high-spin protons and neutron-holes. This is reflected in Figure 4.13 which shows calculations including residual interactions for ^{210}Fr and the two neighbouring isotopes. In ^{210}Fr a number of high spin positive parity states are predicted, although it is not obvious, at first sight, which should be associated with the isomer. The 23^+ state is the favoured candidate however, according to the calculations, there could be a competitive $E2$ γ -decay to a lower 21^+ state. This is not observed, but neither are the equivalent transitions in the neighbouring isotopes; this probably indicates the level of uncertainty in the calculation. This scenario is consistent with the current (tentative) spin assignment for the state and the likely $E3$ decays to the 3844 and 3754 keV states; the latter proposition depends, of course, on the configuration of those states. (Note that core excitations that could produce high spin positive parity states are unlikely to occur at such low energy.)

Were the 23^+ assignment correct, there are still unresolved issues related to the configuration of the two 20^- states at 3754 and 3844 keV. The transition strength of the 663.3 keV $E3$ would be ≈ 10 W.u. which suggests that it is from the spin-flip transition $\pi\tilde{i}_{13/2} \rightarrow \tilde{h}_{9/2}$, or that secondary mixing (engendered by the 3^- coupling) is much less significant (see Ref. [Pole 86]). However, it is not clear why the calculation for the lower 20^- state from the $\pi(h_{9/2}^4 i_{13/2}) \otimes \nu(p_{1/2}^{-2} f_{5/2}^{-1})$ multiplet would be so much lower in energy than the experimental state ($\Delta=357$ keV). The case for the higher 20^- state is similar in that it would be fed by a ≈ 20 W.u. transition which strongly suggests the involvement of the $\pi\tilde{i}_{13/2} \rightarrow \tilde{f}_{7/2}$ transition. As previously stated (see Section 4.2.2), if fully aligned angular momenta were required, either in the higher 20^- state or in the 23^+ state, then an underestimation of the state energy by the calculation could be understood from Pauli blocking not being considered. But this is not the case here, and the difference between calculation and experiment, not seen in ^{209}Fr or ^{211}Fr for the $39/2^+$ states, remains unexplained.

There is also the possibility that the 573.5 and 663.3 keV transitions are of $M2$ multi-polarity, which would also lead to a significant lifetime. This would obviously have implications for the configuration of the two lower states. Considering the possible configuration changes, the implied $M2$ strength for the 663.3 keV γ -ray, of ~ 0.006 W.u., is consistent with a j -forbidden $M2$ transition [Drac 09a]. One possibility then, is that the state at 3754 keV is a member of the $\pi(h_{9/2}^3 i_{13/2} f_{7/2}) \otimes \nu(p_{1/2}^{-2} f_{5/2}^{-1})$ multiplet ($\Delta\ell = 4$ for the transition) but it would not be from the $\pi(h_{9/2}^4 i_{13/2}) \otimes \nu(p_{1/2}^{-2} f_{5/2}^{-1})$ multiplet since a transition strength of

~ 0.1 W.u. would be expected [Drac 09a]. Similarly, the implied strength for a 573.5 keV $M2$ is lower than allowed $M2$ values but it is also higher than a typical j -forbidden $M2$ transition strength. The issues of the multi-polarity of these transitions and the constraints on the configurations of the two states at 3754 and 3844 keV remain under investigation.

States above the isomer at 4417 keV

Several states have been identified above the 23^+ isomer. Since no lifetimes were observed, configuration assignments are unclear. The 1096.9 keV transition, however, is similar in energy to the $10^- \rightarrow 7^+$ energy gap observed in the N=123 isotones (see previous section). It is therefore a possibility that this transition is the corresponding $E3$ and that the state has $J^\pi = 26^-$. This would arise from the configuration $[\pi(h_{9/2}^3 i_{13/2}^2) \otimes \nu(p_{1/2}^{-2} i_{13/2}^{-1})]_{26^-}$. The calculation for this configuration gives a state at $E = 5773$ keV in comparable agreement ($\Delta = 259$ keV) to the level of agreement of the 10^- and 12^- states ($\Delta = 178$ keV and $\Delta = 141$ keV), see Figure 4.8. The strength for such a transition is around $200 e^2\text{fm}^6$ (see previous section) or ~ 0.07 W.u. which means that a favoured $E1$ to the 25^+ state from the $\pi(h_{9/2}^3 i_{13/2}^2) \nu(p_{1/2}^{-2} f_{5/2}^{-1})$ multiplet should be seen. The absence of such a transition would probably mean that the 1097 keV transition is not $E3$ as the strength would imply, for a 100% branching ratio, a lifetime in the μs range. The state at 4742 keV more likely has $J^\pi = 24^+$ since the energy gap with the 23^+ state is similar to that between the 15^- and 16^- states that have related structure. It is worth noting that if one of the states at 4982 and 5004 keV had $J^\pi = 25^+$ then the $M1$ would probably be favoured.

There remains the possibility that neutron core excitation occurs at energies above 5 MeV. States arising from such a phenomenon are calculated at higher energies than what is observed in this study (see Table 4.4). Note, however, that Byrne *et al.* [Byrn 86b, Byrn 86a] calculated neutron core excitation several hundreds of keV higher than the experimental states in heavier francium isotopes. If similar overestimates apply here then neutron core excitation could become competitive and one could expect to see the $\tilde{j}_{15/2} \rightarrow \tilde{g}_{9/2}$ enhanced transitions leading to an isomeric initial state. Hints for such a transition should have been observable in the second experiment, so perhaps the relevant spin was not reached, possibly due to fission competition.

Table 4.4: Calculated energy for selected neutron core excitation configurations.

Configuration	Energy (keV)
$[\pi(h_{9/2}^3 i_{13/2} f_{7/2}) \otimes \nu((p_{1/2}^{-2} f_{5/2}^{-2})_{2+} g_{9/2})_{13/2+}]_{26-}$	6065
$[\pi(h_{9/2}^3 i_{13/2} f_{7/2}) \otimes \nu((p_{1/2}^{-2} f_{5/2}^{-2})_{4+} g_{9/2})_{17/2+}]_{27-}$	6034
$[\pi(h_{9/2}^3 i_{13/2}^2) \otimes \nu((p_{1/2}^{-2} f_{5/2}^{-2})_{2+} g_{9/2})_{13/2+}]_{26-}$	5966
$[\pi(h_{9/2}^3 i_{13/2}^2) \otimes \nu((p_{1/2}^{-2} f_{5/2}^{-2})_{4+} g_{9/2})_{17/2+}]_{27-}$	5840

CHAPTER 4. THE STRUCTURE OF ^{210}FR

Chapter 5

Concluding comments

“Obélix il y a un temps pour déchiffrer des hiéroglyphes et puis il y a un temps pour sortir d'une pyramide, hein, ce serait peut être le moment d'avoir le sens des priorités.”

— Christian Clavier (as Astérix), in
Astérix et Obélix: Mission Cléopâtre

The time-correlated γ -ray spectroscopy measurements reported in this work bring a new description of the structure of ^{210}Fr . Both the general behaviour and the more detailed structural features have been elucidated. The first characteristic of the level scheme presented is the quantity of states at low spin although this is no complete surprise for an odd-odd nucleus. As anticipated, the description was also more complex not only due to the odd-odd nature of ^{210}Fr but also because the well-ordered shell structure found around the lead core is affected by configuration mixing. Unfortunately while the mixing can be qualitatively inferred there is no code available to tackle this issue quantitatively in the present case with eight valence nucleons. Three isomers with configurations related to observed states in other nuclei in the trans-lead region have, however, been measured and most of their characteristics have been described and understood, with the exception of the 12^- isomer at 2018 keV which is of unknown origin.

5.1 Experimental measurements and main structural assignments

A 10^- isomer was expected in ^{210}Fr , as it has been observed in all known nuclei in the ^{208}Pb region with three neutron-holes and an odd number of protons. It is due to the $i_{13/2} \rightarrow f_{5/2}$ configuration change and the j -forbidden decay. This

work reports a 29.8(11) ns lifetime for the isomer that decays via a hindered $E1$ γ -ray with transition strength similar to what was measured in nearby nuclei.

The isomer at 2206 keV has $J^\pi = 15^-$ and a short lifetime of 1.9(4) ns. The configuration assigned is $\pi(h_{9/2}^4 i_{13/2})\nu(p_{1/2}^{-2} f_{5/2}^{-1})$ and the decay is via an $E1$ transition. The 14^+ daughter state configuration is $\pi h_{9/2}^5 \nu(p_{1/2}^{-2} f_{5/2}^{-1})$ which means that this $E1$ decay is also j -forbidden.

Finally, the isomer at 4417 keV has a long lifetime, $\tau = 686(17)$ ns, but the spin assignment, while most likely 23^+ , remains unclear. The isomer is almost undoubtedly a member of the $\pi(h_{9/2}^3 i_{13/2}^2)\nu(p_{1/2}^{-2} f_{5/2}^{-1})$ multiplet and the observed decays are most likely enhanced $E3$ transitions. For nuclei near $A \sim 208$, enhanced $E3$ transition strengths are usually observed when a proton (or proton-hole) de-excites from $|\tilde{i}_{13/2}\rangle$ to $|\tilde{f}_{7/2}\rangle$ and/or when a neutron (or neutron-hole) de-excites from $|\tilde{j}_{15/2}\rangle$ to $|\tilde{g}_{9/2}\rangle$ [Hama 74]. Such $E3$ γ -ray strengths were compiled by Bergström *et al.* [Berg 85], and discussed in detail by A. P. Byrne [Byrn 86a]. The enhanced strengths for ^{209}Fr and ^{211}Fr (see Table 4.3) are consistent with the transition strengths expected for the $\tilde{i}_{13/2} \rightarrow \tilde{f}_{7/2}$ proton de-excitation. If the 573.5 and 663.3 keV transitions were to be $E3$, the strengths reported in this thesis (see Table 4.3) would be somewhat less enhanced than the typical values observed.

5.2 Shell model calculation

Semi-empirical shell model calculations, by mean of comparison with experiments, were used to guide the configuration assignments for the experimental states. This approach, however, is in constant evolution due to the fact that not all two-body interactions are experimentally known (see Appendix E) and from one study to another, some of them may be unveiled. It therefore made sense to perform updated semi-empirical shell model calculations for relevant nuclei near ^{210}Fr , including the neighbouring francium isotopes and the ^{205}Pb neutron core. Although the new calculations do not suggest changes in the previous configuration assignments for these nuclei (the differences to prior calculations are small), the systematic calculations and comparisons highlight the (unsurprising) conclusion that the agreement with experiment degrades rapidly with the addition of neutron holes. This is surely due to the fact that increasing numbers of close-lying configurations can give the same spin and parity and hence the experimental states are not pure but mixed. Unfortunately, present computer limitations mean that mixing calculations can only be performed close to the shell closures.

5.3. FUTURE WORK

For some states, however, the predicted configurations are relatively pure and these are often found at high spins because only a few, or even just one, configuration possesses a (energy competitive) member that has a particular high spin. This is the case for the 686 ns isomer in ^{210}Fr for which the multiplet assignment is rather definite, although there is still some doubt over the $(23)^+$ assignment.

5.3 Future work

The degradation in the level of agreement between calculation and experiment, moving away from ^{208}Pb , is an incentive for investigating nuclei still spherical but far away from the inert core. For example, only a few states, at the moment, are known in $^{206,207}\text{Fr}$, although these nuclei might have transitioned to more deformed shape.

A number of assignments in ^{210}Fr could be improved from a new measurement. For example, the electromagnetic nature of the direct decays of the isomer at 4417 keV is not known with certainty and there is still room for an $M2$ assignment rather than $E3$. This could be solved by direct conversion electron measurements or by a more comprehensive angular distribution measurement, with better angular coverage. The latter option would only be useful, if the reason why alignment is not lost following the decay of the high-spin long-lived isomer is understood.

A better measurement for ^{210}Fr may identify new structure at higher spins. Either neutron core excitation or a j -forbidden $E3$ transition is expected to occur as an “echo” of the $10^- \rightarrow 7^+$ transition lower in the level scheme (see Section 4.3). The relevant angular momentum region is likely to approach the fission barrier and to explore this part of the level scheme would likely require more statistics than CAESAR could provide in a week-long experiment.

Finally, the lighter francium isotope, ^{208}Fr , could be studied. States in this nucleus have been investigated (as a by-product) up to $J \sim 16\hbar$ [Drac 09b], but the experiment was not optimal for the production of ^{208}Fr . As a result, of the expected structural features, only the 10^- isomer was measured and a high-spin study is warranted. The problematic 12^- isomer in ^{210}Fr may be seen in ^{208}Fr and shed light on its structure. More important would be the opportunity to keep investigating the occurrence of a high-spin isomer at around 4.5 MeV. Although it is likely to be a difficult measurement due to increased fission competition, the prospect of experimental observations that enable a better understanding of the structure of nuclei in this region makes it a worthwhile goal.

CHAPTER 5. CONCLUDING COMMENTS

Appendix A

Deconvoluting unresolved transitions - an example

The technique outlined in Section 2.3.3 for the deconvolution of unresolved transitions proved very useful in the study of ^{210}Fr since several transitions were significantly contaminated.

The region around 817 keV contains four γ -rays intense enough to create significant contamination across neighbouring gates (see Figures A.1, A.2 and A.3). These γ -rays are the 814.4 keV from the EC-decay of ^{207}At into ^{207}Po , the 816.8 keV transition from ^{210}Fr , the 817.8 keV γ -ray in ^{210}Rn populated directly from the heavy ion reaction and in the EC-decay of ^{210}Fr into ^{210}Rn , and, finally, the 820.9 keV γ -ray from ^{211}Fr . The method requires a coincident γ -ray that is only associated with each of these transitions. The level scheme for ^{210}Rn was previously known and suggested the use of the 643.8 keV transition to identify the yield of this γ -ray in each gate since it is populated through both mechanisms. For ^{210}Fr , the study of other gates indicates that the 721.2 keV γ -ray is a suitable candidate. The 357.6 keV in ^{211}Fr [Byrn 86b] and the 300.7 keV in ^{207}Po [Jons 71] are also chosen. The intensity for each of the γ -rays is split between gates as shown in Table A.1 and therefore it can be written in matrix form as¹:

¹Precise values are required because inverting a square matrix requires $\gtrsim N^3/2$ operations. Moreover the smallest intensity peaks are at the level of $\sim 0.1\%$ of the strongest peaks.

APPENDIX A. DECONVOLUTING UNRESOLVED TRANSITIONS - AN EXAMPLE

Table A.1: Partitioning of the intensity for specific γ -rays in the four gates shown on Figure A.1.

E_γ	counts in gate 1	counts in gate 2	counts in gate 3	counts in gate 4
300.7	3924	1935	0	0
357.6	0	0	2200	11226
643.8	0	5900	12511	307
721.2	1013	11884	5037	0

$$\begin{aligned} \begin{pmatrix} \text{gate a} \\ \text{gate b} \\ \text{gate c} \\ \text{gate d} \end{pmatrix} &= \begin{pmatrix} \alpha_{11} & \alpha_{12} & \alpha_{13} & \alpha_{14} \\ \alpha_{21} & \alpha_{22} & \alpha_{23} & \alpha_{24} \\ \alpha_{31} & \alpha_{32} & \alpha_{33} & \alpha_{34} \\ \alpha_{41} & \alpha_{42} & \alpha_{43} & \alpha_{44} \end{pmatrix} \cdot \begin{pmatrix} 300.7 \\ 357.6 \\ 643.8 \\ 721.2 \end{pmatrix} \\ &= \begin{pmatrix} 0.670 & 0 & 0 & 0.056 \\ 0.330 & 0 & 0.315 & 0.663 \\ 0 & 0.164 & 0.668 & 0.281 \\ 0 & 0.836 & 0.016 & 0 \end{pmatrix} \cdot \begin{pmatrix} 300.7 \\ 357.6 \\ 643.8 \\ 721.2 \end{pmatrix}, \end{aligned} \quad (\text{A.1})$$

and “clean” gates are obtained through:

$$\begin{aligned} \begin{pmatrix} \text{Gate on 814.4 keV} \\ \text{Gate on 816.8 keV} \\ \text{Gate on 817.8 keV} \\ \text{Gate on 820.9 keV} \end{pmatrix} &= \begin{pmatrix} 1.574 & -0.166 & 0.079 & -0.015 \\ -0.008 & 0.016 & -0.04 & 1.203 \\ 0.414 & -0.841 & 1.903 & -0.373 \\ -0.981 & 1.991 & -0.943 & 0.185 \end{pmatrix} \\ &\cdot \begin{pmatrix} \text{gate a} \\ \text{gate b} \\ \text{gate c} \\ \text{gate d} \end{pmatrix}, \end{aligned} \quad (\text{A.2})$$

The results of the subtraction are shown in Figure A.4. While the peak fit of the region suggested four γ -rays, the observation of unknown lines, after deconvolution, made apparent the presence of, at least, a fifth (low intensity) line in this region. This demonstrates the precision of the method in deconvoluting contributions.

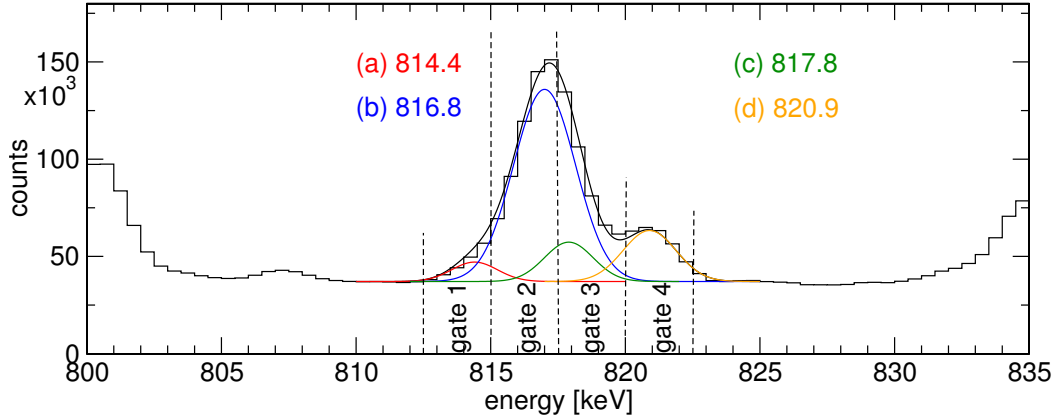


Figure A.1: In-beam matrix with a narrow prompt coincidence condition (± 30 ns) zoomed on the ~ 817 keV region.

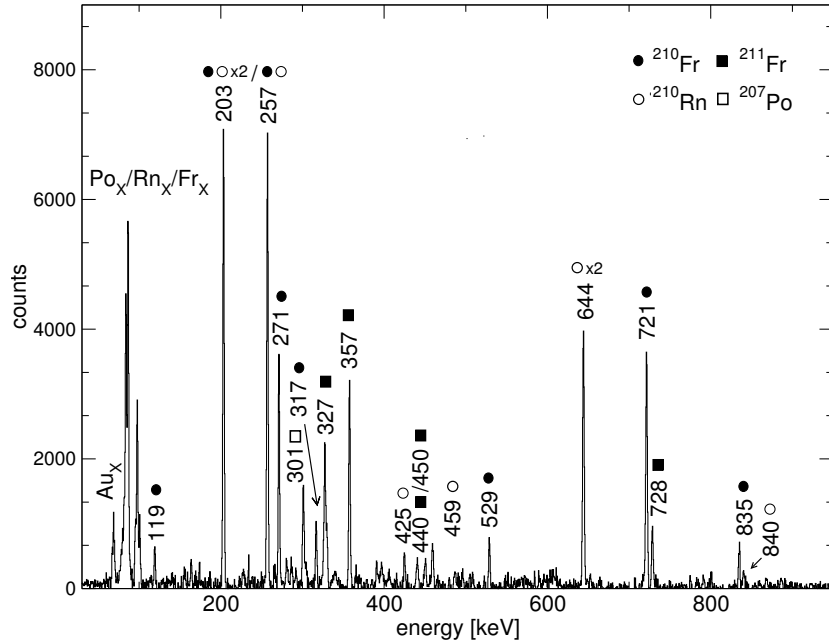


Figure A.2: Coincidence spectrum obtained when gating on the entire area encompassed by gate 1, 2, 3 and 4. The “x2” symbol means that the transition results from two different production mechanisms for ^{210}Fr .

APPENDIX A. DECONVOLUTING UNRESOLVED TRANSITIONS - AN EXAMPLE

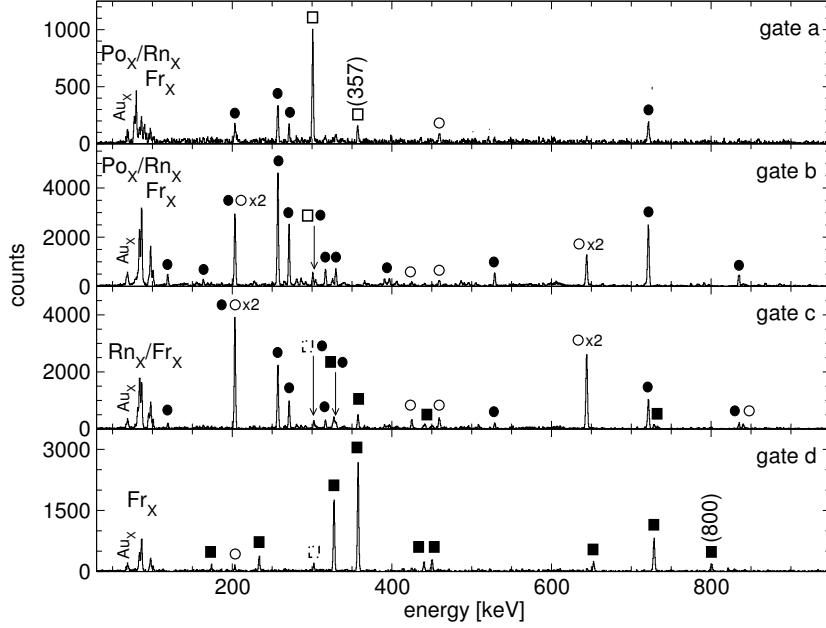


Figure A.3: Coincidence spectra for individual gates before deconvolution. The dashed square signifies that the peak has an unknown origin.

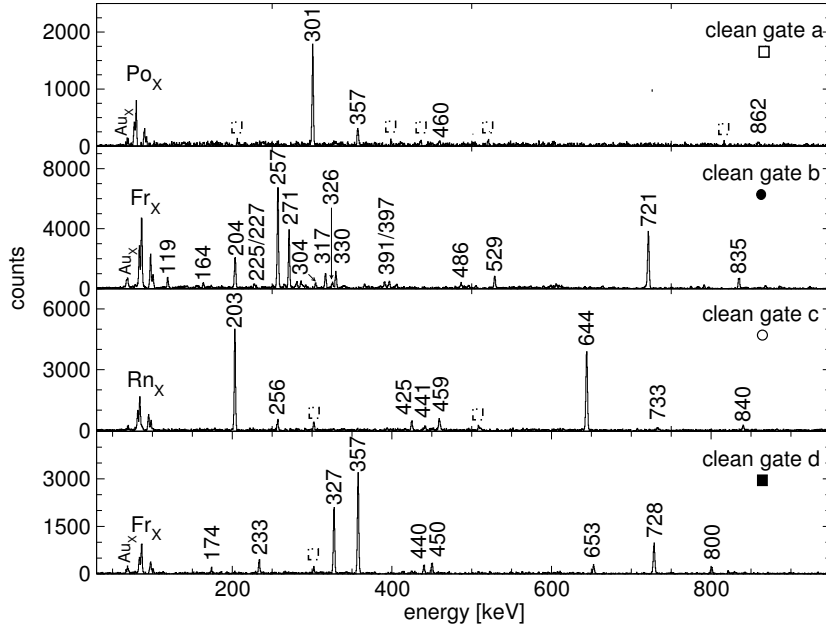


Figure A.4: Coincidence spectra for individual gates after deconvolution. From top to bottom gates on (a) 814.4 keV in ^{207}Po , (b) 816.8 keV in ^{210}Fr , (c) 817.8 keV in ^{210}Rn and 820.9 keV in ^{211}Fr .

Appendix B

Detailed γ - γ coincidence arguments

The level scheme presented in Chapter 3 was built using a set of logical arguments deduced from observations in the in-beam data. More detailed arguments are required for the present case because the absence of significant lifetimes means that distinctive separation of the level scheme into parts was not possible. The logic used is shown in the pages that follow and completes the presentation made in Section 3.2.

APPENDIX B. DETAILED γ - γ COINCIDENCE ARGUMENTS

The prompt coincidence spectra for 519.6 and 544.4 keV are identical.

The prompt coincidence spectra for 519.6 and 544.4 keV select out five main transitions below the state at 1627 keV: 143.2, 225.4, 289.1, 793.0 and 902.5 keV.

The main γ -rays from the prompt coincidence spectra for 118.9, 203.5 and 256.9 keV are 816.8 and 721.2 keV, and these γ -rays are not seen in the prompt coincidence spectra for 519.6 and 544.4 keV.

The prompt coincidence spectra for 289.1 and 225.4 keV are identical.

The 902.5 and 143.2 keV transitions are not observed in the prompt coincidence spectra for 225.4 and 289.1 keV.

The 793.0 keV transition is present in the prompt coincidence spectra for 225.4 and 289.1 keV and balances the intensity of the 519.6 and 544.4 keV transitions

A weak 816.8 keV peak is in the prompt coincidence spectra for 225.4 and 289.1 keV, echoing the presence of a weak 289.1 keV transition in the prompt coincidence spectrum for 816.8 keV. The 225.4 keV γ -ray cannot be seen due to low branching ratio.

The prompt coincidence spectrum for 793.0 keV shows 519.6, 544.4, 289.1 and 225.4 keV but does not show 816.8 and 721.2 keV.

(i) 519.6 and 544.4 are parallel and there must be a 24.8 keV transition below or above the 519.6 keV transition making up for the energy gap.

(ii) 793.0 and 289.1(225.4) keV are in cascade and parallel to 902.5 and 143.2 keV.

(iii) The ordering of 519.6(544.4), 793.0, 289.1(225.4) must be as presented in the level scheme.

(iv) There might be a transition linking 289.1(225.4) and 816.8 keV.

(v) 289.1 and 225.4 are parallel and there must be a 63.8 keV transition below or above 225.4 keV making up for the energy gap.

(vi) 289.1 and 225.4 are parallel and there must be a 63.8 keV transition below or above 225.4 keV making up for the energy gap.

(vii) 289.1 and 225.4 are parallel and there must be a 63.8 keV transition below or above 225.4 keV making up for the energy gap.

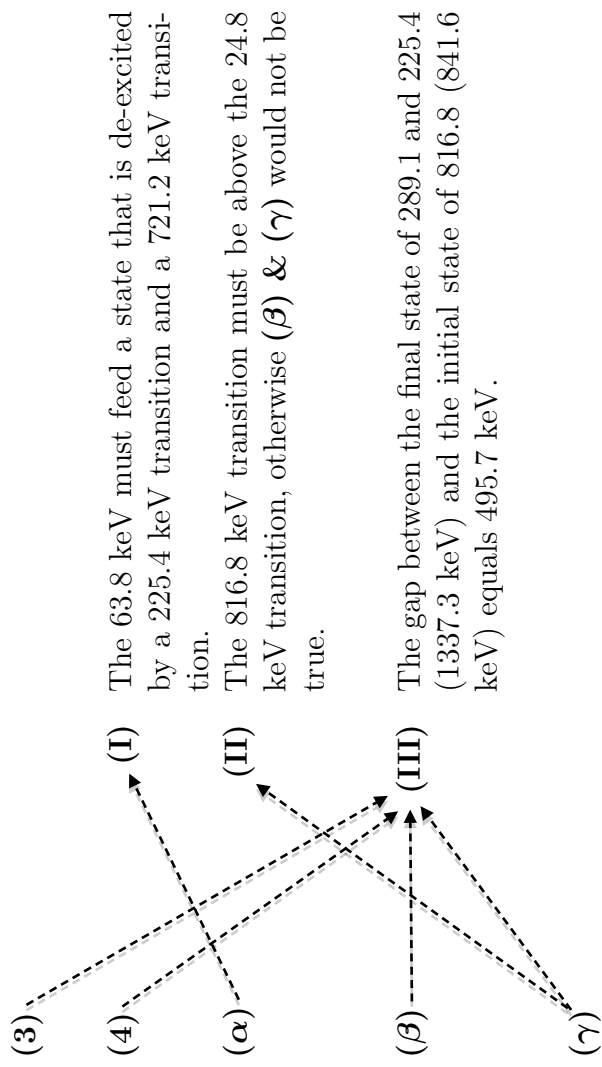
The ordering of 519.6(544.4), 793.0, 289.1(225.4) must be as presented in the level scheme.

There might be a transition linking 289.1(225.4) and 816.8 keV.

The prompt coincidence spectrum for 721.2 keV shows a 816.8 and a 63.8 keV γ -ray. The X- γ prompt coincidence matrix with a gate on 63.8 keV shows 256.9, 721.2, 519.6 keV ...

There is no difference between the prompt coincidence spectra for 793.0 keV and 721.2 keV (apart from the presence of 225.5, 289.1, 519.6 and 544.4 in the first one and 816.8 in the second one).

The energy sum $816.8 + 721.2 + 63.8$ equals the sum $544.4 + 793.0 + 289.1$ (1626.6 keV).



- (I) The 63.8 keV must feed a state that is de-excited by a 225.4 keV transition and a 721.2 keV transition.
- (II) The 816.8 keV transition must be above the 24.8 keV transition, otherwise (β) & (γ) would not be true.

- (III) The gap between the final state of 289.1 and 225.4 (1337.3 keV) and the initial state of 816.8 (841.6 keV) equals 495.7 keV.

The prompt coincidence spectra for 519.6 and 544.4 keV are identical.

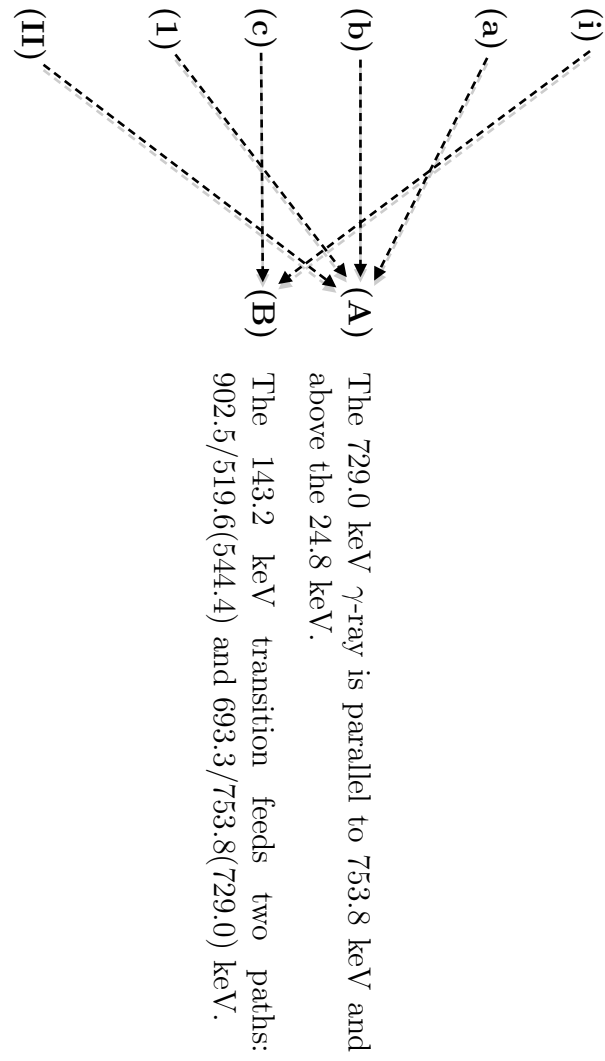
The prompt coincidence spectrum for 143.2 keV shows 519.6(544.4), 693.3, 753.8 and 902.5 keV γ -rays. A 729.0 keV γ -ray is also clearly visible.

The 753.8 keV transition was also observed in the α decay of ^{214}Ac into ^{210}Fr [Kuus 04].

The sum 544.4 + 902.5 equals the sum 753.8 + 693.3 (1446.9).

519.6 and 544.4 are parallel and there must be a 24.8 keV transition below or above 519.6 keV making up for the energy gap.

The 816.8 keV transition must be above the 24.8 keV transition, otherwise (β) & (γ) would not be true.



Appendix C

Measurement of total conversion coefficients

This section presents the measurement of the total conversion coefficients for transitions in ^{210}Fr . As stated in Chapter 2, direct measurements of internal conversion electrons were not made, instead long chopped data from the second experiment was used, benefiting from the presence of the long-lived high spin isomer at 4417 keV. Because the conversion coefficient α_T depends on the electromagnetic nature of the radiation, this measurement allows for multi-polarity assignments to γ -ray transitions.

The tables that follow present how the measurements were done, i.e. the gates that were used and in what matrix as well as details of the intensity balance that was applied to evaluate α_T for which transition (the “:” symbol indicates the measured result, while (##) enumerates the different results, from (1) to (37)).

For completeness, the A_2/A_0 coefficients deduced from angular distribution measurements are also listed where they are known. In all cases, expected values for α_T are taken from Ref. [Kibe 08].

APPENDIX C. MEASUREMENT OF TOTAL CONVERSION COEFFICIENTS

Table C.1: Measurements of total conversion coefficients α_T from intensity balance measurements. Intensities are from the sum of out-of-beam spectra with gates on the 663.3 and 573.5 keV γ -rays.

Transitions (keV)	I_γ	A_2/A_0	$\sigma\lambda$ assumed	Result			$E1$	$M1$	$E2$	$M2$	$E3$	α_T measured
				$E1$	$M1$	$E2$						α_T
505.2	128(9)	-0.69(4)	$M1$				0.159					
791.0	180(13)	+0.25(10)	$E2$					0.0136				
$\therefore (1)$	329.6	237(10)	-0.42(4)				0.0277	0.503	0.110	1.70	0.594	0.396(92)
791.0	180(13)	+0.25(10)	$E2$									
329.6	237(10)	-0.42(4)	$M1$				0.0112	0.159	0.0460	0.444	0.127	0.36(18)
$\therefore (2)$	505.2	128(9)	-0.69(4)									
329.6	237(10)	-0.42(4)	$M1$				0.03					
834.8	723(26)	+0.36(3)	$E2$					0.0122				
$\therefore (3)$	256.9	1000(28)	-0.27(3)				0.0488	0.998	0.235	3.88	1.75	0.088(43)
329.6	237(10)	-0.42(4)		$\therefore (1) 0.396(92)$								
834.8	723(26)	+0.36(3)	$E2$				0.0122					
$\therefore (4)$	256.9	1000(28)	-0.27(3)				0.0488	0.998	0.235	3.88	1.75	0.063(47)
285.8	132(7)	-0.35(2)	$M1$				0.744					
505.2	128(9)	-0.69(4)	$M1$				0.159					
834.8	723(26)	+0.36(3)	$E2$					0.0122				
$\therefore (5)$	316.6	568(18)	+0.34(3)				0.0303	0.562	0.123	1.94	0.701	0.144(65)
834.8	723(26)	+0.36(3)	$E2$				0.0122					
316.6	568(18)	+0.34(3)	$E2$					0.123				
505.2	128(9)	-0.69(4)	$M1$				0.159					
$\therefore (6)$	285.8	132(7)	-0.35(2)				0.0382	0.744	0.168	2.71	1.09	0.83(28)

Table C.2: Measurements of total conversion coefficients α_T from intensity balance measurements. Intensities are from an out-of-beam spectrum with a gate on the 834.8 keV γ -ray.

Transitions (keV)	I_γ	A_2/A_0	$\sigma\lambda$ assumed	Result used	E_1	M_1	E_2	M_2	E_3	α_T measured
486.4	402(18)	-0.34(4)	M_1			0.176				
517.2	20(6)		E_2				0.0340			
$\therefore (7)$	573.5	467(20)			0.00866	0.113	0.0269	0.303	0.0860	0.06(6)
$\therefore (8)$	396.6	503(20)	-0.28(3)	M_1		0.00653	0.0770	0.0196	0.198	0.0569
	663.3	514(23)				0.304				0.276(76)
396.6	503(20)	-0.69(4)	M_1			0.176				
486.4	409(18)	+0.36(3)	M_1				0.0340			
517.2	21(6)		E_2							
$\therefore (9)$	285.8	189(10)	-0.35(2)	M_1		0.0303	0.562	0.123	1.94	0.701
	316.6	725(24)	+0.34(3)							0.143(66)
816.8	593(26)	+0.28(2)	E_2			0.0127				
693.2	56(7)	+0.16(4)	E_2				0.0178			
544.4	102(9)	+0.44(3)	E_2				0.0302			
$\therefore (10)$	519.6	325(16)	-0.44(3)	M_1		0.147				
	256.9	1000(30)	-0.27(3)	E_1		0.0488	0.998	0.235	3.88	1.75
227.3	62(6)	+0.37(4)	E_2			0.353				
$\therefore (11)$	203.5	341(13)	-0.39(4)			0.0846	1.911	0.520	8.612	5.305
	256.9	1000(30)	-0.27(3)	E_1		0.0488				0.129(48)
$\therefore (12)$	227.3	62(6)	+0.37(4)	E_2						
	225.4	341(13)	-0.39(4)							
$\therefore (13)$	721.2	487(23)	+0.27(3)	E_2		0.140				
	225.4	48(5)	-0.21(4)	M_1						
	63.9	26(4)			0.0846	1.91	0.520	8.61	5.31	1.84(15)
	902.5	91(10)	+0.32(3)	E_2		0.1436				
	693.2	56(7)	+0.16(4)	E_2		0.0164				
$\therefore (14)$	143.2	49(5)	-0.32(4)							2.04(40)
					0.198	5.16	1.98	30.0	32.7	23(4)

APPENDIX C. MEASUREMENT OF TOTAL CONVERSION COEFFICIENTS

Table C.3: Measurements of total conversion coefficients α_T from intensity balance measurements. Intensities are from an out-of-beam spectrum with a gate on the 256.9 keV γ -ray.

Transitions (keV)	I_γ	A_2/A_0	$\sigma\lambda$	Result assumed	E1	M1	$E2$	$M2$	$E3$	α_T measured
486.4	525(17)	-0.34(4)		M1		0.176		0.0340		
517.2	26(8)			E2						
\therefore (15)	573.5	691(22)				0.00866	0.113	0.0269	0.303	0.0860 -0.06(4)
\therefore (16)	396.6	602(18)	-0.28(3)	M1		0.00653	0.0770	0.0196	0.198	0.0569 < 0.1
\therefore (17)	663.3	759(23)			0.311	8.75	4.27	59.2	90.0	9.43(51)
816.8	816(26)	+0.28(2)		E2			0.0127			
693.2	82(7)	+0.16(4)		E2			0.0178			
544.4	143(9)	+0.44(3)		E2			0.0302			
519.6	413(16)	-0.44(3)		M1		0.147				
227.3	65(4)	+0.37(4)		E2			0.353			
\therefore (18)	203.5	462(14)	-0.39(4)		0.0846	1.91	0.520	8.61	5.31	2.14(12)
816.8	816(26)	+0.28(2)		E2			0.0127			
693.2	82(7)	+0.16(4)		E2			0.0178			
544.4	143(9)	+0.44(3)		E2			0.0302			
519.6	413(16)	-0.44(3)		M1		0.147				
227.3	65(4)	+0.37(4)		M1		1.403				
\therefore (19)	203.5	462(14)	-0.39(4)		0.0846	1.91	0.520	8.61	5.31	1.99(12)
902.5	158(11)	+0.32(3)		E2			0.0104			
693.2	82(7)	+0.16(4)		E2			0.0178			
\therefore (20)	143.2	60(5)	-0.32(4)		0.198	5.16	1.98	30.0	32.7	3.05(40)
721.2	683(23)	+0.27(3)		E2			0.0164			
225.4	42(5)	-0.21(4)		M1						
\therefore (21)	63.9	23(4)			0.355	10.4	74.1	319.7	3051	29.6(48)

Table C.4: Measurements of total conversion coefficients α_T from intensity balance measurements. Intensities are from an out-of-beam spectrum with a gate on the 203.5 keV γ -ray.

Transitions (keV)	I_γ	A_2/A_0	$\sigma\lambda$ assumed	Result used	$E1$	$M1$	α_T $E2$	$M2$	$E3$	α_T measured
486.4	314(13)	-0.34(4)	$M1$			0.176				
517.2	15(5)		$E2$			0.0304				
$\therefore (22)$	573.5	343(14)			0.00866	0.113	0.0269	0.303	0.0860	0.12(7)
396.6	365(13)	-0.28(3)	$M1$			0.304				
$\therefore (23)$	663.3	388(17)			0.0653	0.770	0.0196	0.198	0.0569	0.223(69)
721.2	410(17)	+0.27(3)	$E2$			0.0164				
225.4	34(4) ^(a)	-0.21(4)	$M1$			1.44				
$\therefore (25)$	63.9	18(3)			0.355	10.4	74.1	319.7	3051	26.8(48)
721.2	410(17)	+0.28(2)	$E2$			0.0164				
693.2	95(8)	+0.16(4)	$E2$			0.0178				
544.4	116(8)	+0.44(3)	$E2$			0.0302				
519.6	209(10)	-0.44(3)	$M1$			0.147				
$\therefore (26)$	118.9	72(4)	+0.36(4)		0.311	8.75	4.27	59.2	89.96	10.5(7)
256.9	737(22)	-0.27(3)	$E1$	0.0488						
$\therefore (27)$	118.9	72(4)	+0.36(4)	0.311	8.75	4.27	59.2	89.96	10.5(7)	
902.5	92(9)	+0.32(3)	$E2$			0.0104				
693.2	51(5)	+0.16(4)	$E2$			0.0178				
$\therefore (28)$	143.2	33(3)	-0.32(4)	0.198	5.16	1.98	30.0	32.7	3.39(51)	

(a) Using observed branching ratio in gates where the 225.4 keV γ -ray peak has sufficient counts for the intensity to be extracted.

APPENDIX C. MEASUREMENT OF TOTAL CONVERSION
COEFFICIENTS

Table C.5: Measurements of total conversion coefficients α_T from intensity balance measurements. Intensities are from an out-of-beam spectrum with a gate on the 505.2 keV γ -ray.

Transitions (keV)	I_γ	A_2/A_0	$\sigma\lambda$ assumed	Result used	$E1$	$M1$	$E2$	$M2$	$E3$	α_T measured
256.9	1000(45)	-0.27(3)	$E1$		0.0488					
$\therefore (29)$	329.6	761(42)	-0.42(4)		0.0277	0.503	0.110	1.70	0.594	0.378(98)

Table C.6: Measurements of total conversion coefficients α_T from intensity balance measurements. Intensities are from an out-of-beam spectrum with a gate on the 118.9 keV γ -ray.

	Transitions (keV)	I_γ	A_2/A_0	σ_λ	Result assumed used	$E1$	$M1$	α_T $E2$	$M2$	$E3$	α_T measured
.. (30)	256.9 203.5	1000(37) 425(21)	-0.27(3) -0.39(4)	$E1$		0.0488					
						0.0846	1.91	5.20	8.61	5.31	1.47(15)
	721.2 225.4	561(37) 70(7)	+0.27(3) -0.21(4)	$E2$ $M1$			1.44	0.0164			
.. (31)	63.9	37(7)				0.355	10.4	74.1	319.7	3051	19.0(34)

 APPENDIX C. MEASUREMENT OF TOTAL CONVERSION COEFFICIENTS

Table C.7: Measurements of total conversion coefficients α_T from intensity balance measurements. Intensities are from an out-of-beam spectrum with a gate on the 528.6 keV γ -ray.

Transitions (keV)	I_γ	A_2/A_0	$\sigma\lambda$ assumed	Result used	$E1$	$M1$	$E2$	$M2$	$E3$	α_T measured
816.8	1000(32)	+0.28(2)					0.0127			
$\therefore (32)$	271.0	988(30)	-0.13(4)		0.0431	0.861	0.198	3.24	1.37	< 0.07

Table C.8: Measurements of total conversion coefficients α_T from intensity balance measurements for γ -rays in ^{211}Fr .

Transitions (keV)	I_γ	A_2	σ_λ	α_T [Byrn 86a]	$\alpha_T^{(a)}$
450.2	471(16)	-0.11(1)	$E1$	0.0151	
.. (33) 112.9	69(5)	+0.09(4)	$E2$	5.32	5.9(6)
800.3	1000(32)	+0.14(6)	$E2$	0.0133	
.. (34) 173.7	242(7)	-0.16(1)	$M1$	2.98	2.9(3)
800.3	1000(32)	+0.14(6)	$E2$	0.0133	3.18(19)
.. (35) 233.4	735(21)	+0.163(7)	$E2$	0.323	0.27(6)
					0.38(6)

(a) Measured in the present work.

APPENDIX C. MEASUREMENT OF TOTAL CONVERSION COEFFICIENTS

Table C.9: Measurements of total conversion coefficients α_T from intensity balance measurements for γ -rays in the decay of ^{206}At into ^{206}Po . Intensities are from an out-of-beam spectrum with a gate on the 868.3 keV γ -ray.

Transitions (keV)	I_γ	A_2/A_0	$\sigma\lambda$	α_T [Ling 77] ^(a)	$E1$	$M1$	$E2$	$M2$	$E3$	α_T measured
700.6	1000(30)			$E2$						0.0151
733.6	582(20)			$E2$						0.0137
$\therefore (36)$	256.3	285(10)		0.815	0.0452	0.779	0.205	3.13	1.43	0.49(14)
$\therefore (37)$	477.0	419(14)	$E2$	0.815	0.0452	0.779	0.205	3.13	1.43	0.52(8)
256.3	285(10)									

(a) Note that uncertainties are not given in the publication for the conversion coefficients.

Appendix D

Calculation of the 19^- state energy in ^{210}Fr using partial decomposition

The structure of ^{210}Fr can also be discussed, and state energies calculated, through the method presented by Blomqvist *et. al* [Blom 83] and used, for example, by Poletti *et al.* [Pole 85] to calculate states in ^{209}Rn . In particular the, detailed calculation for the $41/2^-$ state results in an agreement as good as 19 keV between theory and experiment. The method is used in a different fashion here, but is inspired from those two studies. Application of this sort of shell model analysis to ^{210}Fr gives an estimate for the energy of particular states based upon the observation of the assumed configurations in nearby nuclei.

In the following, the notation $\langle \pi \otimes \nu \rangle$ is a shorthand form for:

$$\langle \pi \otimes \nu | V_{\text{int}} | \pi \otimes \nu \rangle. \quad (\text{D.1})$$

Consider the 19^- state in ^{210}Fr for which the structure is assumed to be:

$$\left[\pi \left(h_{9/2}^4 i_{13/2} \right)_{33/2+} \otimes \nu \left(p_{1/2}^{-2} \right)_{0+} f_{5/2}^{-1} \right]_{19-}. \quad (\text{D.2})$$

It can be decomposed as follows:

$$\begin{aligned} \langle ^{210}\text{Fr}, 19^- \rangle &= \left\langle \left(\pi h_{9/2}^4 i_{13/2} \right)_{33/2+} \otimes \nu f_{5/2}^{-1} \otimes (j^{-2})_{0+} \right\rangle_{19-} \\ &= \left\langle \left(\pi h_{9/2}^4 i_{13/2} \right)_{33/2+} \otimes (j^{-2})_{0+} \right\rangle + \left\langle \left(\pi h_{9/2}^4 i_{13/2} \right)_{33/2+} \otimes \nu f_{5/2}^{-1} \right\rangle \\ &\quad + \left\langle \nu f_{5/2}^{-1} \otimes j_{0+}^{-2} \right\rangle + \left\langle \pi h_{9/2}^4 i_{13/2} \right\rangle_{33/2+} + \left\langle j^{-2} \right\rangle_{0+}. \end{aligned} \quad (\text{D.3})$$

APPENDIX D. CALCULATION OF THE 19^- STATE ENERGY IN ^{210}Fr
USING PARTIAL DECOMPOSITION

In ^{211}Fr the $33/2^+$ state at 3244 keV was described as:

$$\left[\pi \left(h_{9/2}^4 i_{13/2} \right)_{33/2^+} \otimes \nu j_{0^+}^{-2} \right]_{33/2^+} \quad (\text{D.4})$$

and its interaction energy can be further developed:

$$\begin{aligned} \langle ^{211}\text{Fr}, 33/2^+ \rangle &= \left\langle \left(\pi h_{9/2}^4 i_{13/2} \right)_{33/2^+} \otimes \nu \left(j^{-2} \right)_{0^+} \right\rangle_{33/2^+} \\ &= \left\langle \left(\pi h_{9/2}^4 i_{13/2} \right)_{33/2^+} \otimes \left(j^{-2} \right)_{0^+} \right\rangle + \langle \pi h_{9/2}^4 i_{13/2} \rangle_{33/2^+} + \langle j^{-2} \rangle_{0^+}. \end{aligned} \quad (\text{D.5})$$

Putting Eq. D.5 in Eq. D.3 gives:

$$\begin{aligned} \langle ^{210}\text{Fr}, 19^- \rangle &= \left\langle \left(\pi h_{9/2}^4 i_{13/2} \right)_{33/2^+} \otimes \nu f_{5/2}^{-1} \otimes \left(j^{-2} \right)_{0^+} \right\rangle_{19^-} \\ &= \langle ^{211}\text{Fr}, 33/2^+ \rangle + \left\langle \left(\pi h_{9/2}^4 i_{13/2} \right)_{33/2^+} \otimes \nu f_{5/2}^{-1} \right\rangle + \left\langle \nu f_{5/2}^{-1} \otimes j_{0^+}^{-2} \right\rangle. \end{aligned} \quad (\text{D.6})$$

To find the experimental values for the two last terms of Eq. D.6, the nuclei ^{212}Fr and ^{206}Pb can be used. The first term gives the proton-neutron hole coupling and an extra five proton interaction energy:

$$\begin{aligned} \langle ^{212}\text{Fr}, 19^- \rangle &= \left\langle \left(\pi h_{9/2}^4 i_{13/2} \right)_{33/2^+} \otimes \nu \left(f_{5/2}^{-1} \right)_{5/2^-} \right\rangle_{33/2^+} \\ &= \left\langle \left(\pi h_{9/2}^4 i_{13/2} \right)_{33/2^+} \otimes \nu \left(f_{5/2}^{-1} \right)_{5/2^-} \right\rangle + \langle \pi h_{9/2}^4 i_{13/2} \rangle_{33/2^+}, \end{aligned} \quad (\text{D.7})$$

while the second gives the three neutron excitation. The extra five valence proton interaction energy can be subtracted using the appropriate structure from ^{213}Fr . Finally, the j_{0^+} coupling can be taken from ^{206}Pb . As a result the residual interaction energy of the 19^- state is:

$$\begin{aligned} \langle ^{210}\text{Fr}, 19^- \rangle &= \left\langle \left(\pi h_{9/2}^4 i_{13/2} \right)_{33/2^+} \otimes \nu f_{5/2}^{-1} \otimes \left(j^{-2} \right)_{0^+} \right\rangle_{19^-} \\ &= \langle ^{212}\text{Fr}, 19^- \rangle + \langle ^{211}\text{Fr}, 33/2^+ \rangle - \langle ^{213}\text{Fr}, 33/2^+ \rangle + \langle ^{205}\text{Pb}, 5/2^- \rangle \\ &\quad + \langle ^{206}\text{Pb}, 0^+ \rangle. \end{aligned} \quad (\text{D.8})$$

The last two residual interactions equal zero as they represent the ground state of the respective nuclei. The excitation energy of a state is defined compared to the ground state mass of the nucleus [Laws 80].

For ^{210}Fr the ground state mass is defined as:

$$^{210}_{gs}\text{Fr} = 5\varepsilon_{h9/2} + 2\varepsilon_{p1/2-2} + \varepsilon_{f5/2-1}, \quad (\text{D.9})$$

where the ε 's are the single particle energies outside the closed shell, therefore relative to ^{208}Pb . The method to obtain single particle energies was shown in Figure 4.1. The energy of a state can now be defined as:

$${}_{\text{gs}}^{210}\text{Fr} + E_{19^-, {}_{\text{gs}}^{210}\text{Fr}} = \langle {}^{210}\text{Fr}, 19^- \rangle + \varepsilon_{i13/2} - \varepsilon_{h9/2}. \quad (\text{D.10})$$

Applying the same method for the nuclei involved in Eq. D.8, the energy of the 19^- can eventually be evaluated by the following equation:

$$\begin{aligned} E_{19^-, {}_{\text{gs}}^{210}\text{Fr}} &= E_{33/2^+, {}^{211}\text{Fr}} + E_{19^-, {}^{212}\text{Fr}} - E_{33/2^+, {}^{213}\text{Fr}} + \text{RM} \\ &= 3244 + 3583 - 3427 + \text{RM} \\ &= 3400 \text{ keV} + \text{RM}, \end{aligned} \quad (\text{D.11})$$

where RM designates the residual mass that arises when using the ground state mass as defined in Eq. D.9. Explicitly:

$$\begin{aligned} \text{RM} &= \left({}_{\text{gs}}^{212}\text{Fr} + {}_{\text{gs}}^{211}\text{Fr} + {}_{\text{gs}}^{205}\text{Pb} \right) - \left({}_{\text{gs}}^{213}\text{Fr} + {}_{\text{gs}}^{210}\text{Fr} \right) + {}_{\text{gs}}^{206}\text{Pb} + {}_{\text{gs}}^{207}\text{Pb} \\ &= -5 \text{ keV}. \end{aligned} \quad (\text{D.12})$$

This method proves its reliability when the calculated value 3395 keV¹ is compared to the observed energy of 3358 keV. Heavier Fr isotopes, however, lack the $35/2^+$ states (in ^{211}Fr and ^{213}Fr) and the 18^- state (^{212}Fr) that would allow for this method to be used for the determination of the 18^- and 20^- state energies in ^{210}Fr . The previous calculation would give a very similar result for either $\langle \nu p_{1/2}^{-2} f_{5/2}^{-1} \rangle$ or $\langle \nu p_{1/2}^{-1} f_{5/2}^{-2} \rangle$. That is because the $1/2^-$ state in ^{205}Pb is assumed to lie at 2 keV [Pole 85] therefore the two-body residual interaction that would appear in Eq. D.8 (the $\langle {}^{206}\text{Pb}, 2^+ \rangle$) would be 2 keV.

¹The ground state mass ^{207}Pb arises in Eq. D.12 because of the $f_{5/2}^{-1}$ neutron hole. While only two-body interactions are considered in the expansion, the ground state masses for the nuclei have to be taken into account.

APPENDIX D. CALCULATION OF THE 19^- STATE ENERGY IN ^{210}Fr
USING PARTIAL DECOMPOSITION

Appendix E

List of two-body residual interactions used in this work

The following tables present a list of two-body residual interaction that have been used or are relevant in this work. Nothing is added to the extensive table of Bayer *et al.* [Baye 99], but for completeness and ease the values are reproduced in this work.

APPENDIX E. LIST OF TWO-BODY RESIDUAL INTERACTIONS USED
IN THIS WORK

Table E.1: $\pi - \nu^{-1}$ -Two-body residual interactions for members of multiplets used in the calculation performed as part of this work (from Ref. [Baye 99] and references therein).

Configuration	J^π	E_{exp} (keV)	$\langle j_1, j_2 \rangle$ (keV)	Kuo & Herling (keV)
$\pi h_{9/2}\nu p_{1/2}^{-1}$	5^+	0	92	110
$\varepsilon_0 = -92$ keV	4^+	63	155	149
$\pi f_{7/2}\nu p_{1/2}^{-1}$	4^+	1034	229	252
$\varepsilon_0 = 805$ keV	3^+	937	132	230
$\pi i_{13/2}\nu p_{1/2}^{-1}$	7^-	1626	109	106
$\varepsilon_0 = 1517$ keV	6^-	1678	161	136
$\pi h_{9/2}\nu p_{3/2}^{-1}$	6^+	1095	289	288
$\varepsilon_0 = 806$ keV	5^+	887	81	21
	4^+	959	153	148
	3^+	1070	264	286
$\pi f_{7/2}\nu p_{3/2}^{-1}$	5^+	1837	134	303
$\varepsilon_0 = 1703$ keV	4^+	1564	-139	123
	3^+	1871	168	210
	2^+	2127	424	447
$\pi i_{13/2}\nu p_{3/2}^{-1}$	8^-			216
$\varepsilon_0 = 2415$ keV	7^-			113
	6^-			45
	5^-			407

Table E.1: (*Continued.*)

Configuration	J^π	E_{exp} (keV)	$\langle j_1, j_2 \rangle$ (keV)	Kuo & Herling (keV)
$\pi h_{9/2} \nu f_{5/2}^{-1}$ $\varepsilon_0 = 478$ keV	7 ⁺	651	173	278
	6 ⁺	511	33	-37
	5 ⁺	629	151	138
	4 ⁺	602	124	73
	3 ⁺	634	156	226
	2 ⁺	925	447	604
$\pi f_{7/2} \nu f_{5/2}^{-1}$ $\varepsilon_0 = 1375$ keV	6 ⁺	1738	363	257
	5 ⁺	1470	95	357
	4 ⁺	1605	230	75
	3 ⁺	1530	155	369
	2 ⁺	1540	165	200
	1 ⁺	1803	428	733
$\pi i_{13/2} \nu f_{5/2}^{-1}$ $\varepsilon_0 = 1375$ keV	9 ⁻			413
	8 ⁻			32
	7 ⁻			97
	6 ⁻			131
	5 ⁻			54
	4 ⁻			468
$\pi h_{9/2} \nu i_{13/2}^{-1}$ $\varepsilon_0 = 1541$ keV	11 ⁻	2427	886	754
	10 ⁻	1571	30	103
	9 ⁻	1787	246	271
	8 ⁻	1660	119	170
	7 ⁻	1716	175	226
	6 ⁻	1716	175	260
	5 ⁻	1704	163	252
	4 ⁻	1844	303	449
	3 ⁻	1921	380	390
	2 ⁻	2894	1353	1653

APPENDIX E. LIST OF TWO-BODY RESIDUAL INTERACTIONS USED
IN THIS WORK

Table E.1: (*Continued.*)

Configuration	J^π	E_{exp} (keV)	$\langle j_1, j_2 \rangle$ (keV)	Kuo & Herling (keV)
$\pi f_{7/2} \nu i_{13/2}^{-1}$	10 ⁻			321
$\varepsilon_0 = 2438$ keV	9 ⁻			-71
	8 ⁻			60
	7 ⁻			2
	6 ⁻			142
	5 ⁻			155
	4 ⁻			303
	3 ⁻			
$\pi i_{13/2} \nu i_{13/2}^{-1}$	13 ⁺			450
$\varepsilon_0 = 3150$ keV	12 ⁺			30
	11 ⁺			
	10 ⁺			
	9 ⁺			
	8 ⁺			-27
	7 ⁺			154
	6 ⁺			-43
	5 ⁺			
	4 ⁺			-35

Table E.2: $\pi - \pi$ - Two-body residual interactions for members of multiplets used in the calculation performed as part of this work (from Ref. [Baye 99] and references therein).

Configuration	J^π	E_{exp} (keV)	$\langle j_1, j_2 \rangle$ (keV)	Kuo & Herling (keV)
$\pi h_{9/2}^2$	8 ⁺	1557	373	390
$\varepsilon_0 = 1184$ keV	6 ⁺	1473	289	340
	4 ⁺	1427	243	320
	2 ⁺	1181	-3	40
	0 ⁺	1184	0	-1240
$\pi h_{9/2} f_{7/2}$	8 ⁺	2188	106	60
$\varepsilon_0 = 2082$ keV	7 ⁺	2438	356	300
	6 ⁺	2326	244	260
	5 ⁺	2403	321	340
	4 ⁺	2383	301	370
	3 ⁺	2414	332	340
	2 ⁺	2290	208	290
	1 ⁺	2394	312	250

Table E.2: (*Continued.*)

Configuration	J^π	E_{exp} (keV)	$\langle j_1, j_2 \rangle$ (keV)	Kuo & Herling (keV)
$\pi h_{9/2} i_{13/2}$ $\varepsilon_0 = 2794$ keV	11 ⁻	2849	55	80
	10 ⁻	3183	389	280
	9 ⁻	3000	206	200
	8 ⁻	3138	344	260
	7 ⁻	3017	223	260
	6 ⁻	3125	331	310
	5 ⁻	3026	232	330
	4 ⁻	3075	281	330
	3 ⁻	2846	52	220
	2 ⁻	3024	230	150
$\pi i_{13/2} f_{7/2}$ $\varepsilon_0 = 3691$ keV	10 ⁻		777	420
	9 ⁻		110	240
	8 ⁻			380
	7 ⁻			210
	6 ⁻			370
	5 ⁻			170
	4 ⁻			290
	3 ⁻			-130
	6 ⁺			280
	4 ⁺			210
$\pi f_{7/2}^2$ $\varepsilon_0 = 2979$ keV	2 ⁺			-60
	0 ⁺	2609	-370	-350
	12 ⁺			330
	10 ⁺			290
	8 ⁺		243	280
	6 ⁺			290
	4 ⁺			320
	2 ⁺			170
	9 ⁺			120

APPENDIX E. LIST OF TWO-BODY RESIDUAL INTERACTIONS USED
IN THIS WORK

Table E.3: $\nu^{-1} - \nu^{-1}$ - Two-body residual interactions for members of multiplets used in the calculation performed as part of this work (from Ref. [Baye 99] and references therein).

Configuration	J^π	E_{exp} (keV)	$\langle j_1, j_2 \rangle$ (keV)	Kuo & Herling (keV)
$\nu p_{1/2}^{-2}$	0^+	0	-630	-940
$\varepsilon_0 = 630$ keV				
$\nu p_{3/2}^{-2}$	2^+	2423	-3	-130
$\varepsilon_0 = 2426$ keV	0^+	2315	-111	-240
$\nu f_{5/2}^{-2}$	4^+	1684	-86	-90
$\varepsilon_0 = 1770$ keV	2^+	1784	14	-70
	0^+	1166	-604	-810
$\nu i_{13/2}^{-2}$	12^+	4027	131	140
$\varepsilon_0 = 3896$ keV	10^+	3958	62	80
	8^+			20
	6^+			-20
	4^+			-210
	2^+			-740
	0^+			-1040
$\nu p_{1/2}^{-1} p_{3/2}^{-1}$	2^+	1467	-61	-240
$\varepsilon_0 = 1528$ keV	1^+	1703	175	50
$\nu p_{1/2}^{-1} f_{5/2}^{-1}$	3^+	1341	141	140
$\varepsilon_0 = 1200$ keV	2^+	803	-397	-420
$\nu p_{3/2}^{-1} f_{5/2}^{-1}$	4^+	1998	-100	-130
$\varepsilon_0 = 2098$ keV	3^+	2214	116	60
	2^+	2148	50	40
	1^+	2250	152	10
$\nu p_{1/2}^{-1} i_{13/2}^{-1}$	7^-	2200	-63	-90
$\varepsilon_0 = 2263$ keV	6^-	2384	121	10
$\nu p_{3/2}^{-1} i_{13/2}^{-1}$	8^-			-10
$\varepsilon_0 = 3161$ keV	7^-	3225	64	-30
	6^-	3238	77	-20
	5^-	3016	-145	-150
$\nu i_{13/2}^{-1} f_{5/2}^{-1}$	9^-	2658	-175	-210
$\varepsilon_0 = 2833$ keV	8^-			150
	7^-	2865	32	90
	6^-	2940	107	130
	5^-	2782	-51	-90
	4^-	2826	-7	-100

Appendix F

Calculation of energy matrix elements using the shell model

In Section 4.1.4, it was shown how the energy matrix elements could be determined by using the relevant Hamiltonians for the interaction between the nucleon and for the *de facto* ground state energy (see Eq. 4.8). The interaction Hamiltonian (H_3 in Eq. 4.8) can be expressed using the two body matrix elements if the wave function is decomposed using the cfp's and the Racah W-coefficients (giving the probability for each decomposition). This is given by Lawson (see Eq. 1.96 in Ref. [Laws 80]):

$$\begin{aligned}
& \langle [(j_1)_{J'_1\beta'_1}^{n'_1} \otimes (j_2)_{J'_2\beta'_2}^{n'_2}]_{I,M} | H_3 | [(j_1)_{J_1\beta_1}^{n_1} \otimes (j_2)_{J_2\beta_2}^{n_2}]_{I,M} \rangle = \\
& (-1)^{J'_2 - J_2} n_1 n_2 \hat{J}_1 \hat{J}_2 \hat{J}'_1 \hat{J}'_2 \\
& \times \sum_{J=3\beta_3 J_4 \beta_4 L K} (2L+1)(2K+1) \langle j_1^{n_1-1} J_3 \beta_3, j_1 | \} j_1^{n_1} J_1 \beta_1 \rangle \times \langle j_1^{n_1-1} J_3 \beta_3, j_1 | \} j_1^{n_1} J'_1 \beta'_1 \rangle \\
& \times \langle j_2^{n_2-1} J_4 \beta_4, j_2 | \} j_2^{n_2} J_2 \beta_2 \rangle \times \langle j_2^{n_2-1} J_4 \beta_4, j_2 | \} j_2^{n_2} J'_2 \beta'_2 \rangle \\
& \times W(J_1 j_2 I J_4; L J_2) \times W(J'_1 j_2 I J_4; L J'_2) \times W(J_3 j_1 L j_2; J_1 K) \times W(J_3 j_1 L j_2; J'_1 K) \\
& \times E_K(j_1 j_2; j_1 j_2),
\end{aligned} \tag{F.1}$$

where the E_K are the two body matrix elements, and $\hat{J} = \sqrt{2J+1}$.

Using the previous equation, one can consequently calculate the energy matrix elements for a configuration. Since this becomes of tremendous size with the addition of more than a few particles outside the core, such a calculation can only be made (by hand) by constraining the space to only several nucleons. A calculation for the $29/2^+$ state in ^{213}Fr that arises from the $\pi(h_{9/2}^4 i_{13/2})$ configuration is presented here.

F.1 The $29/2^+$ state in ^{213}Fr

The 350 ns $29/2^+$ isomer in ^{213}Fr lies at an excitation energy of 2538 keV [Byrn 86b]. The structure of the state is known to be $\pi(h_{9/2}^4 i_{13/2})$. In order to calculate the energy of the state using Eq. F.1, one must know the two-body residual interaction that appear in both Eqs. F.1) and F.2. These come from ^{210}Po and are listed in Appendix E (specifically $\pi h_{9/2} i_{13/2}$ values). Due to angular momentum recoupling not all of the couplings (from 2^- to 11^-) in ^{210}Po will take part in the $29/2^+$ state energy. The expansion of each ($\beta\alpha$) element of Eq. F.2 is extremely long, for example the $V_{(82)\times(82)}$ (where $J = 8$ and the seniority is $\beta = 2$) element has 69 non zero components (each of them being the product of one cfp and one W-coefficient).

$$\begin{aligned}
 & \langle \overset{4}{\underset{\beta\alpha}{\text{h}_{9/2}}} \underset{\text{J}\nu}{\text{i}_{13/2}} | H | \overset{4}{\underset{\beta\alpha}{\text{h}_{9/2}}} \underset{\text{J}\nu}{\text{i}_{13/2}} \rangle \\
 &= 4 \times \sum_{\beta\alpha\kappa} \left\langle \frac{9}{2} \beta' \left[\frac{9}{2} \alpha' \right] \right\rangle \frac{9}{2} \beta \alpha \rangle^2 W\left(\beta' \frac{9}{2} \text{J} \frac{13}{2}; \beta \kappa\right)^2 \\
 & \times \underbrace{\left\langle \frac{9}{2} \kappa \left[\frac{13}{2} \right] | H | \frac{9}{2} \kappa \left[\frac{13}{2} \right] \right\rangle}_{E_K\left(\frac{9}{2} \frac{13}{2}; \frac{9}{2} \frac{13}{2}\right)} \quad (F.2)
 \end{aligned}$$

where the W -functions are the Racah coefficients (tabulated in Ref. [Appe 68], a simple program to calculate them is alternatively given below) that represent the probability of each diagram, so that $\sum W^2 = 1$.

The energy matrix obtained is¹:

$$\begin{pmatrix} 1668.9 & -3.0 & -14.8 & 6.3 & 22.9 \\ -3.0 & 2668.9 & -130.0 & 30.0 & 15.8 \\ -14.8 & -130.0 & 2719.2 & 103.6 & -92.2 \\ 6.3 & 30.0 & 103.6 & 2770.7 & -130.7 \\ 22.9 & 15.8 & -92.2 & -130.7 & 3165.1 \end{pmatrix}. \quad (F.3)$$

¹Note that there are only five ways to create a $29/2^+$ state in the $[h_{9/2}, i_{13/2}]^5$ space.

F.2. THE W-COEFFICIENTS

Upon diagonalisation the eigenvalues are:

$$\begin{pmatrix} 1668.3 & & & \\ & 2527.5 & & \\ & & 2744.5 & \\ & & & 2817.7 \\ & & & \\ & & & 3234.8 \end{pmatrix}, \quad (\text{F.4})$$

which compares well to the (unpublished) values obtained by Byrne *et al.* [Byrn 11] in the intermediate calculation of the energy of the state.

For completeness the energy matrix elements, determined using H_1 , H_2 and H_3 , as calculated by Sesame [Davi 05] for the $29/2^+$ states, are $\lambda_1 = 2591.3$, $\lambda_2 = 3480.1$, $\lambda_3 = 3514.3$, $\lambda_4 = 3669.9$, $\lambda_5 = 4132.4$.

F.2 The W-coefficients

Since the cfp's are relatively complex to compute, it is usual to use the table of Bayman and Lande [Baym 66]. However, to perform the previous calculation, the W-functions are derived from the Wigner 6-j symbols [Appe 68]:

$$\begin{Bmatrix} j_1 & j_2 & j_3 \\ \ell_1 & \ell_2 & \ell_3 \end{Bmatrix} = (-1)^{j_1+j_2+\ell_1+\ell_2} \Delta(j_1 j_2 j_3) \Delta(\ell_1 \ell_2 \ell_3) \Delta(\ell_1 j_2 \ell_3) \Delta(j_1 \ell_2 \ell_3) \\ \sum_k \frac{(-1)^k (j_1 + j_2 + \ell_1 + \ell_2 + 1 - k)!}{k! (j_1 + j_2 - j_3 - k)! (\ell_1 + \ell_2 - j_3 - k)! (j_1 + \ell_2 - \ell_3 - k)!} \\ \times \frac{}{(\ell_1 + j_2 - \ell_3 - k)! (-j_1 - \ell_1 + j_3 + \ell_3 + k)! (-j_2 - \ell_2 + j_3 + \ell_3 + k)!}, \quad (\text{F.5})$$

where the Δ functions are defined by:

$$\Delta(abc) = \sqrt{\left(\frac{(a+b-c)!(a-b+c)!(-a+b+c)!}{(a+b+c+1)!} \right)}. \quad (\text{F.6})$$

The W function are then obtained by:

$$\begin{Bmatrix} j_1 & j_2 & j_3 \\ \ell_1 & \ell_2 & \ell_3 \end{Bmatrix} = (-1)^{j_1+j_2+\ell_1+\ell_2} W(j_1 j_2 \ell_2 \ell_1; j_3 \ell_3). \quad (\text{F.7})$$

The first step for the computation of Eq. F.1 is then to code the W-functions. The following gives a code that calculates the value for the Racah W-coefficients. It is written in R and can be readily copied.

APPENDIX F. CALCULATION OF ENERGY MATRIX ELEMENTS USING THE SHELL MODEL

```
### Calculation of Wigner-6j Coefficients ###
### Formulas are taken from Numerical Data and Functional
Relationships in Science and Technology / Volume 3 ###

Delta <- function(a,b,c){
  y <- ((factorial(a+b-c)*factorial(a-b+c)*factorial(-a+b+c))
  /factorial(a+b+c+1))^(1/2) }

S <- rep(0, 15)

Expansion <- function(j1, j2, j3, l1, l2, l3)
{ Quad <- min(-j1-l1+j3+l3, -j2-l2+j3+l3);
  Trian <- min(j1+j2-j3, l1+l2-j3, j1+l2-l3, l1+j2-l3);
  if ( abs(Quad) == Trian ) {
    i <- Trian;
    y <- ((-1)^i*factorial(j1+j2+l1+l2+1-i))/(
      factorial(i)*factorial(j1+j2-j3-i)
      *factorial(l1+l2-j3-i)*factorial(j1+l2-l3-i)
      *factorial(l1+j2-l3-i)*factorial(-j1-l1+j3+l3+i)
      *factorial(-j2-l2+j3+l3+i) )

    if ( abs(Quad) < Trian ) {
      for ( i in abs(Quad) : Trian )
      { S[i+1] <- ((-1)^i*factorial(j1+j2+l1+l2+1-i))/(
        factorial(i)*factorial(j1+j2-j3-i)
        *factorial(l1+l2-j3-i)*factorial(j1+l2-l3-i)
        *factorial(l1+j2-l3-i)*factorial(-j1-l1+j3+l3+i)
        *factorial(-j2-l2+j3+l3+i) )

      y <- sum(S);
    }

    if ( Trian < abs(Quad) ) {
      for ( i in ( 0 : Trian ) )
      { S[i+1] <- ((-1)^i*factorial(j1+j2+l1+l2+1-i))/(
        factorial(i)*factorial(j1+j2-j3-i)
        *factorial(l1+l2-j3-i)*factorial(j1+l2-l3-i)
        *factorial(l1+j2-l3-i)*factorial(-j1-l1+j3+l3+i)
        *factorial(-j2-l2+j3+l3+i) )

      }
    y <- sum(S)    }
  return(y)    }
```

F.2. THE W-COEFFICIENTS

```
w6j <- function(j1,j2,j3,l1,l2,l3){
  if ((j1+j2-j3) < 0) {
    y <- 0
    return('is 0 because j1+j2-j3 < 0') }
  if ((j1-j2+j3) < 0) {
    y <- 0
    return('is 0 because j1-j2+j3 < 0') }
  if ((-j1+j2+j3) < 0) {
    y <- 0
    return('is 0 because -j1+j2+j3 < 0') }
  if ((j1+l2-l3) < 0) {
    y <- 0
    return('is 0 because j1+l2-l3 < 0') }
  if ((j1-l2+l3) < 0) {
    y <- 0
    return('is 0 because j1-l2+l3 < 0') }
  if ((-j1+l2+l3) < 0) {
    y <- 0
    return('is 0 because -j1+l2+l3 < 0') }
  if ((l1+l2-j3) < 0) {
    y <- 0
    return('is 0 because l1+l2-j3 < 0') }
  if ((l1-l2+j3) < 0) {
    y <- 0
    return('is 0 because l1-l2+j3 < 0') }
  if ((-l1+l2+j3) < 0) {
    y <- 0
    return('is 0 because -l1+j2+j3 < 0') }
  if ((l1+j2-l3) < 0) {
    y <- 0
    return('is 0 because l1+j2-l3 < 0') }
  if ((l1-j2+l3) < 0) {
    y <- 0
    return('is 0 because l1-j2+l3 < 0') }
  if ((-l1+j2+l3) < 0) {
    y <- 0
    return('is 0 because -l1+j2+l3 < 0') }
  if ((abs(j1-j2)-j3) > 0) {
    y <- 0
    return('is 0 because |j1-j2| > j3') }
  if ((abs(j1-l2)-l3) > 0) {
```

APPENDIX F. CALCULATION OF ENERGY MATRIX ELEMENTS USING THE SHELL MODEL

```
y <- 0
  return('is 0 because |j1-l2| > 13') }
if ((abs(j2-l1)-13) > 0) {
  y <- 0
  return('is 0 because |j2-l1| > 13') }
if ((abs(j3-l1)-12) > 0) {
  y <- 0
  return('is 0 because |j3-l1| > 12') }
else {
y <- (-1)^(j1+j2+l1+l2)*Delta(j1,j2,j3)*Delta(l1,l2,j3)
  *Delta(l1,j2,l3)*Delta(j1,l2,l3)
  *Expansion(j1,j2,j3,l1,l2,l3)
}
}

Racah <- function(j1, j2, j3, l1, l2, l3){
  y <- W6J(j1, j2, j3, l1, l2, l3)/(-1)^(j1+j2+l1+l2)
}

UFct <- function(j1, j2, j3, l1 ,l2, l3){
  y <- (2*j3+1)^(1/2)*(2*l3+1)^(1/2)*Racah(j1, j2, j3, l1, l2, l3)
}

print(' This program calculates the Wigner 6J Symbol and computes the
      linearly linked Racah Coefficient and U Function, the W6J function
      explains any 0 by highlighting the appropriate triangle rule,
      though note that the parameters for W6J is a vector (j1, j2, j3,
      l1, l2, l3) which corresponds in the habitual notation for W to
      (j1, j2, l2, l1, j3, l3), this might be source of confusion...')
```

Bibliography

- [Ande 55] G. Andersson, E. Arbman, I. Bergstrom, and A. H. Wapstra. “Neutron Deficient Isotopes of Pb and Tl - III - Mass Numbers Below 200”. *Phil.Mag.*, Vol. 46, p. 70, 1955.
- [Ande 57] G. Andersson, E. Arbman, and B. Jung. “Lead and Thallium Isotopes in the Mass Range 195-199”. *Arkiv Fysik*, Vol. 11, p. 297, 1957.
- [Appe 68] H. Appel. *Numerical Data and Functional Relationships in Science and Technology*. Vol. 3, Springer-Verlag, 1968.
- [Astr 57] B. Astrom. “Half-Lives of Isomeric States in ^{202}Pb , ^{203}Pb , ^{206}Pb , and ^{202}Tl ”. *Arkiv Fysik*, Vol. 12, p. 237, 1957.
- [Audi 03] G. Audi, A. H. Wapstra, and C. Thibault. “The AME2003 Atomic Mass Evaluation (II)”. *Nucl. Phys.*, Vol. A729, No. 1, pp. 337 – 676, 2003.
- [Bara 52] M. Baranger, F. J. Dyson, and E. E. Salpeter. “Fourth-Order Vacuum Polarization”. *Phys. Rev.*, Vol. 88, pp. 680–680, 1952.
- [Bass 80] R. Bass. *Nuclear Reactions with Heavy Ions*. Springer-Verlag, 1980.
- [Bay 50] Z. Bay. “Calculation of Decay Times from Coincidence Experiments”. *Phys. Rev.*, Vol. 77, pp. 419–419, 1950.
- [Baye 01] S. Bayer, A. P. Byrne, G. D. Dracoulis, A. M. Baxter, T. Kibédi, and F. G. Kondev. “Core-excited states and core-polarization effects in ^{210}At and ^{211}At ”. *Nuclear Physics A*, Vol. 694, No. 1-2, pp. 3 – 62, 2001.
- [Baye 99] S. Bayer, A. P. Byrne, G. D. Dracoulis, A. M. Baxter, T. Kibédi, F. G. Kondev, S. M. Mullins, and T. R. McGoram. “High-Spin States, Yrast Isomers and Residual Interactions in the Odd-Odd Nucleus ^{212}At ”. *Nuclear Physics A*, Vol. 650, No. 1, pp. 3 – 36, 1999.

BIBLIOGRAPHY

- [Baym 66] B. F. Bayman and A. Lande. “Tables of Identical-Particle Fractional Parentage Coefficients”. *Nuclear Physics*, Vol. 77, No. 1, pp. 1 – 80, 1966.
- [Beng 07] R. Bengtsson and P. Möller. “Nuclear Physics: a Non-Disappearing Magic Trick”. *Nature*, Vol. 449, pp. 411–413, September 2007.
- [Berg 85] I. Bergström and B. Fant. “Systematics of B(E3) Values in the Trans-Lead Region”. *Phys. Scr.*, Vol. 31, pp. 26–30, 1985.
- [Blom 83] J. Blomqvist, P. Kleinheinz, and P. J. Daly. “Atomic Masses Above ^{146}Gd Derived from a Shell Model Analysis of High Spin States”. *Zeitschrift für Physik A Hadrons and Nuclei*, Vol. 312, pp. 27–41, 1983.
- [Boda 62] D. Bodansky. “Compound Statistical Features in Nuclear Reactions”. *Annual Review of Nuclear Science*, Vol. 12, No. 1, pp. 79–122, 1962.
- [Bohr 69] A. Bohr and B. Mottelson. *Nuclear Structure*. W. A. Benjamin, 1969.
- [Boni 68] M. Bonitz, J. Kantele, and N. J. Sigurd Hansen. “Evidence for j -Forbidden Isomeric Transition in ^{208}Bi ”. *Nuclear Physics A*, Vol. 115, No. 1, pp. 219 – 224, 1968.
- [Byrn 11] A. P. Byrne. 2011. Private communication.
- [Byrn 86a] A. P. Byrne. *The Nuclear Structure of High Spin States in $^{211,212,213}\text{Fr}$* . PhD thesis, The Australian National University, Canberra, Australia, 1986.
- [Byrn 86b] A. P. Byrne, G. D. Dracoulis, C. Fahlander, H. Hubel, A. R. Poletti, A. E. Stuchbery, J. Gerl, R. F. Davie, and S. J. Poletti. “Spectroscopy of High-Spin States in $^{211,212,213}\text{Fr}$ ”. *Nuclear Physics A*, Vol. 448, No. 1, pp. 137 – 188, 1986.
- [Byrn 94] A. P. Byrne, G. J. Lane, G. D. Dracoulis, B. Fabricius, T. Kibédi, A. E. Stuchbery, A. M. Baxter, and S. K. J. “Octupole coupling and proton-neutron interactions in ^{214}Fr ”. *Nuclear Physics A*, Vol. 567, No. 2, pp. 445 – 476, 1994.
- [Davi 05] P. M. Davidson. “SESAME User Manual, Internal Report P1636 (unpublished)”. Tech. Rep., The Australian National University, Department of Nuclear Physics, Canberra, Australia, 2005.

BIBLIOGRAPHY

- [Debr 90] M. E. Debray, J. Davidson, M. Davidson, A. J. Kreiner, D. Hojman, D. Santos, K. Ahn, D. B. Fossan, Y. Liang, R. Ma, E. S. Paul, W. F. Piel, and N. Xu. “Evidence for the Onset of Reflection Asymmetry in ^{216}Fr ”. *Phys. Rev. C*, Vol. 41, pp. R1895–R1898, 1990.
- [DoE 12] DoE - US Department of Energy. “The National Nuclear Data Center”. www.nndc.bnl.gov. 2012.
- [Drac 09a] G. D. Dracoulis, P. M. Davidson, G. J. Lane, A. P. Byrne, T. Kibédi, P. Nieminen, H. Watanabe, and A. N. Wilson. “Spectroscopy and High-Spin Structure of ^{209}Fr ”. *Phys. Rev. C*, Vol. 79, p. 054313, 2009.
- [Drac 09b] G. D. Dracoulis, P. M. Davidson, G. J. Lane, A. P. Byrne, T. Kibédi, P. Nieminen, A. N. Wilson, and H. Watanabe. “Assignment of Levels in ^{208}Fr and 10^- Isomers in the Odd-Odd Isotones ^{206}At and ^{208}Fr ”. *The European Physical Journal A - Hadrons and Nuclei*, Vol. 40, pp. 127–130, 2009.
- [Drig 85] M. W. Drigert, J. A. Cizewski, and M. S. Rosenthal. “Level structure of ^{215}Fr ”. *Phys. Rev. C*, Vol. 32, pp. 136–144, 1985.
- [Ekst 78] C. Ekström, S. Ingelman, G. Wannberg, and M. Skarestad. “Nuclear Ground State Spins of the Francium Isotopes $^{208-213,220-222}\text{Fr}$ ”. *Physica Scripta*, Vol. 18, pp. 51–53, 1978.
- [Fant 84] B. Fant, T. Weckstræm, T. Lönnroth, C. J. Herrlander, K. Honkanen, and A. Kallberg. “Study of the Three-Proton Three-Neutron-Hole Nucleus ^{208}Fr ”. *Nuclear Physics A*, Vol. 429, No. 2, pp. 296 – 312, 1984.
- [Feng 99] X. C. Feng, Y. X. Guo, X. H. Zhou, X. F. Sun, X. G. Lei, W. X. Huang, J. J. He, Z. Liu, Y. H. Zhang, S. F. Zhu, Y. X. Luo, S. X. Wen, G. J. Yuan, and X. G. Wu. “Level Structure in ^{206}At ”. *The European Physical Journal A - Hadrons and Nuclei*, Vol. 6, pp. 235–237, 1999.
- [Fisc 55] V. K. Fischer. “Metastable States of ^{180}Re , ^{191}Ir , ^{193}Au , ^{201}Pb , and ^{203}Pb ”. *Phys. Rev.*, Vol. 99, pp. 764–770, 1955.
- [Frit 58] A. Fritsch and J. Hollander. “Radiations from Decay of Bismuth-203, Bismuth-204, Lead-204m, and Bismuth-205”. *Journal of Inorganic and Nuclear Chemistry*, Vol. 6, No. 3, pp. 165–180, 1958.

BIBLIOGRAPHY

- [Gipp 75] P. Gippner, K.-H. Kaun, W. Neubert, W. Schulze, and F. Stary. “A j -Forbidden Isomeric Transition in ^{204}At ”. *Nuclear Physics A*, Vol. 237, No. 1, pp. 142–148, 1975.
- [Hage 72] U. Hagemann, K.-H. Kaun, W. Neubert, W. Schulze, and F. Stary. “Two-Quasiparticle Isomeric States in Doubly Odd Bi nuclei”. *Nuclear Physics A*, Vol. 197, No. 1, pp. 111 – 120, 1972.
- [Hama 74] I. Hamamoto. “Particle Spectra and Particle-Vibration Coupling in the Pb Region”. *Physics Reports*, Vol. 10, No. 2, pp. 63–105, 1974.
- [Haus 72] O. Häusser, F. C. Khanna, and D. Ward. “Gamma Decay of Low-Lying States Near the ^{208}Pb Closed Shell”. *Nucl. Phys. A*, Vol. 194, No. 1, pp. 113–119, 1972.
- [Hick 80] K. Hicks and T. Ward. “The Half-Life of ^{197g}Pb ”. *Nuclear Physics A*, Vol. 349, No. 1-2, pp. 29 – 36, 1980.
- [Huys 92] M. Huyse, P. Decrock, P. Dendooven, G. Reusen, P. Van Duppen, and J. Wauters. “Isomers in Three Doubly Odd Fr-At-Bi α -Decay Chains”. *Phys. Rev. C*, Vol. 46, pp. 1209–1217, 1992.
- [Jons 71] B. Jonson, M. Alpsten, A. Appelqvist, and G. Astner. “Levels in ^{207}Po Populated in the Decay of ^{207}At ”. *Nuclear Physics A*, Vol. 177, No. 1, pp. 81 – 102, 1971.
- [Kanj 11] D. Kanjilal, S. Saha, S. Bhattacharya, A. Goswami, R. Kshetri, R. Raut, S. Muralithar, R. P. Singh, G. Mukherjee, and B. Mukherjee. “First Observation of High Spin States and Isomeric Decay in ^{210}Fr ”. *Phys. Rev. C*, Vol. 84, p. 064321, 2011.
- [Kibe 08] T. Kibédi, T. W. Burrows, Trzhaskovskaya, P. M. Davidson, and C. W. Nestor Jr. “Evaluation of Theoretical Conversion Coefficients Using BrIcc”. *Nuclear Instruments and Methods in Physics Research Section A: Accelerators, Spectrometers, Detectors and Associated Equipment*, Vol. 589, No. 2, pp. 202–229, 2008.
- [Kran 88] K. S. Krane. *Introductory Nuclear Physics*. John Wiley & Sons, 1988.
- [Kuo 71] T. T. S. Kuo and G. H. Herling. “NRL Report no. 2258”. Tech. Rep., Naval Research Laboratory, Washington, 1971.

BIBLIOGRAPHY

- [Kuus 04] P. Kuusiniemi, F. P. Heßberger, D. Ackermann, S. Hofmann, and I. Kojouharov. “Decay Studies of $^{214-216}\text{Ac}$ by α - γ - γ -Coincidences”. *The European Physical Journal A - Hadrons and Nuclei*, Vol. 22, pp. 429–442, 2004.
- [Lane 95] G. J. Lane. *Coexistence and Structure of Deformed Shapes Near the Z=82 Closed Shell*. PhD thesis, The Australian National University, 1995.
- [Lane 98] G. J. Lane, D. B. Fossan, J. M. Sears, J. F. Smith, J. A. Cameron, R. M. Clark, I. M. Hibbert, V. P. Janzen, R. Krücken, I.-Y. Lee, A. O. Macchiavelli, C. M. Parry, and R. Wadsworth. “Octupole Correlations at Low Spin in $^{108}_{52}\text{Te}_{56}$ ”. *Phys. Rev. C*, Vol. 57, pp. R1022–R1026, 1998.
- [Laws 80] R. D. Lawson. *Theory of the Nuclear Shell Model. Oxford studies in nuclear physics*, Clarendon Press, Oxford, 1980.
- [Lind 76] C. G. Lindén, I. M. Bergström, J. Blomqvist, K. G. Rensfelt, H. Ser-golle, and K. Westerberg. “High Spin States ^{205}Pb and a Precision Test of the Nuclear Shell Model for Three Nucleons”. *Zeitschrift für Physik A Hadrons and Nuclei*, Vol. 277, pp. 273–290, 1976.
- [Lind 77] C. G. Lindén. “A 480 ms Isomeric $29/2^-$ State of the $(p_{1/2}^0)_{0+} f_{5/2}^{-1}(i_{13/2}^{-2})_{12+}$ Configuration in ^{203}Pb ”. *Z.Phys.*, Vol. A280, p. 51, 1977.
- [Ling 77] E. W. A. Lingeman. “Levels in ^{206}Po Populated in the EC- β^+ Decay of ^{206}At ”. *Phys.Scr.*, Vol. 15, p. 205, 1977.
- [LNHB 12] LNHB - Laboratoire National Henri Becquerel. “Table des Nucléides”. www.nucleide.org. 2012.
- [Lobn 75] K. E. G. Löbner. “Gamma-Ray Transition Probabilities in Deformed Nuclei”. In: W. D. Hamilton, Ed., *The Electromagnetic Interaction in Nuclear Spectroscopy*, Chap. 6, pp. 141–171, North-Holland, 1975.
- [Lonn 81] T. Lönnroth, B. Fant, K. Fransson, A. Kallberg, K.-O. Pettersson, and L. Vogh. “High-Spin States in ^{204}Bi and the Question of Many-Nucleon Configuration Mixing and the Question of Many-Nucleon Configuration Mixing”. *Physica Scripta*, Vol. 23, No. 5A, p. 774, 1981.

BIBLIOGRAPHY

- [Lonn 88] T. Lönnroth. “Evidence for Three Microscopically Different Kinds of $E1$ Transition in Lead-Region Nuclei”. *Zeitschrift für Physik A Hadrons and Nuclei*, Vol. 331, pp. 11–19, 1988.
- [Macf 60] M. H. Macfarlane and J. B. French. “Stripping Reactions and the Structure of Light and Intermediate Nuclei”. *Rev. Mod. Phys.*, Vol. 32, pp. 567–691, 1960.
- [Maie 71] K. Maier, J. Leigh, and R. Diamond. “Measurement of the Magnetic Moment and Lifetime of the $13/2^+$ Level in ^{205}Pb ”. *Nuclear Physics A*, Vol. 176, No. 3, pp. 497–504, 1971.
- [Marg 12] V. Margerin, G. J. Lane, G. D. Dracoulis, N. Palalani, and M. L. Smith. “Levels in ^{210}Fr and the decay of a high-spin, multi-particle isomer”. *EPJ Web of Conferences*, Vol. 35, p. 06003, 2012.
- [Mate 74] E. D. Mateosian and A. Sunyar. “Tables of Attenuation Coefficients for Angular Distribution of Gamma Rays from Partially Aligned Nuclei”. *Atomic Data and Nuclear Data Tables*, Vol. 13, No. 4, pp. 391 – 406, 1974.
- [Meye 06] D. A. Meyer, C. W. Beausang, J. J. Ressler, H. Ai, H. Amro, M. Babillon, R. F. Casten, C. R. Fitzpatrick, G. Gürdal, A. Heinz, E. A. McCutchan, C. Plettner, J. Qian, N. J. Thomas, V. Werner, E. Williams, N. V. Zamfir, and J.-y. Zhang. “First Investigation of Excited States in the Odd-Proton Nucleus ^{209}Fr ”. *Phys. Rev. C*, Vol. 73, p. 024307, 2006.
- [More 69] T. Morek, W. Neubert, S. Chojnacki, K. Alexander, and Z. Wilhelm. “A Short-Lived Isomer in ^{203}At ”. Tech. Rep. JINR-P6-4494, 1969.
- [Newt 74] J. O. Newton. *Nuclear Spectroscopy and Reactions*, Chap. VII.E, pp. 185–225. Vol. C, Academic Press, 1974.
- [Nybe 12] J. Nyberg. “AGATA - Advanced Gamma Tracking Array”. *pre-print*, No. arXiv:1111.5731v1, 2012.
- [Paul 75] H. C. Pauli, K. Alder, and R. M. Steffen. “The Theory of Internal Conversion”. In: W. D. Hamilton, Ed., *The Electromagnetic Interaction in Nuclear Spectroscopy*, Chap. 10, pp. 341–440, North-Holland, 1975.

BIBLIOGRAPHY

- [Pelt 82] D. Pelte and D. Schwalm. *Heavy Ion Collisions*, Chap. 1. North Holland, Amsterdam, 1982.
- [Pole 82] A. R. Poletti, G. D. Dracoulis, C. Fahlander, and I. Morrison. “Yrast Traps and High-Spin States in ^{210}Rn ”. *Nuclear Physics A*, Vol. 380, No. 2, pp. 335–364, 1982.
- [Pole 85] A. R. Poletti, G. D. Dracoulis, C. Fahlander, and A. P. Byrne. “The Yrast Spectroscopy of ^{209}Rn ”. *Nuclear Physics A*, Vol. 440, No. 1, pp. 118–142, 1985.
- [Pole 86] S. J. Poletti, G. D. Dracoulis, A. R. Poletti, A. P. Byrne, A. E. Stuchbery, and J. Gerl. “g-Factors in ^{210}Rn and octupole coupling of core-excited states in ^{210}Rn , ^{211}Rn and ^{212}Rn ”. *Nuclear Physics A*, Vol. 448, No. 1, pp. 189–204, 1986.
- [Pole 94] A. Poletti, G. Dracoulis, A. Byrne, A. Stuchbery, B. Fabricius, T. KibÅdi, and P. Davidson. “Structure of low-lying high-spin states in ^{204}Hg and ^{205}Hg ”. *Nuclear Physics A*, Vol. 580, No. 1, pp. 64–80, 1994.
- [Raca 43] G. Racah. “Theory of Complex Spectra. III”. *Phys. Rev.*, Vol. 63, pp. 367–382, 1943.
- [Radf 95] D. Radford. “ESCL8R and LEVIT8R: Software for interactive graphical analysis of HPGe coincidence data sets”. *Nuclear Instruments and Methods in Physics Research Section A: Accelerators, Spectrometers, Detectors and Associated Equipment*, Vol. 361, pp. 297–305, 1995.
- [Raki 74] Y. N. Rakivnenko, A. P. Klyucharev, V. A. Lutsik, I. A. Romanii, E. A. Skakun, and G. I. Yatsenko. “Decay of the Millisecond Isomers ^{204m}Bi and ^{206m}Bi ”. *Yad.Fiz.*, Vol. 20, p. 617, 1974.
- [Rao 81] B. Rao, R. Broda, C. Günther, A. Kleinrahm, and M. Ogawa. “The 10^- Isomer and Other High-Spin States in ^{202}Bi ”. *Nuclear Physics A*, Vol. 362, No. 1, pp. 71–85, 1981.
- [Rapa 79] M. Rapaport, R. Fink, L. Riedinger, L. Collins, and G. O’Kelley. “Half-Lives and Decay of ^{197}Pb Isomers”. *Nuclear Physics A*, Vol. 315, No. 1-2, pp. 163–168, 1979.

BIBLIOGRAPHY

- [Redm 54] P. J. Redmond. “An Explicit Formula for the Calculation of Fractional Parentage Coefficients”. *Proceedings of the Royal Society of London. Series A. Mathematical and Physical Sciences*, Vol. 222, No. 1148, pp. 84–93, 1954.
- [Ritc 81] B. G. Ritchie, K. S. Toth, H. K. Carter, R. L. Mlekodaj, and E. H. Spejewski. “Alpha-Decay Properties of $^{205,206,207,208}\text{Fr}$: Identification of ^{206m}Fr ”. *Phys. Rev. C*, Vol. 23, pp. 2342–2344, 1981.
- [Stef 75] R. M. Steffen and K. Alder. “Angular Distribution and Correlation of Gamma-Rays”. In: W. D. Hamilton, Ed., *The Electromagnetic Interaction in Nuclear Spectroscopy*, Chap. 12, pp. 505–582, North-Holland, 1975.
- [Stoc 56] R. Stockendal, J. A. McDonnell, M. Schmorak, and I. Bergstrom. “Nuclear Isomerism in Odd Lead Isotopes”. *Arkiv Fysik*, Vol. 11, p. 165, 1956.
- [Stod 91] H. Stodart. *The Measurement of Lifetimes in $^{216,217}\text{Rn}$ Using the $\gamma\text{-}\gamma$ -Time Technique*. Honour’s thesis, The Australian National University, Canberra, Australia, 1991.
- [Thom 68] T. D. Thomas. “Compound Nuclear Reactions Induced by Heavy Ions”. *Annual Review of Nuclear Science*, Vol. 18, No. 1, pp. 343–406, 1968.
- [Usui 05] J. Uusitalo, M. Leino, T. Enqvist, K. Eskola, T. Grahn, P. T. Greenlees, P. Jones, R. Julin, S. Juutinen, A. Keenan, H. Kettunen, H. Koivisto, P. Kuusiniemi, A.-P. Leppänen, P. Nieminen, J. Pakarinen, P. Rahkila, and C. Scholey. “ α Decay Studies of Very Neutron-Deficient Francium and Radium Isotopes”. *Phys. Rev. C*, Vol. 71, p. 024306, 2005.